# Process Design and Optimization for Recovery of Biohydrogen

Prozessentwicklung und -optimierung der Biowasserstoffaufbereitung

Von der Fakultät für Maschinenwesen
der Rheinisch-Westfälischen Technischen Hochschule Aachen
zur Erlangung des akademischen Grades
eines Doktors der Ingenieurwissenschaften genehmigte Dissertation

vorgelegt von

Burkhard Eike Ludger Ohs

Berichter:
Univ.-Prof. Dr.-Ing. Matthias Wessling
Univ.-Prof. Dr.-Ing. Dieter Bathen

Tag der mündlichen Prüfung: 09.09.2020

Diese Dissertation ist auf den Internetseiten der Universitätsbibliothek online verfügbar.

# Danksagung

Die Dissertation ist nie das Ergebnis eines Einzelnen. Vielmehr entsteht eine solche Arbeit in enger Zusammenarbeit vieler Personen. Allen, die zum Gelingen der vorliegenden Arbeit beigetragen haben, möchte ich hiermit herzlich danken.

Mein besonderer Dank gilt Professor Matthias Wessling für die Möglichkeit diese Arbeit an seinem Lehrstuhl verfassen zu können und seine zahlreichen Ideen, die in diese Arbeit eingeflossen sind. Ebenso möchte ich mich bei Professor Dieter Bathen für die Übernahme des Koreferates und die Begutachtung der vorliegenden Arbeit bedanken.

Mein Dank gilt insbesondere auch meinen Kollegen für die vielfältigen Diskussionen und Anregungen, die diese Arbeit sehr bereichert haben. Vor allem möchte ich hier meinen Bürokollegen und den SusPro-Mitgliedern danken. Die enge Zusammenarbeit mit den Kollegen hat mir besonders viel Spaß gemacht und war stehts eine große Motivation diese Arbeit fertigzustellen. Besonders möchte ich mich bei Laura Keller und Benedikt Aumeier für die zahlreichen Diskussionen über Adsorptionsmaterialien und -prozesse bedanken.

Einen großen Beitrag zu dieser Arbeit und zu weiteren Projekten haben meine studentischen Hilfskräfte sowie Bachelor- und Masterarbeiter geleistet. Ich möchte mich nochmal ganz herzlich für die vielen Ideen, die tiefgehenden Diskussionen, die hohe Motivation und den unermütlichen Einsatz bedanken. Namentlich möchte ich hier folgende Studenten hervorheben, die ich für einen längeren Zeitraum begleiten durfte: Johannes Lohaus, Thomas Waltermann, Philipp Thenee, Martin Falkenberg, Lorenz Abduly und Maximilian Krödel.

Meiner Familie und meinen Freunden danke ich dafür, dass sie mir stets zur Seite gestanden und zur richtigen Zeit für einen ausreichenden Ausgleich gesorgt haben. Hier gilt mein besonderer Dank meinem Bruder Rüdiger Ohs für die zahlreichen Diskussionen, motivierenden Wort und sportlichen Aktivitäten. Schließlich danke ich meiner Frau Larissa, die immer ein besonderer Rückhalt während der Promotion gewesen ist. Ohne

ihren Rückhalt wäre die Arbeit in dieser Form nicht möglich gewesen. Vielen Dank!

*Für Larissa und Lia.*
*Für meine Eltern, für meine Geschwister und für meine Schwiegereltern.*

# Abstract

$H_2$ is regarded as a promising energy carrier and serves as an important raw material for the chemical industry. Up to now, $H_2$ is mainly produced by steam reforming of fossil resources. Besides their limited availability, tremendous $CO_2$ emissions are associated therewith. This demands for alternative production routes. For example, $H_2$ can be produced by fermentation processes using waste streams, which combines waste treatment with energy production. However, $H_2$ streams from biogenic origin also contain other by-products, e.g. $CO_2$, which must be removed before utilization. The separation of the gaseous by-products is a major cost driver for the $H_2$ production, but possible separation processes have only been analyzed insufficiently. In comparison to the conventional $H_2$ production, the feed for the gas treatment is present at ambient conditions and thus needs particular attention. Therefore, different separation processes were compared under technical and economic aspects.

Membrane-based processes are attractive for biohydrogen upgrading due to their high energy efficiency. They can reach high recoveries, but only a limited purity. In comparison, pressure swing adsorption (PSA) allow producing highly pure $H_2$ but suffer from low recoveries for bulk separation. Luckily, hybrid membrane-PSA processes allow combining both their advantages. However, the development of hybrid processes is very challenging due to the infinite number of process variants. Thus, an optimization framework for hybrid membrane-PSA separation is presented, which can identify optimal process designs with relatively little effort. In addition to optimizing the overall process, it is also possible to increase the efficiency of adsorption processes using hollow fiber adsorbents. Compared to conventional adsorption beds, they are characterized by a reduced mass transfer, a low pressure loss and defined flow conditions. In this work, an optimization model for hollow fiber adsorbers not only identified the optimal process but also the design of the hollow fiber itself.

Furthermore, the $H_2$ stream is often diluted by inert components, e.g. by $N_2$ for sparging of the fermentation. For diluted $H_2$ streams, compression of the feed gas is usually uneconomical. Thus, in the second part of the thesis, a process consisting of an electrochemical $H_2$ separation and temperature swing adsorption for the separation of $N_2$ and $CO_2$ is presented. The purified $N_2$ can then be recycled for sparging. Amine-functionalized sorbents are particularly suitable for the separation of the co-produced $CO_2$, which is present at low partial pressures. Yet, the adsorption kinetics for $CO_2$ for these materials have not been adequately described. This makes a detailed process analysis difficult. Therefore, a kinetics model for $CO_2$ adsorption was developed.

Finally, this work shows the influence of the $H_2$ fraction on the separation costs. The costs of the separation of diluted $H_2$ streams are more than four times higher than for high-concentrated $H_2$ streams. Thus, it is crucial that the biohydrogen production processes target designs with high $H_2$ fractions. With this thesis at hand, overall process analysis of the biogenic $H_2$ production is possible.

# Zusammenfassung

$H_2$ gilt als ein vielversprechender Energieträger und ist ein wichtiger Rohstoff für die chemische Industrie. Aktuell wird $H_2$ überwiegend mittels Dampfreformierung aus begrenzten fossilen Energieträgern gewonnen, wobei große Mengen $CO_2$ emitiert werden. Daher werden zahlreiche alternative Produktionsvarianten untersucht. $H_2$ kann fermentativ aus Abfallströme produziert werden, wodurch die Abfallverwertung zur Energiegewinnung genutzt wird. Hierbei fallen jedoch auch weitere Nebenprodukte, wie z. B. $CO_2$, an. Diese müssen für die Nutzung des Wasserstoffs aufwendig abgetrennt werden. Die Trennung der weiteren Gaskomponenten stellt dabei einen wesentlicher Kostentreiber dar. Bisher wurden mögliche Abtrennprozesse jedoch nur unzureichend betrachtet. Daher werden in dieser Doktorarbeit verschieden Trennprozesse unter technischen und ökonomischen Gesichtspunkten verglichen.

Membranprozesse sind für die Biowasserstoffaufbereitung sehr energieeffizient, können jedoch nur eine begrenzte Produktreinheit erzielen. Mittels Druckwechseladsorptionsprozessen kann zwar hochreiner $H_2$ gewonnen werden, die erzielbare Ausbeute bei der Bulktrennung ist aber limitiert. Hybride Membran-Adsorptionsprozesse kombinieren die Vorteile beider Technologien. Jedoch ist die Entwicklung solcher Prozesse aufgrund der Vielzahl an Verschaltungsvarianten sehr aufwendig. Im Rahmen dieser Arbeit wurde daher ein Optimierungsmodell für den hybriden Gastrennprozess entwickelt. Neben der Optimierung des Gesamtprozesses ist eine Effizienzsteigerung von Adsorptionsprozessen mittels sogenannter Hohlfaseradsorber möglich. Diese zeichnen sich im Vergleich zu konventionellen Adsorptionsbetten durch einen besseren Stofftransport, einem geringen Druckverlust und definierten Strömungsbedingungen aus. In dieser Arbeit wurden mit einem Optimierungsmodell nicht nur optimale Prozessparameter sondern auch Geometrien der Hohlfaseradsorber identifiziert.

Darüber hinaus ist der Wasserstoffstrom häufig durch inerte Komponenten, z. B. $N_2$, verdünnt. Dadurch ist eine Kompression des Feedgases oftmals unwirtschaftlich. Im zweiten Teil der Arbeit wurde ein Prozess aus einer elektrochemischen Wasserstofftrennung und einer Temperaturwechseladsorption für die Trennung von $CO_2$ und $N_2$ untersucht. Der aufgereinigte $N_2$, der häufig für die Begasung bei der fermentativen $H_2$-Produktion eingesetzt wird, kann somit recycelt werden. Amine-funktionalisierte Adsorbentien eignen sich besonders für die $CO_2$-Abtrennung bei niedrigen Partialdrücken. Die $CO_2$-Adsorptionskinetik dieser Materialien wurde bisher jedoch nur unzureichend beschrieben, wodurch eine detaillierte Prozessanalyse unmöglich ist. Deshalb wurde im Rahmen dieser Arbeit ein Kinetikmodell für die $CO_2$-Adsorption entwickelt.

Abschließend wurden die verschiedenen Trennprozesse miteinander verglichen. Der Vergleich zeigt, dass die Kosten für die Aufreinigung des Wasserstoffes bei Verdünnung vierfach höher sind. Es ist also notwendig, Biowasserstoffprozesse zu entwickeln bei denen der $H_2$ in möglichst hoher Konzentration vorliegt. Mit den vorgestellten Prozessstudien ist es nun möglich, die $H_2$-Produktion ganzheitlich zu betrachten.

# Contents

# 1 Introduction

## 1.1 Motivation



As shown in Figure 1.1, the worldwide energy production almost doubled since 1980. So far, the energy supply has mainly been satisfied by fossil resources. The increasing demand for energy has provoked the depletion of fossil energy resources, which also led to rising greenhouse gas emissions. Thus, alternative energy production routes must be developed. Until 2050, it is expected that about 50% of the world energy supply is provided by renewable energy sources (see Figure 1.1).

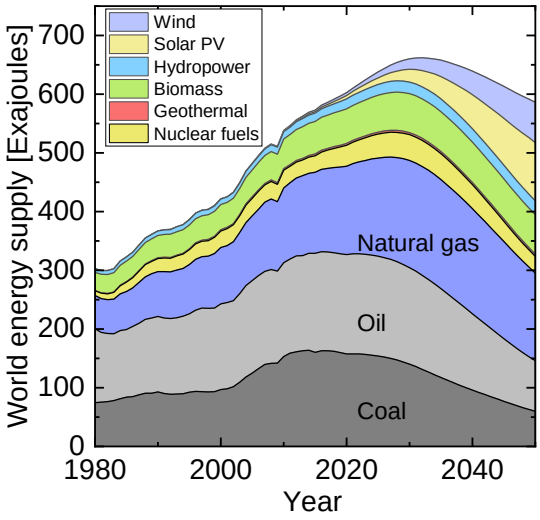


**Figure 1.1:** World primary energy supply by source [DNV 2017].

Hydrogen energy ($H_2$) is a promising candidate to drive the energy transition due to its high gravimetric energy density (122 kJ/g), non-polluting oxidative products and high conversion efficiency to usable power. Besides serving as a fuel, it can be used to balance the fluctuating energy supply by other sustainable production routes such as wind and solar power. Also, hydrogen is an important feedstock for the chemical industry, for example in the synthesis of ammonia. Nevertheless, the extensive utilization of hydrogen as a fuel is still hampered by technical challenges regarding its production, storage and distribution [Dunn2002; Levi2004]. Currently, hydrogen is mainly produced from fossil resources such as natural gas by steam reforming. In this process, significant amounts of $CO_2$ are produced as well

[LeVa2014]. Another route is the energy demanding electrolysis of water which (indirectly) depends on fossil energy sources. Due to an emerging market of $H_2$-powered vehicles or electricity production via fuel cells, the demand for hydrogen as a clean and sustainable energy source will inevitably increase. This increase, with regard to uprising climate changes, will trigger a market pull for a likewise clean and sustainable production of hydrogen from renewable resources, which is boosted by the drawbacks of currently prevailing production processes. Thus, alternative hydrogen production routes must be developed. With such processes, the energy supply becomes more climate-friendly and makes countries with fewer fossil resources independent of energy imports.



Hydrogen can be produced sustainably by bioprocesses, which circumvents the environmental drawbacks of conventional production routes and gives rise to a clean and renewable energy platform. Still, biohydrogen has a negligible share in the world-wide $H_2$ production and huge research efforts are made in improving the production technology [Elsh2013; Chan2015]. The main goal is to increase $H_2$ yields as well as productivities to overcome current practicability concerns [Levi2004]. Another issue is the separation of the produced $H_2$ from the accumulating gaseous mixtures in the headspace of the bioreactors [Bako2013a]. Besides the apparent reason of effectively capturing and purifying biohydrogen for further utilization, continuous $H_2$ removal is crucial to prevent microbial growth and an inhibition of $H_2$-biosynthesis by $H_2$ [Béla2006]. Vacuum operation and nitrogen sparging are beyond the most applied means to reduce the hydrogen partial pressure. There are several promising variants and concepts for the biohydrogen production by (micro-)organisms, but still, fundamental research on the integral production process has to be continued to increase its efficiency and applicability on an industrial scale [Sing2015; Arim2015; Chan2015]. This of course involves the separation and purification of $H_2$ from the gaseous mixtures produced during fermentation. Only by a combined consideration of all process steps that are needed to obtain a usable product, namely pure biohydrogen, the process as a whole can be effectively optimized [Bako2015]. However, the separation of biohydrogen on a

process scale has not been considered sufficiently yet. As the separation is a key energy consumer and cost driver, it needs particular attention to allow for an integral analysis of biohydrogen production routes.



## 1.2 Biohydrogen upgrading

Generally, raw biohydrogen is mostly a mixture of $H_2$, $CO_2$ and $N_2$ (if sparging is applied to reduce the inhibition by $H_2$ an $CO_2$). For practical applications, e.g. in fuel cells, the produced biohydrogen has to be purified (see Figure 1.2) and therefore, it needs to be effectively separated from the other components [Béla2006]. In fact, the separation of $H_2$ is often hampered by the inert gas sparging of the fermentation reactor, since it further dilutes $H_2$ in the product outlet stream.

For the separation of $H_2$ from $CO_2$ (and $N_2$), membrane gas separation processes are very attractive [Béla2006] due their low energy consumption [Sand2013], small footprints [Bern2009] as well as the possibility of a flexible operation [Scho2015a]. But, hydrogen utilization often requires high purities [Loff2003; Huft1999], which is usually difficult to archive using stand-alone membrane processes [Brun2010]. In comparison, pressure-swing adsorption (PSA) processes are well known and widely used for the production of highly pure hydrogen [Sirc2000a; Ohs2018b], but only exhibit low recoveries when bulk streams are separated [Ockw2007]. Consequently, hybrid separation processes combine the advantages of both separation methods [Li2016a] and often hybrid membrane-PSA are more beneficial than stand-alone membrane processes [Sirc1999; Ockw2007; Este2002; Este2007]. However, the design if hybrid processes is challenging and heuristic and iterative process development usually result in suboptimal process designs. Thus, advanced process developments are necessary to exploit the benefits of both technologies fully.

Furthermore, temperature-vacuum swing adsorption (TVSA) processes gained increasing attention for carbon capture and direct air capture processes due to their low energy consumption. With further material and process development, TVSA processes are also attractive for biohydro-

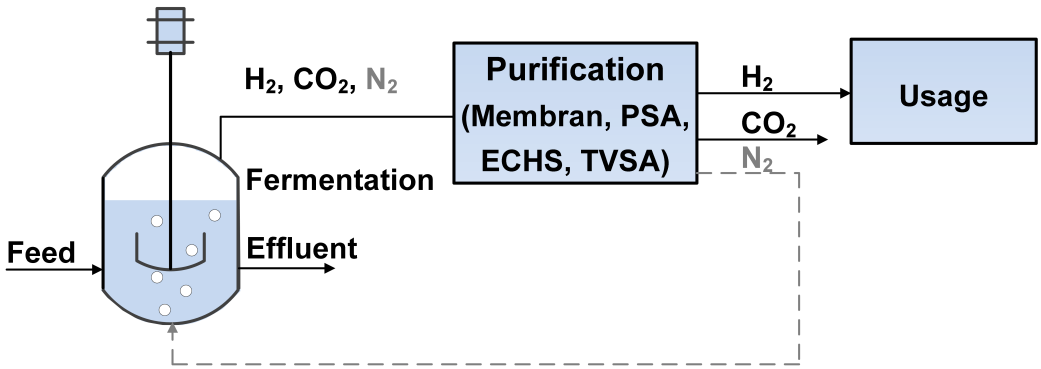


**Figure 1.2:** Separation of hydrogen from $CO_2$ and nitrogen, if sparging is applied.

gen recovery. In particular, novel amine-functionalized materials show very high $CO_2$ adsorption capacities [Mell2011], are tolerant to moisture in the feed [Liu2011] and are very selective towards $CO_2$ in gas mixtures even at low $CO_2$ concentrations [Belm2009; Belm2010a; Kell2018]. However, precise and versatile models describing the adsorption kinetics of this materials are still missing. Recently, electrochemical hydrogen separation emerged as a method to produce highly pure hydrogen even from low hydrogen feed fractions as any compression of the feed stream is required. In such processes, molecular hydrogen is oxidized at the cathode [Sedl1981]. Due to the potential gradient, the protons diffuse toward the anode where they are reduced to molecular hydrogen again. Combining electrochemical hydrogen separation and temperature-vacuum swing adsorption processes thus allow an energy efficient hydrogen upgrading without any compression of the bulk stream. So far, a process combining these two promising technologies has not been presented.

Hydrogen is a very valuable gas which is often used at high purities. This makes the design of separation processes challenging and usually different separation technologies must be combined to achieve both high purities and recoveries. So far, efficient separation processes have only been investigated insufficiently for biohydrogen separation. Thus, this thesis analyzes different separation technologies regarding energy consumption and

costs. In particular, it is investigated if biohydrogen separation is economically feasible and evaluated how much energy provided by the hydrogen is consumed by the separation process. Hereby, one of the key question is how nitrogen sparging influences the separation efficiency and costs.



## 1.3 Outline of this thesis

Biohydrogen is a mixture of $H_2$ and $CO_2$, as well as $N_2$ if sparging is applied. To make biohydrogen separation economically and energetically feasible, efficient separation processes are required. This thesis presents process design methods which allow optimizing and comparing the different technologies. A comparison of the various processes has been a missing part in the research on biological hydrogen production.

Figure 1.3 depicts the outline of this thesis. First, Chapter 2 provides a short review of biohydrogen production and separation. In particular, the current research of relevant separation technologies is summarized. For biogydrogen separation, the influence of nitrogen sparging on energy consumption and separation cost is one of the most important issues. Thus, the thesis is separated into two parts.

Part A (Chapter 3 and 4) focuses on processes where only $H_2$ and $CO_2$ are present in the feed gas mixture. Hybrid membrane-PSA processes promise to achieve both high recovery and purity. However, the design of such hybrid processes is intricate and challenging due to the large variety of possible process configurations. To solve this challenge, an optimization model for the design of hybrid membrane-PSA processes is presented in Chapter 3. As the overall optimization of the process with a dynamic adsorption model is not possible, a simple but precise short-cut model is developed. This allows identifying an optimal process from a large number of possible process configurations such as optimal process layouts, recycle streams and operation condition. It is also investigated how the feed composition influences the process design.

Besides overall process optimization, adsorption processes can further be improved by hollow fiber sorbents, which show lower pressure drops,

higher mass transfer and well-defined flow conditions. The hollow fiber design gives an additional degree of freedom for process development. So far, process and fiber optimization has not be combined. Thus, Chapter 4 presents an optimization model which does not only allow identifying an optimal process, but also the optimal fiber design. This includes the fiber dimensions such as fiber length, fiber diameter as well as fiber wall thickness. Furthermore, it is investigated how these parameters vary for different process condition.



Unfortunately, $H_2$ as well as $CO_2$ inhibit the biohydrogen fermentation. Thus, $N_2$ sparging is often applied to reduce their partial pressure. This makes the hydrogen recovery even more challenging. Part B of the thesis (Chapter 5 and 6) analyzes the separation of $H_2$, $CO_2$ and $N_2$. For such diluted hydrogen streams, the compression of the bulk stream is not possible. Furthermore, also the $CO_2$ stream has to be separated for $N_2$ recycling. Amine-functionalized solid sorbents are promising materials for this task due to their outstanding adsorption capacities at low $CO_2$ partial pressures. However, only limited studies about the adsorption kinetics have been presented and the adsorption behavior of these materials cannot be described by conventional kinetic models, which makes the process design impossible. Thus, a semiphysical dual kinetic adsorption model, which is both simple and precise, is developed in Chapter 5. It is also evaluated if the model can be applied to various types of amine-functionalized solid sorbents and how the model parameters change for different preparation methods.

With this model at hand, Chapter 6 analyzes a separation process based on an electrochemical separation unit for hydrogen removal as well as temperature-vacuum swing adsorption unit for $CO_2$ separation from nitrogen. For the electrochemical hydrogen separation unit, a cell voltage balancing the stack size and energy consumption is identified. For the temperature-vacuum swing adsorption unit, usually only the energy consumption is considered as process criteria. However, it is shown that also the volume specific throughput has to be considered.

Chapter 7 summarizes the findings of the aforementioned chapters and

compares the different technologies. In particular, the influence of the feed composition on the process costs is shown. Furthermore, the challenges and limitations of the thesis are discussed. Finally, an outlook for future research and starting points for upcoming investigations are given.



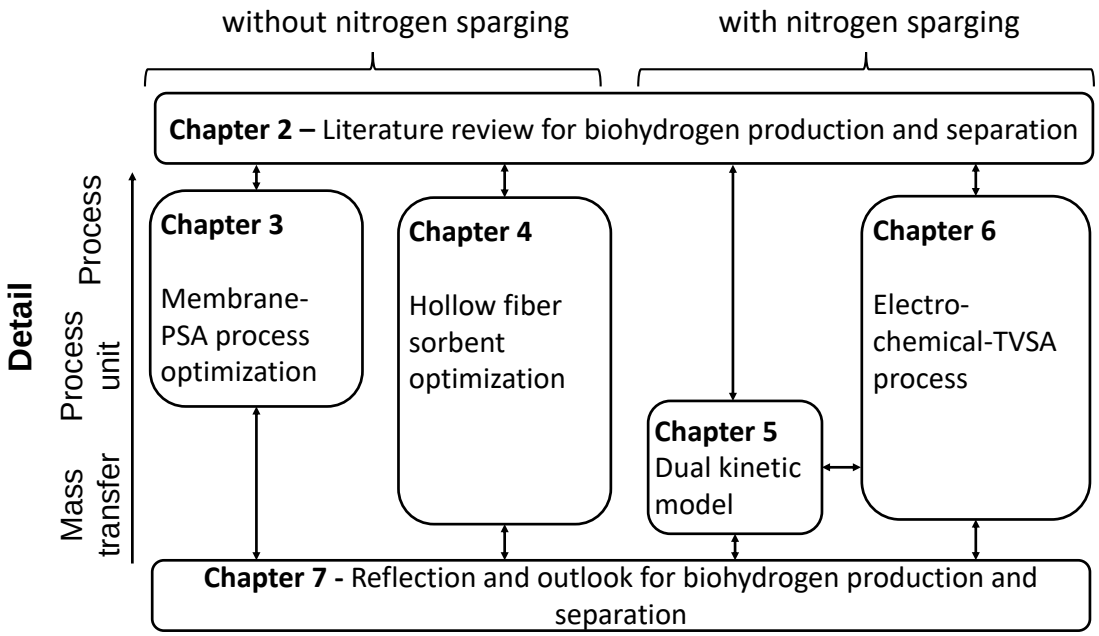


**Figure 1.3:** Structure of this thesis.

# 2 Literature review of biohydrogen production and separation

## 2.1 Sustainable hydrogen production



A sustainable energy and feedstock supply remains one of the major challenges of today's society [Lund2007; Chu2012; Turn2004; Milt2010]. Hydrogen ($H_2$) is a very promising energy carrier for the future [Barr2003] and is also an important feedstock for the chemical industry [Stol2016], e.g. for ammonia and methanol production. Currently, it is mainly produced from fossil resources such as coal and natural gas [Venn2011]. For a more sustainable future, alternative production routes must be developed [Edwa2008]. Many options, such as electrochemical [Carm2013] or photocatalytic water splitting [Maed2010; Kudo2009], are currently investigated. Alternatively, $H_2$ can also be produced by fermentation processes in which renewable feedstocks, such as waste streams, can be used [Levi2004; Kapd2006; Dine2018; Wang2018]. This route allows combining waste treatment and energy production and is thus particularly attractive [Han2017; Kapd2006]. Several process variants exist for the biological production of $H_2$, including direct and indirect biophotolysis as well as photo- and dark-fermentation [Das2001]. Dark-fermentative production under anaerobic conditions is the most popular option of these alternatives due to its potential high $H_2$ production rate, high stability as well as its simple instrumental setup and control requirements [Das2008; Elsh2013].

Unfortunately, the $H_2$ fermentation is inhibited by the produced hydrogen [Nath2004; Guo2010; Oh2009]. Thus, methods to reduce the $H_2$ partial pressure, such as vacuum operation or nitrogen sparging, have been investigated [Kim2006; Lee2012; Mizu2000; Nguy2010]. However, these methods decrease the energy efficiency of the biohydrogen production significantly because the $H_2$ purification becomes challenging at high degrees of dilution [Ramí2013]. Furthermore, $CO_2$ is produced as well in such a process, which must be removed before $H_2$ utilization.

## 2.2 Hydrogen separation

As the separation of the product gas is energy consuming and costly, it is crucial to develop an efficient process to make biohydrogen production economically attractive. Furthermore, the concentration and volume flow rates of $H_2$ and $CO_2$ in biohydrogen streams differ from other separation processes such as steam reforming or carbon capture. Also, decentralized production plants require a simple process design and a low plant footprint. Thus, $CO_2$ removal from biohydrogen streams requires additional attention. Processes based on polymeric membranes [Bako2013a; Hara2007; Horv2004; Neve2009; Bako2015], amine absorption [Mass2016], membrane contactors [Modi2008; Tepl2002] as well as electrochemical methods [Mass2016] have been investigated for $H_2$ upgrading. So far, research on biohydrogen separation mainly focuses on hydrogen enrichment up to 90% [Bako2013a; Béla2006; Bako2013b; Bako2015]. Yet, a design study for the production of highly-pure hydrogen from biogenic origin has not been presented.



### 2.2.1 Hybrid membrane-pressure swing adsorption

Membrane processes have already been commercialized for gas separation, such as natural gas treatment, air separation [Bake2014] and biogas upgrading [Scho2013a]. In comparison to conventional separation tasks, they show many benefits such as low energy consumption [Sand2013], small footprints [Bern2009] as well as the possibility of flexible operation [Scho2015a]. Conventional membranes separate gaseous compounds by their differences in molecular weight and diffusivity [Bako2013a]. A measure for the permeation of a (pure and homogeneous) component through a specific membrane(-material) is given by the permeance $Q$. Regarding hydrogen separation efficiency, the ratio in $Q$, namely the selectivity, between $H_2$ and the remaining components in the gas stream (mainly $CO_2$ and $N_2$), as well as $Q_{H_2}$ itself, should be as high as possible. Several membrane materials, most often on a polymer basis, have already been reported to ex-

hibit good permeabilities and selectivities for $H_2$ [Béla2006]. Unfortunately, multi-stage processes are required to achieve both high purities and recoveries [Bake1998; Huan2014]. In such processes, recompression is one of the primary cost drivers and optimizing membrane processes is crucial to balance compression costs, membrane costs and recovery [Bake2014]. Due to the large variety of possible process configurations, developing the optimal process design represents a challenging task. Recently, advanced optimization methods have been developed to find optimal process configurations and conditions for multi-stage membrane processes [Qi1998; Scho2015b; Ohs2016; Alsa2017a; Alsa2017b].



Over the last decades, pressure swing adsorption gained commercial acceptance as an energy-efficient gas separation technique [Ruth1994]. Major applications are the recovery of high purity hydrogen [Sirc2000a], natural gas treating [Tagl2009] as well as air separation [Haya1996]. In comparison to other separation methods, PSA is often advantageous due to its simple operation [Ho2008], its high flexibility [Sirc2002], its possibility to tailor adsorption materials to the specific separation task [Li2009] and its low energy consumption, because any phase change is involved. However, to improve overall process performance, e.g. energy demand and recovery, additional improvements are required. Currently, research focuses on process optimization [Ko2003; Ko2005; Jian2003; Agar2010; Hasa2013], material design [Li2009; Choi2009] as well as the development of structured adsorbents [Mosc2008; Reza2010a; Reza2010b]. Hydrogen utilization often requires high purities [Loff2003; Huft1999], which usually results in high costs using stand-alone membrane processes [Brun2010]. In comparison, pressure-swing adsorption processes are well known and widely used for the production of highly pure hydrogen [Sirc2000a; Ohs2018b], but only exhibit low recoveries when bulk streams are separated [Ockw2007]. Consequently, hybrid separation processes have been investigated to combine the advantages of both separation methods [Li2016a]. It has been shown that hybrid processes outperform both stand-alone PSA as well as stand-alone membrane processes [Sirc1999; Ockw2007; Este2002; Este2007]. However, the design of such hybrid processes is intricate and challenging

as the PSA unit gives additional degrees of freedom. As membrane and PSA processes are complementary separation steps, each with its advantages and disadvantages, it is essential to exploit their synergies fully. While developing hybrid membrane-PSA separation processes, for example the following questions must be addressed:

- To which degree does the separation take place in the membrane and the PSA process, respectively?
- Are recycle streams necessary?
- Is the process scheme influenced by the feed composition?



Commonly, two design methods are applied:

- 1. Black-box approach: The PSA unit is modeled as a simple splitter [Ockw2007; Ocho2007; Carr2010]. Particularly, this approach is used for intricate production systems combining many operations steps.
- 2. Iterative approach by subsequent simulation of the two process steps: In a first step, a membrane process is simulated. Subsequently, the PSA process is calculated using the outflow of the membrane unit as the inflow. Often, the tail gas of the PSA process is recycled to the membrane process and then the membrane process must be simulated anew. The subsequent simulation of the two process steps is repeated until convergence is achieved [Sirc1999].

For the black-box approach, detailed information about the PSA process is missing. For instance, the performance of the PSA process depends on the pressure level of the membrane process and the particular feed composition. Thus, finding the optimal process design with a simple splitter function is impossible. In comparison, the second approach is very time and calculation-intensive since it is challenging to investigate all potential process configurations iteratively. Nikolić et al. presented an optimization framework for hybrid PSA-processes [Niko2015] which optimizes the recovery of the process. In contrast, hydrogen from biogenic origin is available at ambient pressure and temperature only. Thus, the compression costs for

the separation are critical and require the pressure levels to be included in the process development and optimization. To solve this challenge, more advanced process development methods such as global optimization are necessary. These methods allow identifing the optimal process design from a large variety of possible solutions. This means to find the best process structure and operation conditions as presented in Chapter 3.



### 2.2.2 Hollow fiber sorbents

Besides developing hybrid processes, adsorption processes can be improved by hollow fiber sorbents, which promise to overcome some of the fundamental shortcomings in swing adsorption. They have first been introduced by Feng et al. [Feng1998], who filled the shell side of a common hollow fiber microporous membrane module with adsorbent particles. The gas stream flows through the lumen side of the fibers resulting in lower pressure drops and lower mass transfer resistance compared to conventional packed-bed reactors. Controlled flow distribution under laminar conditions led to sharper breakthrough curves and thus higher recoveries.

Furthermore, adsorptive particles were immobilized in membrane fiber walls. These fibers are produced by membrane fiber spinning technology using both a polymer binder as well as high loadings of adsorbent fillers. This concept was first presented by Avramescu et al. for liquid-based adsorption, i.e. preparative chromatography applications [Avra2003]. Later, Lively et al. applied this approach for adsorptive membrane gas separation [Live2012a; Bhan2013; Labr2014]. A simultaneous co-extrusion process can form an additional sheath layer made of low permeable polymer. This layer prevents any gas losses and a thermal moderator (e.g. wax) on the outside can facilitate isothermal operation [Live2012a]. Experimentally, it was shown that hollow fiber sorbents could outperform conventional packed-bed reactors [Live2012b]. The simple scalability and high flexibility due to the modular design of hollow fiber sorbent modules are particularly attractive for small-scale processes with varying feed conditions [Kaly2015]. Other novel hollow fiber sorbents, such as microtubes based

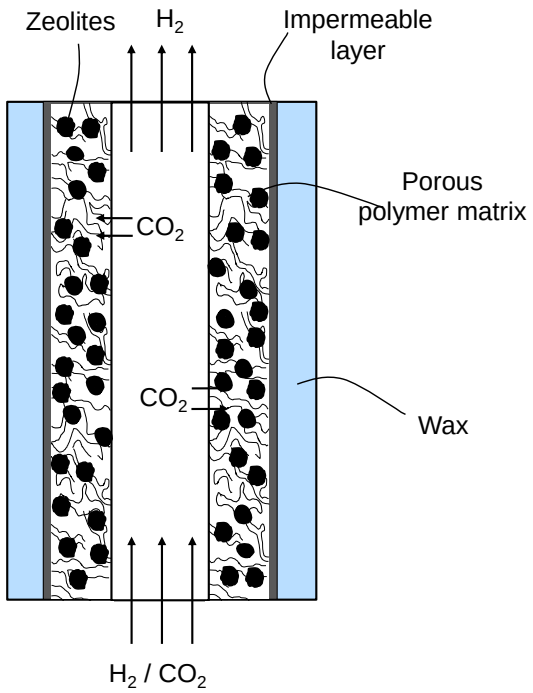


**Figure 2.1:** Scheme of a hollow fiber sorbent consisting of a hybrid zeolite-polymer fiber and an impermeable sheath layer with a thermal moderator for isothermal operation.

on PEI-functionalized carbon nanotubes, may be applied as well [Kell2018].

Using hollow fiber sorbents provides additional design freedom for adsorption processes as not only the process but also the fiber itself can be adjusted to the specific separation tasks. This includes the optimal fiber length, diameter and wall thickness. Holistic design methods allow exploiting their potential fully and decreasing energy consumption and costs. But today, rigorous modeling and optimization efforts of the PSA process as well as the hollow fiber geometry itself are still missing [Reza2014]. Such an integrated design method as well as a comparison with conventional packed-bed reactors are presented in Chapter 4.

### Amine-functionalized solid sorbents

As described above, the separation of $CO_2$ is a critical step for sustainable hydrogen upgrading. In general, the reduction of $CO_2$ emissions is also one of the most important technological challenges of the future [Inte2015]. Adsorption-based processes have already been proposed for the separa-

tion of $CO_2$ from flue gas, natural gas and even from ambient air [DAle2010; Choi2009; Saya2011; Ntia2016; Keit2009]. However, commercially available sorbent materials often lack either high adsorption capacity or selectivity, in particular when humid streams are separated [Wang2014; Belm2010b]. Consequently, researchers are actively exploring more efficient $CO_2$ sorbent materials. In particular, amine-functionalized solid sorbents are very promising materials. They show very high $CO_2$ adsorption capacities [Mell2011], are tolerant to moisture in the feed [Liu2011] and are very selective towards $CO_2$ in mixtures with nitrogen, methane, oxygen or hydrogen even at low $CO_2$ concentrations [Belm2009; Belm2010a; Kell2018]. In comparison to absorption-based amine $CO_2$ separation, an adsorption process does not require to heat the bulk solvent and thus needs less heating energy [Dutc2015].

Depending on their preparation method, solid amine sorbents can be divided into three classes [Sama2012]: (i) chemical grafting of amines or amine-functional groups on the surface of the solid support (ii) physical amine impregnation on solid sorbents and (iii) a hybrid of the two other classes, where the amines are physically loaded on the solid support and then polymerized in-situ. The rigorous design and optimization of processes require kinetic models of these adsorption materials. In this regard, simple but precise kinetic models for amine-functionalized solid sorbents are needed to describe their behavior and fully exploit their potential. Recently, an increasing number of studies regarding the influence of functionalization methods on adsorption capacities and adsorption kinetics have been published [Mona2013; Belm2009; Zhao2013; Zele2008; Liu2014]. The functionalization method, the amine type, the amine loading as well as the porous solid support are among the most critical parameters for adsorption capacity and kinetics [Hiyo2005; Heyd2011a; Son2008]. However, only limited studies regarding models for the adsorption as well as desorption kinetics of $CO_2$ on amine-functionalized materials exist [Liu2014; Sern2010; Heyd2011b; Zhao2013]. The kinetics of $CO_2$ adsorption on solid sorbents are affected by several molecular processes occurring simultaneously such as film diffusion, intra-particle diffusion and adsorbate

interaction with active sites (physisorption and/or chemi-sorption with reactions of higher order) [Heyd2011b; Boll2012b]. Bollini et al. used Toth and Langmuir isotherms to account for the different adsorption sites [Boll2012a; Boll2012b] and used linear driving force expressions to describe the mass transfer rate. Hereby, they assumed that the rate limiting processes are based on diffusional mechanisms. But, these studies did not provide any information on the desorption kinetics [Abdo2015]. Recently, detailed mechanistic kinetic models have been discussed, but they are too complex for process simulation and optimization [Abdo2015]. In fact, a large number of kinetic parameters and their temperature dependencies have to be determined. To avoid (a) the uncertainty in the parameters of such complex models and (b) their lack of numerical stability in process simulations, the different adsorption steps are usually summarized by an overall mass transfer resistance for semi-empirical models. Serna-Guerrero et al. showed that pseudo-first-order (PFO) and pseudo-second-order kinetic models (PSO) have some limitations describing the adsorption of $CO_2$ on amine-functionalized materials [Sern2010]. In comparison, Avrami's fractional-order kinetic model (AFO) [Sern2010] and the generalized fractional-order kinetic model (GFO) [Heyd2011b] are able to describe the $CO_2$ uptake of amine-functionalized solid sorbents accurately. However, for these two models the $CO_2$ uptake is a power function of the time and consequently the effective kinetic coefficient increases with adsorption time. Thus, these two models have the following physical limitations:

(i) In Avrami's model and the generalized fractional-order kinetic model (see equation 5.2 and 5.3), the effective adsorption kinetics are an exponential function of the adsorption time. Therefore, the effective adsorption coefficient becomes infinitely large at long adsorption times. Actually, it should remain within reasonable bounds.

(ii) The identified adsorption parameters for Avrami's model and the generalized fractional-order kinetic model depend on the $CO_2$ mole fraction of the gas phase and the sorption temperature applied. Mostly, a systematic relationship of these parameters cannot be ob-

served [Heyd2011b] (see also Table 5.1). Thus, the kinetics can only be used for the specific parameters investigated during the experimental studies, i.e. a particular temperature and concentration.

(iii) Avrami's model and the generalized fractional-order kinetic model can be used to describe the initial loading of amine-functionalized materials. However, in cyclic adsorption processes adsorption and desorption takes place. Usually, the sorbent is not fully regenerated because this would result in long cycle times. If the adsorption time of Avrami's model and the generalized fractional-order kinetic model restarts, it is expected that the kinetic parameters identified for the initial loading do not allow describing the $CO_2$ uptake of already (partially) loaded sorbent materials.



Additionally, the time-dependent definition of the adsorption kinetics makes the simulation of adsorption processes challenging:

(i) Kinetic adsorption studies use thermogravimetric methods at isotropic conditions due to small sample sizes. However, in adsorption beds axial (and radial) temperature and concentration gradients are present. Thus, the adsorption time in the uptake kinetics has to be defined separately for each location in the adsorption bed. For Avrami's model and the generalized fractional-order kinetic model there is no explicit criteria for the start of the local adsorption time, which makes the choice of a starting point rather arbitrary. In particular, this is relevant for cyclic adsorption processes with incomplete regeneration and thus different initial conditions as in simple kinetic experiments.

(ii) For Avrami's model, the desorption has been described as an exponential function of time. As for the adsorption step, the desorption time has to be defined separately for each location of the bed because high temperature and concentration gradients exist.

(iii) In comparison to thermogravimetric measurements the temperature in column adsorption beds increases and decreases slowly during heating and cooling, respectively. Often the heating and cooling time can

be in the range of the desorption period [Tlil2009; Clau2011]. Thus, the desorption function has to be defined individually for each location in the adsorption bed. This is not an intrinsic limitation of the adsorption model, but makes modeling very inconvenient, since an (arbitrarily) chosen desorption time has to be defined for each location.

Thus, we develop a new, simple and versatile model that describes adsorption kinetics of $CO_2$ on amine-functionalized solid sorbents (Chapter 5). To show its general usability, we tested the model for different types of solid support materials and functionalization methods.



### 2.2.3 Electrochemical hydrogen separation

Recently, Massanet-Nicolau et al. showed that an electrochemical process for hydrogen separation combined with amine scrubbing for $CO_2$ removal can improve the efficiency of $N_2$-purged biohydrogen fermentations [Mass2016]. Such a process does not require the compression of the bulk stream. Electrochemical hydrogen separation allows producing highly pure hydrogen even from low hydrogen feed fractions. In this process, molecular hydrogen is oxidized at the cathode [Sedl1981]. Due to the potential gradient, the protons diffuse toward the anode where they are reduced to molecular hydrogen again. Electrochemical hydrogen separation processes only require small overpotentials to separate $H_2$ from gas mixtures. In particular, electrochemical hydrogen separation has already been investigated for (1) $H_2$, $N_2$ and $CO_2$ separation [Mass2016], (2) $H_2$ and $CH_4$ separation, where $H_2$ is injected into the natural gas grid and then separated at the point of usage[Ibeh2007], (3) reformate stream separation derived from hydrocarbon sources [Abdu2011]. As a novel separation method, it has not been investigated:

- Which stack size is required for relevant process streams?
- What are ideal cell voltages for important process criteria such as volume-specific throughput and energy efficiency?

- How are these process parameters influenced by the energy and stack price?

These questions can only be answered by a detailed process analysis which is presented in Chapter 6 for the first time.

# 3 Optimizing hybrid membrane-pressure swing adsorption processes for biogenic hydrogen recovery



Parts of this chapter have been published as:

Burkhard Ohs, Martin Falkenberg, Matthias Wessling
*Optimizing hybrid membrane-pressure swing adsorption processes for biogenic hydrogen recovery*, Chemical Engineering Journal, 2019
DOI: 10.1016/j.cej.2019.01.136

## 3.1 Introduction

Membrane and pressure swing adsorption processes are considered as energy-efficient separation technologies but only reach limited purities or recovery, respectively. In comparison, hybrid processes allow combining the benefits of both technologies. However, the design of hybrid processes is challenging. To address this challenge, first a semi-physical, but precise short-cut-model for the pressure swing adsorption unit is developed. With this short-cut model at hand, optimization based on mixed-integer-nonlinear programming (MINLP) identifies the optimal design of a hybrid membrane pressure swing adsorption process depending on the pressure conditions chosen. To showcase the methodology and to investiagte how the feed composition influences the process design, three different feedstocks with varying $H_2$ contents are considered ($H_2$ feed fraction of 25, 50 and 75 mol-%).

## 3.2 Optimization approach

As discussed above, developing hybrid membrane PSA processes is challenging. To meet this challenge, we present an optimization framework for hybrid membrane-PSA processes using mixed-integer-non-linear programming. The optimization model consists of [Ohs2016]:

- A process structure with connect-options to allow for different process configurations, e.g. recycle points [Skib2012],
- Physical equations describing the various process units, i.e. compressors, membranes and PSA,
- Cost correlations and economic calculations, e.g. investment costs and present value calculations,
- Technical boundary conditions, e.g. minimal required recovery and purity,
- Process and cost parameters, e.g. feed flow rate and $H_2$ price.

With this framework, we can evaluate a large number of potential process configurations and identify the best design resulting in the lowest costs. So far, many optimization studies often focus on identifying the process design with the lowest energy demand. However, identifying the economic optimum is of higher practical relevance as the energy demand, which can often be reduced by providing more membrane area and/or adsorber size.

### 3.2.1 Process model

Figure 3.1 provides a schematic of the generic flow sheet. It represents all potential process configurations investigated in this chapter. For the bulk separation, we consider a two-stage membrane process using $CO_2$-selective membranes (see stage 1 and stage 2 in Figure 3.1). This type of membranes typically exhibit higher selectivities and permeabilities compared with $H_2$ selective membranes. Additionally, for $CO_2$ selective membranes, the hydrogen remains on the high-pressure side which avoids repressurization of the hydrogen-rich stream for the PSA unit, which produces highly-pure hydrogen. Furthermore, recycling the tail gas of the PSA unit may increase the overall recovery of the process [Sirc1999]. The recycle stream can also pass a third membrane unit. The optimization model then identifies the best process configuration, i.e. the process configuration resulting in the lowest cost, and answers the following questions:

- To which degree does the separation take place in the membrane and in the PSA unit, respectively?
- Which membrane unit is required and what is its optimal membrane area?
- What is the optimal system pressure?
- Where are the optimal recycle locations and what are the recycle rates?
- What is the optimal size of the adsorption bed?
- Where is the waste stream purged out of the system?

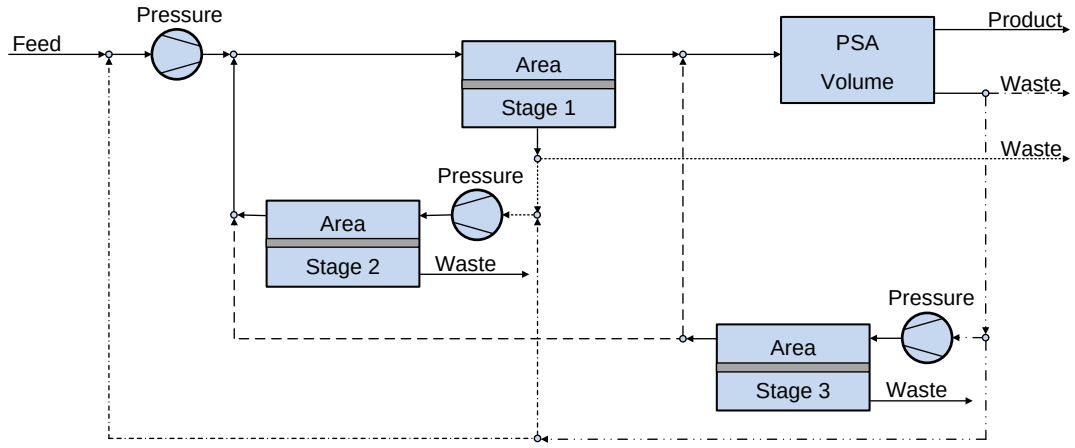


**Figure 3.1:** Schematic representation of the process model. The optimization model identifies the process structure, the optimal membrane area, the optimal adsorber size, recycle locations and system pressure.

## 3.2.2 Unit operations

In this chapter, the hybrid separation process comprises three process entities: compressors, membrane units and a PSA unit. We present the governing equations in the following.

### Membrane module

In this chapter, we implemented a discretized model, which is applicable for global optimization, to describe the gas separation within a membrane module [Scho2015b; Ohs2016; Alsa2017b]. The following equation describes the local flux along a counter-current hollow fiber membrane module:

$$\dot{n}''_{i,j} = Q_i \cdot (p_{R,i,j} - p_{P,i,j}) \tag{3.1}$$

with $\dot{n}''_{i,j}$ as the local flux of component $i$ through the membrane within the discretization element $j$, $Q_i$ as the permeance of the membrane for component $i$ and $p_{R,i,j}$ as well as $p_{P,i,j}$ as the partial pressure of component $i$ within the discretization element $j$ on the retentate and the permeate side, respectively. The molar balance for both the retentate and permeate is then

described by (see also Figure 3.2) [Scho2015b; Ohs2016; Alsa2017b]:

$$\Delta \dot{n}_{R,i,j} = -\dot{n}^{"}_{i,j} \cdot W \cdot \Delta z \tag{3.2}$$

and

$$\Delta \dot{n}_{P,i,j} = -\dot{n}^{"}_{i,j} \cdot W \cdot \Delta z \tag{3.3}$$

where $\dot{n}_{R,i,j}$ and $\dot{n}_{P,i,j}$ denote the flow rate at the discretization element $j$ on the retentate and permeate side, respectively, $W$ the total width of the membrane module, i.e. the sum of the circumference of all fibers, and $\Delta z$ the length of the discretization element. In this chapter, ten discretization elements and polymeric membranes with a $CO_2$ and $H_2$ permeance of 1000 GPU and 85 GPU, respectively, are used [Lin2014]. The permeance and selectivity of the membrane may be influenced by a high $CO_2$ partial pressure as well as the presence of minor components [Lin2014]. However, in this chapter these effects have not been taken into account, but should be investigated in subsequent studies.

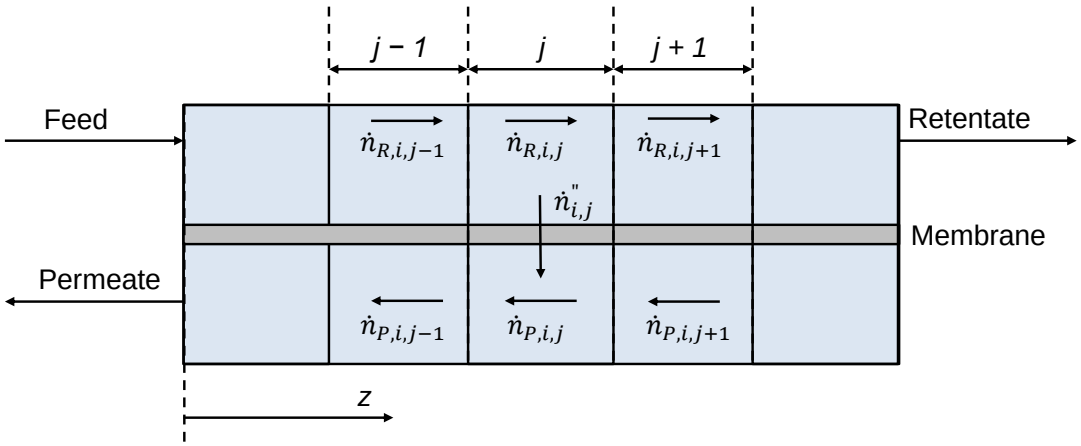


**Figure 3.2:** Schematic representation of the discretized membrane unit.

### Semi-physical short-cut model for pressure swing adsorption unit

Due to their dynamic character, it is very challenging to simulate PSA processes, which is even more difficult for hybrid processes as the complexity further increases. To circumvent this problem, we developed a semi-physical short-cut model for the PSA unit, which we derived from a rigorous PSA process simulation at cyclic steady state conducted in Aspen Adsorption™. The rigorous PSA process uses a state-of-the-art eight step adsorption cycle (see Figure 3.3). The longer cycle steps (adsorption & supply, purge pressurization, regeneration, purge) have a duration of 100 s. In comparison, the shorter cycle steps (adsorption & feed pressurization (AD & FP), blowdown (BD), pressure equalization (PE)) are only 30 s long.



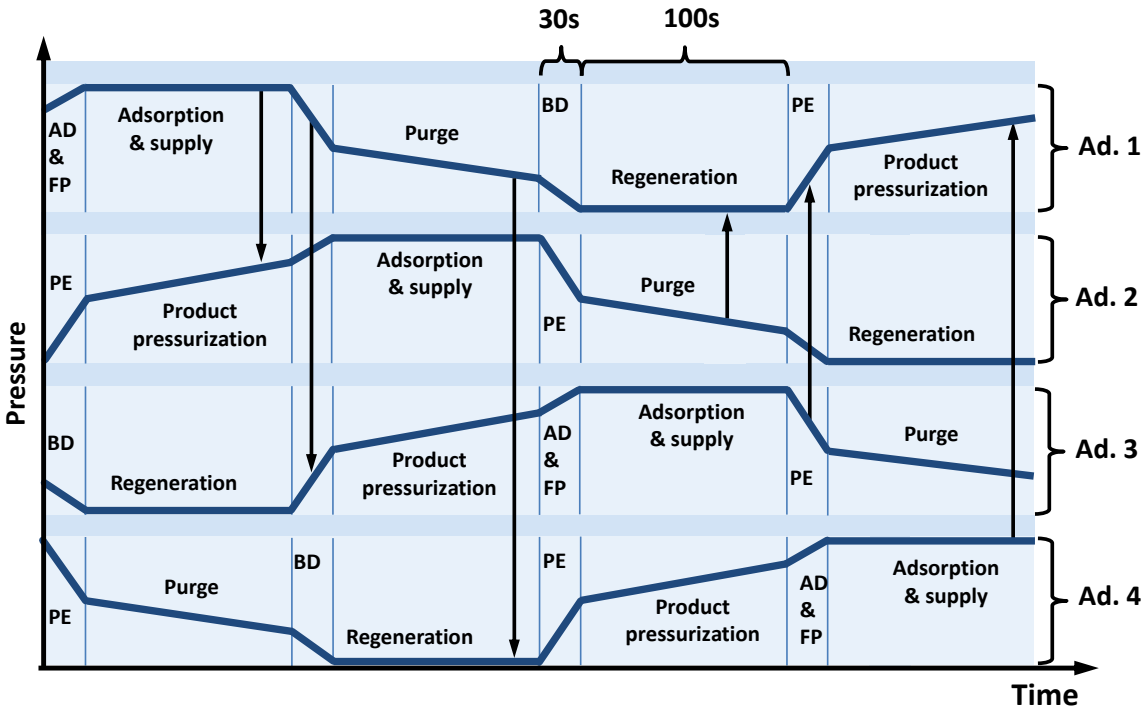


**Figure 3.3:** Pressure trajectories during the eight steps of the adsorption cycle. Here AD stands for adsorption, FP for feed pressurization, DP for depressurization, BD for blowdown and PE for pressure equalization. The scheme was adapted from [Lind2016].

For the rigorous simulation of the adsorption process conducted in Aspen Adsorption™, we assumed the following:

- the gas phase obeys the ideal gas law,
- no radial variation in gas concentration, temperature and pressure exists,
- the axial pressure drop in the column is described by the Ergun equation,
- the porosities of both the adsorption bed and the adsorbent particles are uniform along the bed,
- the inter-phase mass transfer coefficient is described by the diffusion pore model,
- the adsorption isotherm is described by the extended Langmuir model



The governing equations for the cyclic adsorption are given in [Li2016b]. As discussed above, the simulation of PSA is challenging and incorporating dynamic PSA models into integrated process simulation is almost impossible. Thus, Chung et al. proposed a short-cut model for adsorption-based $CO_2$ separation [Chun1998]. However, the short-cut model overestimates the PSA performance and was designed for a process in which the adsorbate represents the product [Chun1998]. Based on the work of Chung et al., we developed a novel short-cut model for the cyclic steady state that is specifically designed to describe processes in which the non-adsorbed component represents the product. Furthermore, the model also takes non-ideal effects such as mass-transfer zones into account. A schematic principle of the novel model is given in Figure 3.4. The model divides the PSA cycles into an adsorption and a desorption step denoted by the subscripts ‘ad‘and ‘de‘, respectively. For both steps, the equilibrium between the gas and the solid phase is assumed. At the beginning of the adsorption step, the packed-bed is in the state of desorption, wherein $n_{g,de}$ is the amount of gas present in the gas phase of the adsorption column and $n_{s,de}$ represents the amount of gas adsorbed on the solid phase. During the adsorption step, the feed $n_f$ is fed into the column. The amount of gas molecules present in the gas phase at the end of the adsorption step is denoted by $n_{g,ad}$ and the amount of adsorbed molecules by $n_{s,ad}$. The amount

$n_{out}$, which is withdrawn during the adsorption step, is split into the amount used for purging $n_{purge}$ and the amount representing the product $n_{prod}$. The overall mass balance for the adsorption step is thus given by:

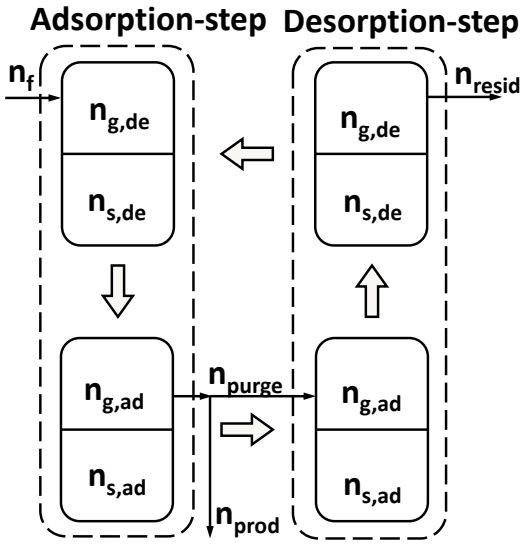


**Figure 3.4:** Schematic representation of the short-cut model for PSA unit.

$$n_f + n_{g,de} + n_{s,de} = n_{g,ad} + n_{s,ad} + n_{out} \tag{3.4}$$

and for component $i$:

$$n_{f,i} + n_{g,de,i} + n_{s,de,i} = n_{g,ad,i} + n_{s,ad,i} + n_{out,i} \quad \text{for i: N-1} \tag{3.5}$$

with $N$ as the number of components in the system. Equivalently, at the beginning of the desorption step the amount of molecules in the gas phase is $n_{g,ad}$ and the amount of gas molecules adsorbed is $n_{s,ad}$. $n_{res}$ is the amount of gas leaving the column as tail gas. Additionally, $n_{purge}$ is fed into the column during desorption to improve regeneration of the column. This leads to the following equation for the overall mass balance for the desorption step:

$$n_{purge} + n_{g,ad} + n_{s,ad} = n_{g,de} + n_{s,de} + n_{res} \tag{3.6}$$

and for component $i$:

$$n_{purge,i} + n_{g,ad,i} + n_{s,ad,i} = n_{g,de,i} + n_{s,de,i} + n_{res,i} \quad \text{for i: } N_{i-1} \tag{3.7}$$

The equilibrium of the gas and adsorbent phase is described by the Langmuir equation (it is assumed that only $CO_2$ is adsorbed):

$$q_{CO_2} = \frac{b_{CO_2} \cdot q_{max,CO_2} \cdot p_{CO_2}}{1 + b_{CO_2} \cdot p_{CO_2}} \tag{3.8}$$

with $q_{CO_2}$ as the $CO_2$ loading of the adsorbent. The two parameters $b_{CO_2}$ and $q_{max,CO_2}$ represent the isothermal constants of the Langmuir model. Delgado et al. discussed adsorption materials for the separation of many gas mixtures and showed that BPL 4X10 activated carbon is attractive for $H_2/CO_2$ separation [Delg2014]. Thus, this material is used in this chapter. The two parameters $b_{CO_2}$ and $q_{max,CO_2}$ are 0.4 $bar^{-1}$ and 7.07 mol/kg, respectively. To account for non-ideal effects, such as limitations by kinetics, three fitting parameters ($\eta_V$, $\eta_{ad}$, $\eta_{ad}$) are incorporated in the PSA model. The fitting parameter $\eta_{ad}$ corrects the adsorber volume since the short-cut model tends to underestimate the actually required volume:

$$V_{Adsorber} = V \cdot \eta_V \tag{3.9}$$

with $V_{Adsorber}$ as the volume of the adsorption bed used (the total adsorber bed volume $V$ minus the unused adsorber bed) and the fitting variable $\eta_V$ as the ratio of the used volume of the adsorbent bed and the total volume within the short-cut-model. The fitting parameter $\eta_{ad}$ allows to estimate the gas phase composition at the end of the adsorption step:

$$y_{g,ad,i} = y_{feed,i} + (y_{prod,i} - y_{feed,i}) \cdot \eta_{ad} \tag{3.10}$$

with $y_{g,ad,i}$ as the molar fraction of component $i$ in the gas phase at the end of the adsorption step, $y_{feed,i}$ the molar feed fraction and $y_{prod,i}$ the molar product fraction. Thus, the average gas composition lies between the feed and product composition. Finally, the fitting parameter for the desorption

step $\eta_{de}$ describes the incomplete regeneration of the adsorbent bed:

$$y_{g,de,i} = y_{feed,i} + (y_{prod,i} - y_{feed,i}) \cdot \eta_{de} \tag{3.11}$$

with $y_{g,de,i}$ as the molar fraction of component $i$ in the gas phase at the end of the desorption step. The fitting parameters were obtained by simulating the PSA unit rigorously for a wide range of feed compositions (70, 80 and 90 mol-%) and adsorber volumes using Aspen Adsorption™. For all simulations, the product flow was fixed and the required feed adsorption pressure, the feed flow needed and the resulting product recovery were calculated. Based on the sensitivity study with the rigorous PSA model, a regression analysis was performed to determine the fitting parameters (see Table 3.1). The resulting fitting parameters are utilizable for a wide range of adsorption pressures and feed compositions. Figure 3.5 depicts the method for the development of the short-cut model.



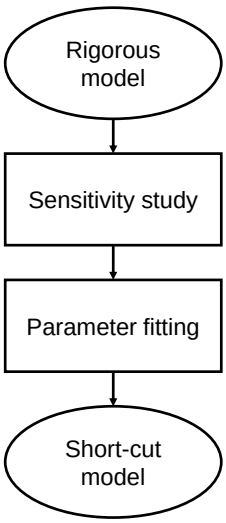


**Figure 3.5:** Method for developing the short-cut model.

Figure 3.6 (a) and (b) compare the adsorber volume per molar flow of product as well hydrogen recovery for the rigorous and the short-cut model for a feed fraction of 80%. The comparison underlines that the short-cut model with the fitting parameters can describe the adsorption process precisely.

**Table 3.1:** Fitting parameters for the PSA short-cut model.

| Fitting parameter | Value |
|---|---|
| $\eta_{ad}$ | 0.18 |
| $\eta_{de}$ | -2.12 |
| $\eta_V$ | 1.10 |

#### Compressor

For the hybrid separation process, compressors are used to generate the driving force for the membrane units and the adsorption pressure. To reduce the calculation effort, we assumed multi-stage compressors with inter-stage cooling for isothermal compression. Hence, the energy consumption of the compressors $P_{Com}$ is calculated by the following equation [Bieg1997]:

$$P_{Com} = \frac{1}{\eta_{Com}} \cdot \dot{n} \cdot R \cdot T \cdot ln(\frac{p_N}{p_0}) \tag{3.12}$$

where $\eta_{Com}$ is the overall efficiency of the compressor, $\dot{n}$ is the molar flow rate, $R$ the ideal gas constant, $T$ the temperature of the gas stream and $p_0$ as well as $p_N$ the inlet and outlet pressure of the compressor, respectively.

### 3.2.3 Economics

In this chapter, we systematically investigated the optimal design of hybrid membrane-PSA processes for $H_2$ purification. For these processes, it is challenging to balance the multiple trade-offs, e.g. plant size versus energy costs for compression. In principle, two different optima can be distinguished: (i) the economic and (ii) the energetic optimum. However, the economic optimum is of higher practical relevance as the energy demand can often be reduced by providing more membrane area and/or a higher adsorber volume. Since only the separation step of the biohydrogen production is considered, it is more appropriate to reduce the separation costs instead of maximizing the profit of the process. By taking the hydrogen

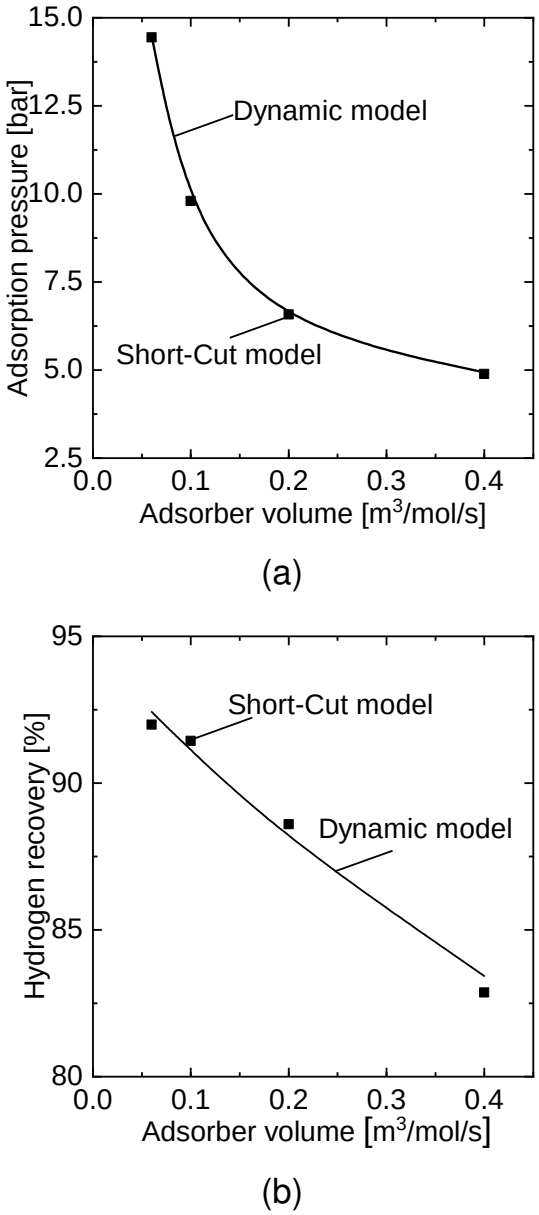


**Figure 3.6:** Comparison of the short-cut model and the rigorous Aspen Adsorption™ model for an adsorber feed composition of 80 mol-% $H_2$. (a) For different adsorber volumes, the required feed pressure to reach a $H_2$ product purity of 99 mol-% was calculated. The resulting $H_2$ recovery is shown in (b).

loss into account, the benefit of the process is indirectly optimized as well. Thus, we minimized the specific purification costs to balance the multiple trade-offs of the separation process, e.g. plant size versus energy costs for compression. Therefore, the investment costs, i.e. costs for membrane, adsorption bed and compressor, were annualized. The operation costs entail the energy costs for the compression, the membrane replacement, the ad-

sorbent replacement as well as opportunity costs for product losses in the waste streams. The equivalent annual costs $EAC$ are defined as follows:

$$EAC = C + \frac{I_{Tot}}{A_{t_{Plant},r}} \tag{3.13}$$

with $C$ as the annual operation costs, $I_{Tot}$ as the total investment costs, $t_{Plant}$ as the plant lifetime, $r$ as the interest rate and $A_{t_{Plant},r}$ as the annuity factor:

$$A_{t_{Plant},r} = \frac{1 - \frac{1}{(1+r)^{t_{Plant}}}}{r} \tag{3.14}$$



The specific costs $c_{Spec}$ are then calculated using the product mass stream $\dot{m}_{Prod}$ and the annual operation time $t_{Ope}$:

$$c_{Spec} = \frac{EAC}{\dot{m}_{Prod} \cdot t_{Ope}} \tag{3.15}$$

The total investment costs are given by:

$$I_{Tot} = I_{Com} + I_{Mem} + I_{PSA} \tag{3.16}$$

with $I_{Com}$, $I_{Mem}$ and $I_{PSA}$ as investment costs for the compressors, the membrane units and the PSA unit, respectively. For simplification, we assumed that the compressor investment cost scale linearly with the power duty:

$$I_{Com,i} = P_{Com,i} \cdot p_{Com} \tag{3.17}$$

Here, $p_{Com}$ represents the power specific investment price of the compressor. Equivalently, the investment cost for the membrane unit can be calculated as follows:

$$I_{Mem,i} = A_{Mem,tot} \cdot p_{Mem} \tag{3.18}$$

with $A_{Mem,tot}$ as the total membrane area to be installed and $p_{Mem}$ as the specific membrane price. In this chapter, the PSA unit process consists of

four pressure vessels operating in parallel, but with shifted cycle schedules. The investment costs of the PSA unit $I_{PSA}$ are calculated by adding the costs for the pressure vessels $I_{Vessel}$ and the cost of the adsorption material $I_{Adorbent}$:

$$I_{PSA} = (I_{Vessel} + I_{Adsorbent}) \cdot n_{PSA} \tag{3.19}$$

with $n_{PSA}$ as the number of adsorber beds. The costs for the pressure vessels are calculated by the Guthrie method [Bieg1997]:



$$I_{Vessel} = UF \cdot BC \cdot (MPF + MF - 1) \cdot CF \tag{3.20}$$

with $UF$ as the update factor, $BC$ the base costs, $MPF$ as the material pressure correction and $MF$ as the module factor and $CF$ as the cost factor to account for the valves in connections of the PSA unit. The base costs are calculated as follows:

$$BC = C_0 \cdot (\frac{L}{L_0})^w \cdot (\frac{D}{D_0})^e \tag{3.21}$$

Here $C_0$, $L_0$ and $D_0$ are the base costs as well as the reference length and diameter according to the Guthrie method [Bieg1997]. $w$ and $e$ denote the length and diameter exponent, respectively. The investment costs of the adsorbent material are calculated as follows:

$$I_{Adsorbent} = V_{Adsorber} \cdot (1 - \epsilon_{Bed}) \cdot \rho_{Sorbent} \cdot C_{Ads} \tag{3.22}$$

with $V_{Adsorber}$ as the volume of the adsorption columns, $\epsilon_{Bed}$ as the bed porosity and $\rho_{Sorbent}$ as the adsorbent density. The sum of the energy costs for compression $C_{Com}$, the membrane replacement costs $C_{Mem}$, the adsorbent service costs $C_{PSA}$ as well as lost revenues due to incomplete recovery $C_{H_2,loss}$ determines the operating costs:

$$C = C_{Com} + C_{Mem} + C_{PSA} + C_{H_2,loss} \tag{3.23}$$

The energy costs are the product of the compressor power $P_{Com}$ and electricity price $p_{Energy}$:

$$C_{Com} = P_{Com} \cdot p_{Energy} \tag{3.24}$$

For simplification, the membrane replacement costs are calculated by multiplying the membrane investment cost $I_{Mem}$ by the ratio of the plant lifetime $t_{Plant}$ and the lifetime of the membrane $t_{Mem}$:

$$C_{Com} = I_{Mem} \cdot \frac{t_{Plant}}{t_{Mem}} \tag{3.25}$$



Equivalently, the costs for the adsorbent replacement is calculated as follows:

$$C_{PSA} = I_{Adsorbent} \cdot \frac{t_{Plant}}{t_{Ads}} \tag{3.26}$$

with $t_{Ads}$ as the lifetime of the sorbent. The costs due to product losses per year are calculated as follows:

$$C_{H_2,loss} = \dot{m}_{Feed} \cdot p_{H_2} \cdot (1 - \tau) \cdot t_{Ope} \tag{3.27}$$

with $\dot{m}_{Feed}$, $p_{H_2}$ as the price of hydrogen and the recovery $\tau$.

### 3.2.4 Mathematical problem definition

As mentioned before, identifying the optimal process design was formulated as an optimization problem using MINLP:

$$min\, f(x, y) \tag{3.28}$$

subject to:

$$h(x, y) = 0 \tag{3.29}$$

$$g(x, y) \geq 0 \tag{3.30}$$

$$x \in X \tag{3.31}$$

$$y \in \{0; 1\} \tag{3.32}$$

where $f(x, y)$ is the objective function, i.e. the specific operation costs, $h(x, y)$ are the model equations presented above such as the equations describing the adsorber and membrane units, $g(x, y)$ is the set of constraints that define the feasible space of operation such as the pressure range or product purity. $x$ is the vector of the optimization variables, e.g. the system pressure, the membrane area for each stage or the adsorber volume, and $y$ the vector of integer variables which describe the connections between the operation units. We implemented the optimization model including the models for the unit operations as well as the processes interconnections in the General Algebraic Modeling System (GAMS). The Antigone solver (Algorithms for coNTinuous / Integer Global Optimization of Nonlinear Equations) was used for global optimization.

## 3.3 Case study

Various feedstocks and production paths can be used for biogenic hydrogen production [Bhar2016; Kapd2006]. Thus, the gas composition can vary significantly. Furthermore, the $H_2$ yield of the fermentation process can be increased by nitrogen purging because a high $H_2$ partial pressure inhibits the biohydrogen production. However, nitrogen sparging increases the costs and the difficulty to purify $H_2$. Thus, we consider a process without nitrogen sparging in this chapter. Besides $H_2$ and $CO_2$, biohydrogen streams also contain smaller amounts of $H_2S$, $CH_4$, CO, $N_2$ and water [Shal2015]. $H_2S$ and water permeate faster through the membrane than $H_2$ and thus concentrate in the $CO_2$ waste stream [Lin2015]. Depending on

further utilization of the $CO_2$ stream, subsequent removal of $H_2S$ and water might be necessary [Lin2015]. Alternatively, a dehumidifier can reduce the water content of the feed stream. Furthermore, $CH_4$, CO and $N_2$ more favorable adsorb on activated carbon [Lope2009], which allows to reach the targeted product purity. Thus, we only consider a binary gas mixture for simplification. In subsequent studies, the model can be easily extended to account for additional components. However, an increased computational effort for global optimization has to be taken into account. To represent different biohydrogen feedstocks, we considered a wide range of $H_2$ feed fractions (25%, 50% and 75%).



Depending on the utilization, different hydrogen purities are required. For example, heat treatment of metals, power generator cooling and hydrogen distribution systems require low grade hydrogen [Levi2010; Liao2010]. Thus, in this chapter, we target a product purity of 99% [Liao2010]. This presents a product purity which can be reached by both membrane and PSA processes and is thus particular interesting as sophisticated process design methods are necessary for an efficient process design. We used 150 $Nm^3/h$ as the feed stream volume, representing a feasible size of biogenic gas production processes [Scho2013a]. To investigate the influence of the system pressure on the process design and the operation costs, we conducted a sensitivity study for different pressure levels, i.e. that for each pressure (depending on the feed concentration between 2 and 16 bar) the optimal process design as well as the related costs were identified. For each configuration, the desorption takes place at 1 bar. All important process parameters are summarized in Table 3.2.

The main economic parameters used in this chapter are summarized in Table 3.3. A membrane price of 55 €/$m^2$ and a lifetime of four years were assumed. For the adsorbent materials, life times of more than ten years have been reported [Wies1988]. However, minor impurities might be present in the feed stream and reduce the sorbent's life time. Thus, a life time of four years, as a conservative estimation, was assumed as well. The price of the sorbent material is 3 €/kg. The costs for the pressure vessels in the adsorption unit were calculated using Guthrie's cost method [Bieg1997;

**Table 3.2:** Process parameters for biohydrogen upgrading.

| Parameter | Description | Value | Unit |
|---|---|---|---|
| $p_{Des}$ | Desorption pressure | 1 | bar |
| $p_{Feed}$ | Process feed gas pressure | 1 | bar |
| $Q_{CO_2}$ | $CO_2$ permeance of the membrane | 1000 | GPU |
| $Q_{H_2}$ | $H_2$ permeance of the membrane | 85 | GPU |
| $T_{Feed}$ | Process feed gas temperature | 293.15 | K |
| $V_{Feed}$ | Feed rate | 150 | $Nm^3/h$ |
| $y_{Feed}$ | $H_2$ feed fraction | 25/50/75 | mol-% |
| $y_{Product}$ | Purity | 99 | mol-% |
| $\eta_{Com}$ | Overall compressor efficiency | 0.72 | - |
| $\rho_{Sorbent}$ | Density of sorbent particle | 916 | $kg/m^3$ |
| $\epsilon_{Sorbent}$ | Adsorption bed porosity | 0.5 | $kg/m^3$ |

Guth1969]. Additionally, a cost factor $CF$ of three has been applied to account for the valves and piping between the pressure vessels. The cost factor is based on the mutual communication with a manufacturer of PSA plants. The investment costs for the compressor were considered with 6.5 k€/kW. Besides the investment and operation expenditures, the costs for the incomplete recovery and thus hydrogen loss must be taken into account to optimize the benefit of the process. Unfortunately, only little information of the hydrogen price in dependence of the hydrogen purity can be found in the literature. The market prices depend on the costs of the production route and feedstocks, which vary both with location and time. For example, the U.S. Department of Energy targets hydrogen production costs for 2020 of 8.1 €/kg for photobiological biohydrogen production [US D2015]. In this chapter, we assumed a $H_2$ price of 5 €/kg, which is a conservative assumption for the hydrogen price from biological origin. Even if this causes some uncertainty, we think that identifying the economic optimum is of higher practical relevance as the energy demand, which is used in most optimization studies, can often be reduced by providing more membrane

area and/or adsorber size. The electricity price is 0.08 €/kWh and the plant operates 8000 h/a. A plant lifetime of 15 years and an interest rate $r$ of 9% was assumed. For the optimal process design, the trade-offs between investment costs and operation costs, e.g. energy consumption and product recovery, must be balanced. Although the ecomomic parameters may vary with time and location, which influences the optimal solution of the mathematical problem, we think that the costs are a reasonable objective function as it comprises the most important criteria of the integrated process.

**Table 3.3:** Economic parameters for the cost calculation.

| Parameter | Description | Value | Unit |
|---|---|---|---|
| $C_0$ | Vessel base costs | 1 | k€ |
| $CF$ | Cost factor to account for valves | 3 | - |
| $D_0$ | Vessel reference diameter | 0.91 | m |
| $e$ | Vessel diameter exponent | 1.05 | - |
| $r$ | Interest rate | 9 | % |
| $L_0$ | Vessel reference length | 1.22 | m |
| $MF$ | Vessel module factor | 4.23 | - |
| $MPF$ | Vessel pressure and materials correction factor | 1.45 | - |
| $p_{Com}$ | Compressor investment price | 6.5 | k€/kW |
| $p_{Energy}$ | Electricity price | 0.08 | €/kWh |
| $p_{H_2}$ | $H_2$ price | 5 | €/kg |
| $p_{Mem}$ | Membrane price | 55 | €/m$^2$ |
| $p_{Sorbent}$ | Adsorber material costs | 3 | €/kg |
| $t_{Mem}$ | Membrane lifetime | 4 | a |
| $t_{Ope}$ | Annual operation time | 8000 | h/a |
| $t_{Plant}$ | Plant lifetime | 15 | a |
| $t_{Sorbent}$ | Adsorber material lifetime | 4 | a |
| $UF$ | Update factor (1968/2016) | 4.9 | - |
| $w$ | Vessel length exponent | 0.81 | - |

## 3.4 Results and discussion

Using MINLP, we optimized the hybrid membrane-PSA processes. Therefore, we systematically varied the system pressure level and optimized the process configuration and parameters, such as membrane area and adsorbent bed size. A single system pressure was set by the boundary condition of the process model as it allows recycling the process streams without

any further compression, which would require an additional compressor and thus increase the costs. Furthermore, it guarantees that any reduction of the pressure of single streams is necessary, which would result in the loss of mechanical energy, respectively. Feed conditions of the separation process can vary significantly with feedstock and operating conditions of the biohydrogen production process. To provide optimal designs for a wide range of potential feed compositions, we optimized the hybrid membrane-PSA systems for $H_2$ feed fractions of 25, 50 and 75 mol-%.

### 3.4.1 Process optimization for a $H_2$ feed fraction of 75 mol-%



The specific separation costs for different system pressures are presented in Figure 3.7 (a). The lowest costs of 0.60 €/kg are obtained at a system pressure of 9.8 bar. The resulting $H_2$ recovery at this pressure is 98.3%. The optimal process consists of three membrane stages and a PSA unit for the final purification (see Figure 3.7 (b)). In the first membrane unit, the hydrogen is concentrated in the retentate stream and then fed to the PSA unit. The permeate of the first membrane unit is pressurized before entering a second membrane for enhanced recovery. The tail gas of the PSA unit is repressurized as well and fed to a third membrane unit, which retentate stream is recycled to the first membrane unit. A process with a system pressure of 6 bar and 16 bar results in almost 10% and 5% higher costs, respectively. For commodity products, such as hydrogen, this can be a significant cost difference having a significant economic impact on manufacturers. While the costs increase, it still might be beneficial to use and operate at higher pressures depending on the downstream utilization of the purified $H_2$.

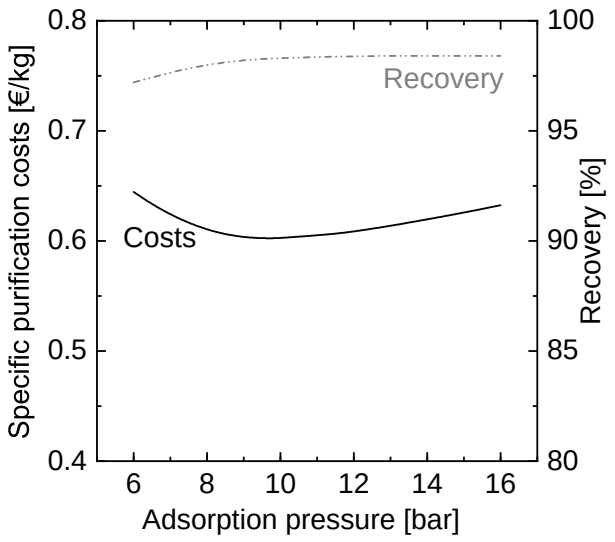


(a)

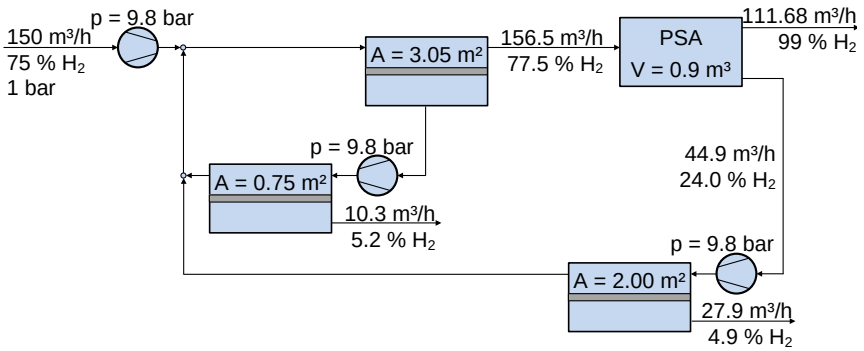


(b)

**Figure 3.7:** (a) Minimal specific purification costs of the hybrid membrane PSA process for a $H_2$ feed fraction of 75 mol-% at different system pressures. For each pressure, the optimal process was identified. (b) Optimal process design for a $H_2$ feed fraction of 75 mol-%. The volume of the adsorber column represents the volume for one of the four columns.

### 3.4.2 Process optimization for a $H_2$ feed fraction of 50 mol-%

For a hydrogen feed fraction of 50 mol-%, a system pressure of 7.7 bar resulted in the lowest costs of 1.02 €/kg (see Figure 3.8 (a)). compared with a feed fraction of 75 mol-%, the dependency on the system pressure is more pronounced. In comparison to a feed content of 75%, the recovery is slightly lower (94.9% for 4 bar and 97.1% for 14 bar). For the feed stream

with a $H_2$ feed fraction of 50 mol-%, Figure 3.8 (b) depicts the optimal process design. As for the feed fraction of 75%, a three-stage membrane process is optimal. compared with the process at a feed content of 75 mol-%, the $H_2$ feed fractions of the PSA (83.7 mol-%) and its tail gas are higher (29.3 mol-%). At pressures below 6 bar, the optimization methods identifies processes without a PSA unit. At these operation points, the partial pressure difference of the $CO_2$ during adsorption and desorption is very low. Thus, the processes cannot benefit from a high working capacity of the sorbent. This results in a second local minimum for the costs at around 4.6 bar. Also the shift from hybrid to pure membrane processes results in a sharp decrease of the recovery. This shows the advantage of deterministic global optimization, as one is not trapped in suboptimal solutions.



### 3.4.3 Process optimization for a $H_2$ feed fraction of 25 mol-%

Finally, we also optimized the hybrid membrane-PSA process for a $H_2$ feed fraction of 25 mol-%. Figure 3.9 (a) shows the optimal separation costs for the purification of a feed stream containing 25 mol-% at different system pressures. As for a feed fraction of 50%, stand-alone membrane processes were identified at pressures below 6 bar. The optimal system pressure is 3.5 bar at minimal specific purification costs of 1.86 €/kg. For higher system pressures, the costs increase up to 2.16 €/kg for 12 bar. At even higher system pressures, the specific costs further increase. The $H_2$ recovery ranges between 91.5% for a system pressure of 3 bar and 95.5% for 12 bar. Figure 3.9 (b) shows the optimal design for the separation process for a system pressure of 3.5 bar. The final hydrogen purity of 99% is reached in the retentate of the first membrane unit. A second membrane unit is then used to recover the permeate of the first unit.

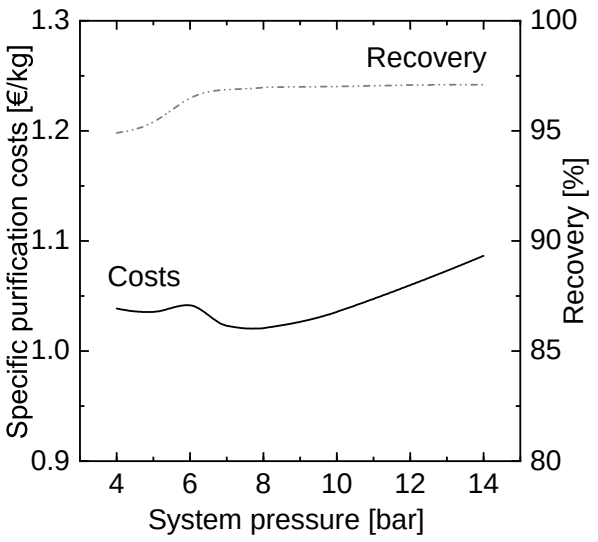


(a)

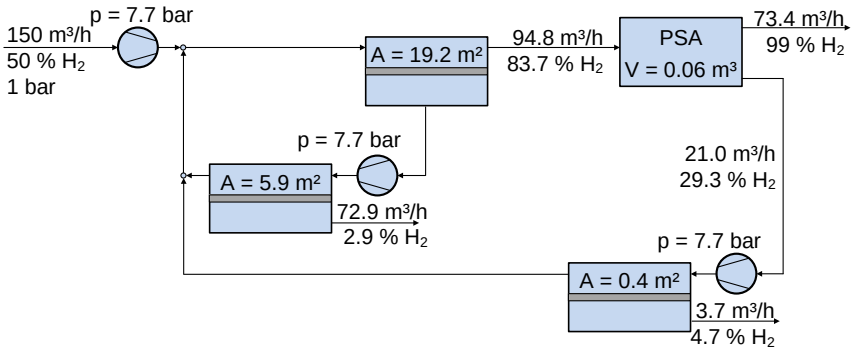


(b)

**Figure 3.8:** (a) Minimal specific purification costs of the hybrid membrane PSA process for a $H_2$ feed fraction of 50 mol-% at different system pressures. For each pressure, the optimal process was identified. (b) Optimal process design for a $H_2$ feed fraction of 50 mol-%. The volume of the adsorber column represents the volume for one of the four columns.

### 3.4.4 Comparison of different feed fractions

Figure 3.10 compares the minimal specific purification costs as well as the energetic efficiency $\eta$ for the three feed compositions. The energetic efficiency relates the energy consumed for the purification process and the energy contained in the hydrogen product stream. It is defined as follows:

$$\eta = 1 - \frac{P_{Com,total}}{LHV_{H_2} \cdot \dot{n}_{Product}} \tag{3.33}$$

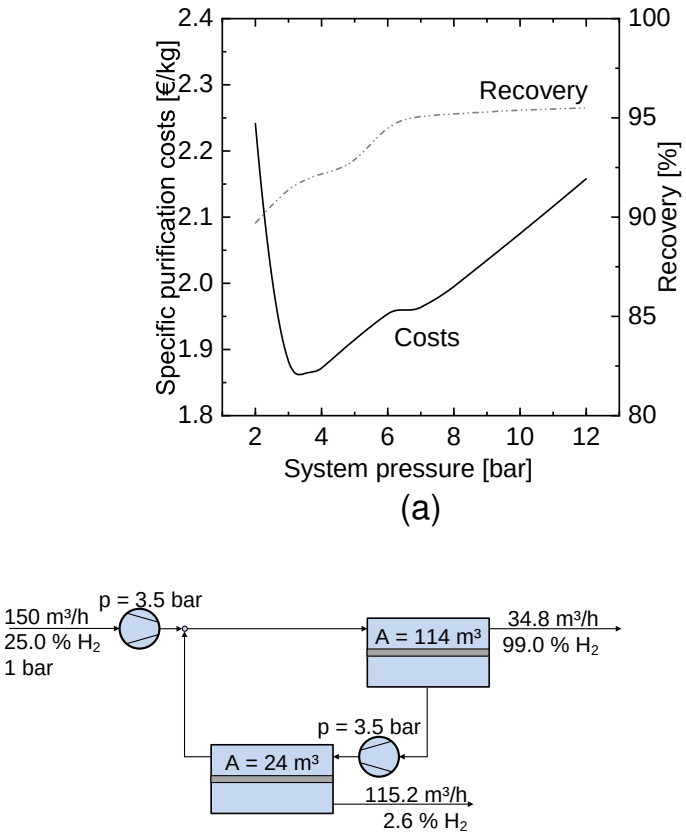


**Figure 3.9:** (a) Minimal specific purification costs of the hybrid membrane PSA process for a $H_2$ feed fraction of 25 mol-% at different system pressures. For each pressure, the optimal process was identified. (b) Optimal process design for a $H_2$ feed fraction of 25 mol-%.

with $P_{Com,total}$ as the compression duty, $LHV_{H_2}$ as the lower heating value of $H_2$ and $\dot{n}_{Product}$ as the product flow rate. The energy efficiencies of the optimal processes are 77.9% for a $H_2$ feed fraction of 25 mol-%, 88.6% for a $H_2$ feed fraction of 50 mol-% and 93.8% for a $H_2$ feed fraction of 75 mol-%. Since the specific purification costs for a hydrogen feed fraction of 25 mol-% (1.86 €/kg) are about three times higher than the costs for a hydrogen feed fraction of 75 mol-% (0.6 €/kg), it is crucial to develop biohydrogen production paths which allow high hydrogen gas phase concentrations.

While the conclusions drawn are specific for the process conditions simulated, some general conclusions for hybrid membrane-PSA processes can

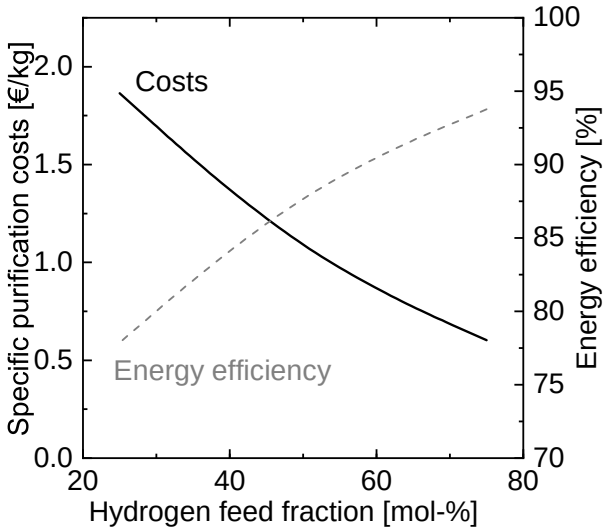


**Figure 3.10:** Comparison of the costs and energy efficiency for different hydrogen feed fractions.

be derived nonetheless:

- At low hydrogen feed fractions, low(er) system pressures are more beneficial since it is very energy consuming to compress the entire bulk feed stream to high pressures.
- At low system pressures, the required size for the membrane (and PSA) units increases and the recovery decreases sharply (compare Figure 3.6). Thus, a high degree of pre-purification is more beneficial.
- If a PSA unit is used, recycling of the tail gas is beneficial to increase the recovery.

The presented optimization methodology for hybrid membrane-PSA systems can be used to evaluate many different process configurations for the many different separation tasks in microbial biohydrogen enrichment [Arya2018]. Each case needs to be considered separately depending on the upstream and downstream conditions. Here, only binary gas mixtures are addressed. It will be even more intricate when ternary gas mixtures need to be separated.

## 3.5 Conclusion

This chapter presented a tool for biohydrogen purification, which allows identifying optimal hybrid membrane-PSA processes, i.e. designs which resulted in the lowest costs. The tool is based on a process model implemented in GAMS and solved by MINLP. The process model includes models for the process units, the process structure as well as economic equations.

The $H_2$ feed fraction can vary significantly depending on the fermentation conditions and the used feedstock. Thus, we optimized the integrated membrane-PSA process for a wide range of hydrogen feed fractions (25 mol-%, 50 mol-% and 75 mol-%). For all feed compositions, a bulk separation using membrane processes was identified as the optimal process design. For $H_2$ feed fractions of 50 mol-% and 75 mol-%, a three-stage process with a PSA unit was optimal. The resulting costs were 1.02 €/kg for $H_2$ feed fraction of 50% and 0.60 €/kg for $H_2$ feed fraction of 75 mol-%. Interestingly, at a hydrogen feed fractions of 25%, the optimal system pressure is only 3.5 bar. At low system pressures, the partial pressure difference for $CO_2$ during ad- and desorption is only minor and the process cannot benefit from a high working capacity. Thus, a stand-alone membrane process was identified. These results provide a sound indication of the optimal design of hybrid biohydrogen separation processes depending on the feed composition and already indicate that is of utmost importance to develop biohydrogen production routes with high hydrogen gas stream fractions to make the separation economically feasible.

3

# 4 Optimized hollow fiber adsorbents and pressure swing adsorption process for $H_2$ recovery



Parts of this chapter have been published as:

Burkhard Ohs, Johannes Lohaus, Dennis Marten, Ralf Hannemann-Tamás, Alexandra Krieger, Matthias Wessling
*Optimized hollow fiber sorbents and pressure swing adsorption process for $H_2$ recovery*, Industrial & Engineering Chemistry Research, 2018
DOI: 10.1021/acs.iecr.7b05368

# 4.1 Introduction

Besides optimizing hybrid-pressure swing adsorption processes, adsorption processes can further be improved by using hollow fiber sorbents. As discussed in Chapter 2, hollow fiber sorbents benefit from a low pressure loss and a reduced mass transfer resistance, well-defined flow conditions and the possibility of thermal moderation. The design of hollow fiber sorbent itself provides additional degrees of freedom for process development. To exploit their potential fully, process and fiber design must be well balanced. Thus, an integrated optimization framework is developed and applied for $H_2$ upgrading with hollow fiber made of a hybrid polymer-zeolite matrix. The matrix is coated with an impermeable polyvinylidene chloride (PVDC) layer to separate the gas phase and the thermal moderator (see Figure 2.1) [Live2012b]. In contrast to previous works, this chapter combines the different dimensions of PSA research by optimizing the process and fiber design simultaneously. In particular, this chapter analyzes the optimal design of hollow fiber sorbents such as fiber diameter, fiber length and fiber wall thickness and how this parameter vary for different process boundary conditions.



# 4.2 Modelling and optimization

## 4.2.1 Variable space for optimization

A variety of process and hollow fiber variables influence the performance of the PSA process. But, contemporary optimization methods have not been applied to a PSA process using hollow fiber sorbents. The interplay between process and fiber design is still unknown and studies usually focus on either of these two dimensions. Determan et al. have shown that a trade-off between fiber dimension as well as module sorption capacity exists [Dete2012]. Additionally, thin fiber geometries reduce the mass transfer resistance but increases pressure loss [Bess2010; Reza2010a]. Also, long

fibers allow for longer adsorption times but increase pressure loss, which decreases adsorption equilibrium and thus module capacity [Chah2001]. Furthermore, Ko et al. observed that product purity increases but recovery decreases with bed length for conventional PSA processes [Ko2003]. Finally, multiple-beds can be interconnected with complex process cycles[Bieg2005]. Thus, the following variables can be optimized for hollow fiber sorbent based PSA processes:

- geometrical quantities:
  - inner and outer diameter of the hollow fibers,
  - length of the hollow fibers,
- process quantities:
  - adsorption pressure,
  - molar flow rate of the feed per hollow fiber (i.e. number of hollow fibers),
  - molar flow rate of the purge stream per hollow fiber,
- process schedule:
  - duration of the adsorption and desorption step,
  - duration of the pressurization and depressurization step,
- multiple-bed process schedule:
  - bed interconnections and
  - equalization steps.

Between these variables, many trade-offs exist, which can only be solved by sophisticated process design methods. Also, it has not been investigated yet, if the optimal fiber geometries vary with product requirements or adsorption capacity. Thus, we propose an optimization model for hollow fiber sorbents, which also allows conducting a techno-economic evaluation of new adsorbent designs. The optimization model comprises (i) a detailed physical model of a PSA process based on hollow fiber sorbents

as well as (ii) economic correlations to describe the overall costs for the process. The objective of the optimization study is the reduction of the separation costs. Mixed-integer-nonlinear-programming (MINLP) is then used to solve the optimization problem and determine (i) optimized geometrical properties of the hollow fiber and (ii) optimal operating conditions such as adsorption pressure, module size and cycle time. As a case study, we considered the separation of $H_2$ and $CO_2$ as an important separation task in both traditional chemical industry as well as emerging applications such as biohydrogen upgrading.

### 4.2.2 Process description



In this chapter, we model PSA processes for the purification of $H_2$ from $CO_2$ using hollow fiber sorbents. The hollow fiber consists of a hybrid polymer-zeolite matrix, which is coated with an impermeable polyvinylidene chloride (PVDC) layer on the shell side (see Figure 2.1) [Live2012b]. The fibers were produced by via dry-jet, wet-quench spinning with commercially available materials [Live2012b]. An additional wax layer in the interspace of the fibers allows the thermal moderation of the adsorption process. Using lumen side hollow fiber sorbents reduces channeling and dispersion within the fiber module as the flow distribution is equal for each fiber. This increases breakthrough time and thus the volume specific efficiency of the fiber. Furthermore, the thermal moderator can be more easily introduced on the shell side compared with the lumen side, where the wax must be introduced into every single fiber.

The adsorption process comprises a four-step cycle: pressurization, adsorption, depressurization and desorption (see Figure 4.1). The hollow fiber adsorption module is first pressurized by purified $H_2$. Subsequently, the pressurized raw gas mixture is fed to the module, where the $CO_2$ is adsorbed on both the zeolite and the polymer binder. Thus, $H_2$ is obtained as the product. Before the $CO_2$ breakthrough, the adsorption step is terminated and followed by depressurization of the adsorber module. Finally, the hollow fiber is regenerated, which is assisted by $H_2$ purging. Additional

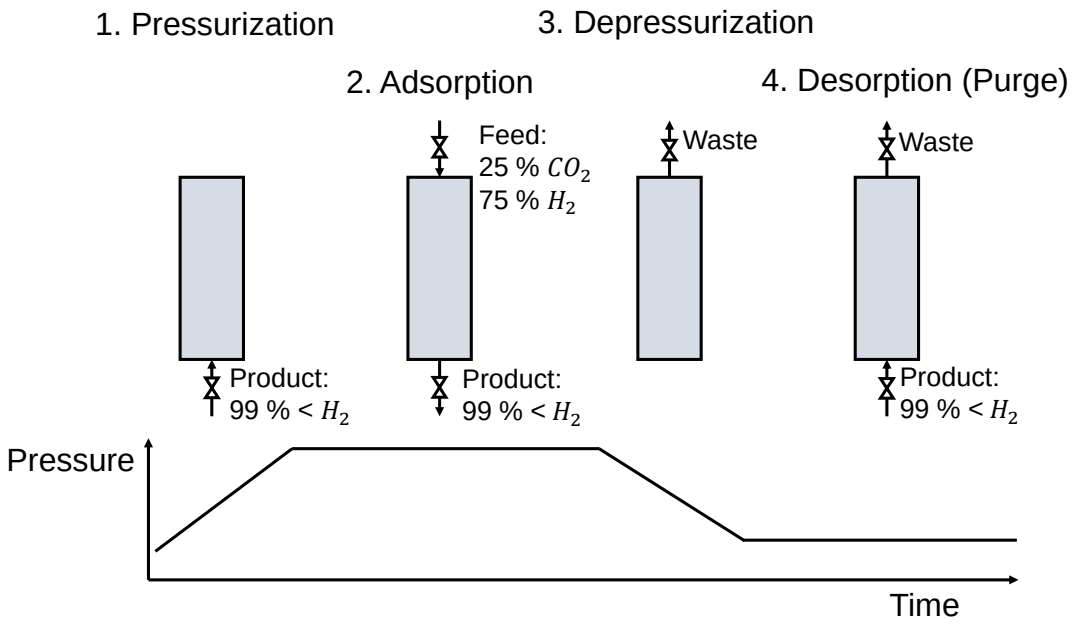


**Figure 4.1:** PSA four-step cycle for the separation of $H_2$ and $CO_2$ with hollow fiber sorbents



purging reduces the partial pressure of the $CO_2$ and increases the regeneration but also decreases the recovery of the process. Thus, there is a trade-off between adsorbent size, cycle time and recovery.

The four-step adsorption process is modeled dynamically. However, the following assumptions and simplifications are applied:

- the gas phase follows the ideal gas law,
- only $H_2$ and $CO_2$ are present in the gas stream,
- the radial variation of state variables is neglected,
- the adsorption rate is approximated by a linear driving force (LDF) expression,
- the viscous flow through the pores of the hollow fiber adsorbent is neglected,
- the temperatures of the fiber adsorbent wall, the impermeable, layer and the paraffin wax are identical,
- the adsorption capacity of the impermeable layer is negligibly small,

- the temperature and pressure depending changes of the bed void volume is negligible,
- the axial fluxes due to diffusion in the fiber wall are negligible,
- the hollow fiber module is adiabatic,
- the $H_2$ sorption is negligible,
- the phase change of the thermal moderator, i.e. wax, is not kinetically hindered.

### 4.2.3 Hollow fiber sorbent model



#### Mass balance

Lively et al. [Live2012b] presented a simplified model for PSA processes based on hollow fiber sorbent but assumed constant lumen gas velocity. However, this assumption is only valid for trace recovery from bulk streams. If a major component is removed, the corresponding velocity change of the bulk needs to be incorporated. Thus, we extended the model reportet in the literature for adsorptive bulk separation in this chapter. The molar balance of $CO_2$ for the hollow fiber sorbent is then given by:

$$\epsilon \frac{\partial(v_z\, c_{CO_2})}{\partial z} + \left(\frac{1-\epsilon_{fb}}{\epsilon_{fb}}\,\epsilon + 1\right) \frac{\partial c_{\mathrm{CO_2}}}{\partial t} + \left(\frac{1-\epsilon_{fb}}{\epsilon_{fb}}\right) \frac{\partial q_{CO_2}}{\partial t} - D_L \frac{\partial^2 c_{CO_2}}{\partial z^2} = 0 \tag{4.1}$$

Here, the time $t$ and the axial direction $z$ are the independent variables. The convective flow corresponds to the change of the net gas flow through the hollow fiber lumen in axial direction $z$. $v_z$ is the axial velocity and $c_{\mathrm{CO_2}}$ the $CO_2$-concentration. The time-dependent change of the concentration ($\partial c_{\mathrm{CO_2}}/\partial t$) in the gas phase at a specific axial position is considered in the second term, where $\epsilon_{fb}$ and $\epsilon$ symbolize the volumetric ratio between the fiber and the bore volume as well as the porosity of the fiber itself (see

[Ohs2018b] for numerical values of the process parameters). The porosity of the fiber is defined as follows:

$$\epsilon = 1 - \frac{V_{Zeo} + V_{CA}}{V_{HF}} \qquad with \quad V_{HF} = \frac{\pi}{4}\left(d_{fo}^2 - d_{fi}^2\right) L \quad , \tag{4.2}$$

where $V_{Zeo}$,$V_{CA}$ and $V_{HF}$ represent the volume of the zeolites, cellulose acetate and the hollow fiber sorbent, respectively. $d_{fo}$ and $d_{fi}$ stand for the outer and inner diameter.

The time derivative of the adsorbent loading $\partial q_{CO_2}/\partial t$ is described by the third term. The last term describes the axial dispersion due to concentration gradients. $D_L$ represents the axial dispersion coefficient. Analogously, the total mole balance is given by:

$$\begin{aligned} &\epsilon \, \frac{\partial(v_z \; c_{total})}{\partial z} + \left(\frac{1-\epsilon_{fb}}{\epsilon_{fb}} \, \epsilon + 1\right) \, \frac{\partial(v_z \; c_{total})}{\partial t} \\ &+ \left(\frac{1-\epsilon_{fb}}{\epsilon_{fb}}\right) \, \frac{\partial q_{\mathrm{CO_2}}}{\partial t} = 0 \end{aligned} \tag{4.3}$$

with $c_{total}$ as the total gas concentration. In this chapter, it is assumed that the hollow fiber sorbent only adsorbs $CO_2$.

### Energy balance

The energy balance for an infinitesimal element of the hollow fiber bore volume comprises five terms:

$$\frac{\partial H_{in}}{\partial t} - \frac{\partial H_{out}}{\partial t} = \frac{\partial H_g}{\partial t} + \frac{\partial H_{transfer}}{\partial t} + \frac{\partial Q_{TF}}{\partial t} \tag{4.4}$$

The two terms on the left-hand side $\partial H_{in}/\partial t$ and $\partial H_{out}/\partial t$ describe the convective enthalpy flow in and out of the infinitesimal element. The term $\partial H_g/\partial t$ stands for the accumulative enthalpy term and $\partial H_{transfer}/\partial t$ for the enthalpy exchange between the gas phase and the fiber materials due to ad- and desorption. The last term $\partial Q_{TF}/\partial t$ represents the heat exchange between the gas phase in the bore volume and the fiber wall. For an ideal gas behavior and constant heat capacity $c_p$, the difference in convective

enthalpy flow into and out of the bore volume can be written as follows:

$$\frac{\partial H_{in}}{\partial t} - \frac{\partial H_{out}}{\partial t} = \frac{A_{HF}}{R}\frac{d}{dz}(\frac{v_z\ p\ (\sum_{i=1}^{N} y_i\ (c_{p,i}\ (T_g - T_0) + h_0, i))}{T_g})dz \tag{4.5}$$

Here, $A_{HF}$, $R$, $p$ and $T_g$ define the cross-sectional area of the bore volume, the ideal gas constant, the velocity, the pressure and the gas temperature, respectively. $y_i$ and $c_{p,i}$ symbolize the molar fraction and the heat capacity of a specific component $i$. $T$ and $H$ are the temperature and the enthalpy, respectively, with $h_{0,i}$ as reference enthalpy for component $i$ at the reference temperature $T_0$.

The time derivative of the gas enthalpy $\partial H_g/\partial t$ in an infinitesimal element of the length $dz$ is given by:

$$\frac{\partial H_g}{\partial t} = \frac{d}{dt}\left(\sum_{i=1}^{N} n_{g,i}\ c_{p,i}\ T_g\right) \tag{4.6}$$

Here, $n_{g,i}$ represents the amount of a substance $i$ in an infinitesimal element of the fiber bore volume:

$$n_{g,i} = \frac{dz\ A_{HF}\ p\ y_i}{R\ T_g} \tag{4.7}$$

The enthalpy exchange $\partial H_{transfer}/\partial t$ between the gas phase and the fiber based on mass transfer is the sum of (i) the enthalpy flow into or out of the pores of the fiber due to pressure changes $\partial H_{Pore,flow}/\partial t$ and (ii) the enthalpy exchange due to adsorption $\partial H_q/\partial t$:

$$\frac{\partial H_{transfer}}{\partial t} = \frac{\partial H_{Pore,flow}}{\partial t} + \frac{\partial H_q}{\partial t} \tag{4.8}$$

with

$$\frac{H_{Pore,flow}}{\partial t} = \epsilon\ A_F\ dz\frac{d}{dt}\left(\frac{p}{R\ T_F}\right)\ \sum_{i=1}^{N}(c_{p,i}\ y_i)\ (T_g - T_F) \tag{4.9}$$

and

$$\frac{\partial H_q}{\partial t} = A_F \; dz \; \frac{\partial q}{\partial t} \; c_{p,CO_2} \; (T_g - T_F) \tag{4.10}$$

Here, $T_F$ and $A_F$ the temperature and the cross-sectional area of the hollow fiber wall. Values for the physical parameters, such as the porosity are based on experimental studies and are summarized in [Ohs2018b]. The heat exchange $\partial Q_{TF}/\partial t$ between the gas phase in the bore volume and the fiber is calculated by:

$$\frac{\partial Q_{TF}}{\partial} = d_{FI} \; \pi \; \alpha \; (T_g - T_F) \; dz \tag{4.11}$$

$d_{FI}$ symbolized the diameter of the bore volume (see Figure 4.2). The heat transfer coefficient $\alpha$ is calculated using the Nusselt number $Nu$:

$$Nu = \frac{\alpha \; d_{FI}}{\lambda_g} \tag{4.12}$$

$\lambda_g$ represents the thermal conductivity of the gas stream. The Nusselt number $Nu$ is constant for laminar flows. Additionally, the second energy balance describes the temperature changes of the solid fiber wall as well as the gas contained in its porous network. The temperature of the solid fiber and the gas in the porous structure are assumed to be equal. Thus, the energy balance results in:

$$0 = \frac{\partial H_F}{\partial t} + \frac{\partial H_P}{\partial t} - \frac{\partial Q_{WF}}{\partial t} - \frac{\partial Q_{TF}}{\partial t} - \frac{\partial H_{transfer}}{\partial t} + \frac{\partial H_{ad}}{\partial t} \tag{4.13}$$

$\partial H_F/\partial t$ and $\partial H_P/\partial t$ describe the time derivative of the enthalpy of the fiber and the pore system. $\partial Q_{WF}/\partial t$ is defined as the heat exchanged between the fiber and the wax. As mentioned before, $\partial H_{transfer}/\partial t$ and $\partial Q_{TF}/\partial t$ (see equations (4.8) and (4.11)) symbolize the enthalpy exchange due to mass and heat transfer with the gas phase flowing through the fiber lumen. $\partial H_{ad}/\partial t$ stands for the heat of adsorption and desorption. The time

derivative of the fibers enthalpy $\partial H_F/\partial t$ can be written as follows:

$$\frac{\partial H_F}{\partial t} = c_{p,fiber}\ A_F\ (1-\epsilon)\ \frac{\partial T_F}{\partial t}\ dz \tag{4.14}$$

$c_{p,fiber}$, $A_F$ and $\partial T_F/\partial$ are the heat capacity, the cross-sectional area and the temperature changes of the fiber. Equivalently, the following expression describes the time derivative of the enthalpy in the pore system $\partial H_P/\partial t$:

$$\frac{\partial H_P}{\partial t} = \frac{d}{dt}\left(n_{Pore}\ \sum_{i=1}^{N}(y_i\ c_{p,i}\ (T_F - T_0) + h_0)\right) \tag{4.15}$$

$n_{pore}$, $c_{p,i}$ and $y_i$ define the amount of molecules in the pore system, the heat capacity and the molar fraction of component $i$. The heat transfer between fiber and wax $\partial Q_{WF}/\partial t$ is calculated as follows:

$$\frac{\partial Q_{WF}}{\partial t} = dz\ d_{FO}\ \pi\ (T_F - T_W)\ k_{WF} \tag{4.16}$$

$d_{FO}$ (see Figure 4.2), $T_F$ and $T_W$ are the outer diameter, temperature of the fiber and the temperature of the wax. $k_{WF}$ represents the heat transfer coefficient between fiber and wax. For simplification, the thermal conductivity $\lambda_{imp}$ of the impermeable layer is applied as the major heat transfer resistance (see Figure 4.2).

$$\frac{\partial Q_{WF}}{\partial t} = dz\ d_a\ \pi\ (T_F - T_W)\ \frac{\lambda_{imp}}{d_{imp}} \tag{4.17}$$

$d_{imp}$ represents the thickness of the impermeable layer. The temperature changes during the process due to the release and uptake of the heat of adsorption, respectively. This term is calculated with the following expression:

$$\frac{\partial H_{Ad}}{\partial t} = \Delta H_{Ads}\ A_F\ (1-\epsilon)\ dz\ \frac{\partial q_{CO_2}}{\partial t} \tag{4.18}$$

$\Delta H_{Ads}$ is the heat of adsorption, $A_F$ the cross-sectional area of the fiber, $\epsilon$ the porosity and $dz$ the length of a discrete element.

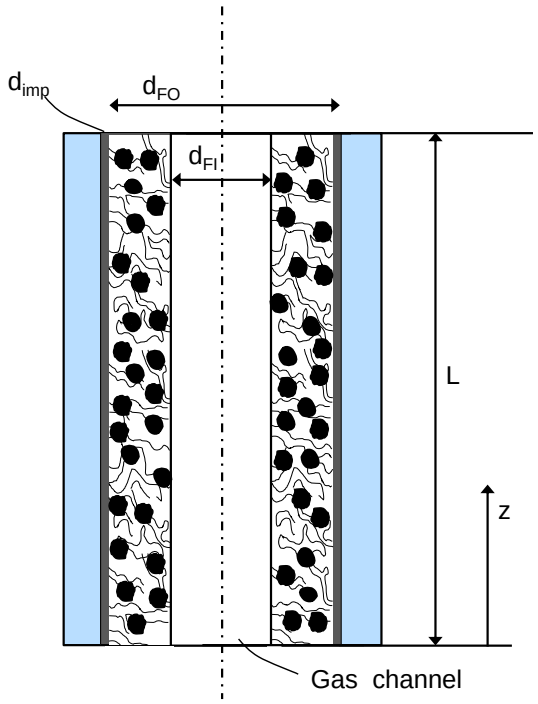


**Figure 4.2:** Scheme of the modeled hollow fiber sorbent with geometrical relations. $d_{imp}$ represents the thickness of the gas impermeable layer $d_{FO}$, the outer fiber diameter and $d_{FO}$ the inner fiber diameter.



Additionally, the energy balance for the thermal moderator, i.e. wax, which ensures almost isothermal operation, is modeled. Therefore, a paraffin wax with a phase transition temperature slightly above feed temperature is used [Bess2010]. The energy released by the $CO_2$ sorption increases the temperature of the fiber adsorbent until it reaches the melting point of the wax. Then, the heat is captured by the phase transition enthalpy of the wax. The enthalpy balance for the wax phase is described by:

$$0 = -\frac{\partial Q_{WF}}{\partial t} + \frac{\partial H_W}{\partial t} \tag{4.19}$$

$\partial Q_{WF}/\partial t$ is the heat transfer between the fiber and the phase wax and $\partial H_W/\partial t$ is the time derivative of the wax enthalpy. The following discontinuous equation describes the time derivative of the wax enthalpy $\partial H_W/\partial t$:

$$\frac{\partial H_W}{\partial t} = \begin{cases} n_W \; c_{p,W} \; \frac{\partial T_W}{\partial t} & \text{if} \quad H_{s,W} < H_W \text{ or } H_W < H_{m,W} \\ \frac{\partial n_{W,m}}{\partial t} \; \Delta H_{Fus} + n_W \; c_{p,W} \; \frac{\partial T_W}{\partial t} & \text{if} \quad H_{m,W} \leq H_W \leq H_{s,W} \end{cases} \tag{4.20}$$

$n_W$, $c_{p,W}$ and $T_W$ define the amount of substance, the heat capacity and the temperature of the wax. The first case defines the condition, in which the wax is either completely solid ($H_W < H_{m,W}$) or completely melted ($H_W > H_{s,W}$). The wax phase changes its aggregate state between these conditions. Thereby, the enthalpy of fusion $\Delta H_{Fus}$ is released or absorbed, respectively. $\partial n_{W,m}/\partial t$ is the amount of wax which changes its aggregate state. The enthalpy of the paraffin wax is approximated with a smooth exponential expression to avoid discontinuous functions, which increase the computational complexity [Ogoh2009]:

$$\frac{\partial H_W}{\partial t} = m_W \; c'_{p,W} \; \frac{\partial T_W}{\partial t} \tag{4.21}$$

with $c'_{p,W}$:

$$c'_{p,W} = A_W \; exp(-B_W \; (\frac{T_W - C_W}{D_W})^2) \tag{4.22}$$

The values for $A_W$, $B_W$, $C_W$ and $D_W$ represent fitted values. Figure 4.3 shows the specific enthalpy for both the continuous and discontinuous formulation of the specific wax enthalpy. Here, the melting temperature is 333.15 K.

### Adsorption

The adsorption rate into the fiber wall is described by the linear driving force (LDF) approach, which is commonly used due to its simplicity and physical consistency [Sirc2000b]:

$$\frac{\partial q_{CO_2}}{\partial t} = k \; (q_{e,CO_2} - q_{CO_2}) \tag{4.23}$$

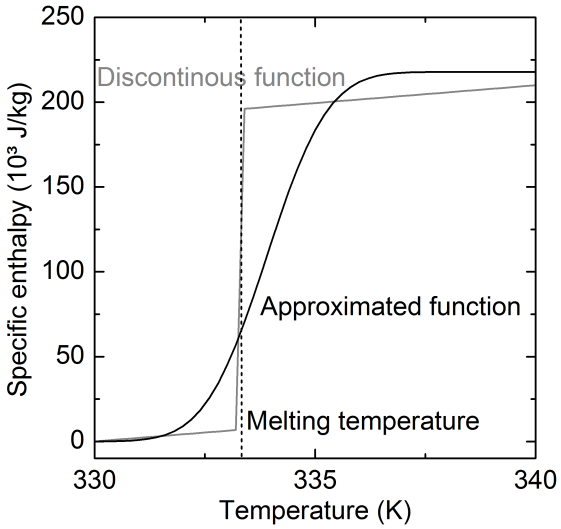


**Figure 4.3:** Approximation of the phase change of the wax by a continuous equation.



The time derivative of the loading $\partial q_{CO_2}/\partial t$ is determined by the difference of the loading equilibrium $q_{e,CO_2}$ and the current loading $q_{CO_2}$ multiplied with the LDF coefficient $k$. For hollow fiber sorbents, the $CO_2$ sorption takes place in both the zeolite particles as well as the polymer matrix. Since the adsorption capacity of both materials for $CO_2$ is significantly higher than the $H_2$ adsorption, only the adsorption of $CO_2$ is considered. The adsorption capacity of the zeolite NaY is determined with the Langmuir approach [Chou1995]:

$$q_{e,Z} = q_{s,Z}\,\frac{b_Z\; p_{CO_2}}{1 + b_Z\; p_{CO_2}} \quad , \tag{4.24}$$

where $q_{s,Z}$ and $b_Z$ stand for the maximum adsorption capacity and the equilibrium constant of the zeolite. The values of the adsorption parameter can be found in [Ohs2018b]. $p_{CO_2}$ symbolizes the partial pressure of $CO_2$.

For the CA matrix, the dual sorption model describes the $CO_2$-adsorption, which results in the following expression for the loading capacity of the polymer $q_{e,CA}$ [Bess2010]:

$$q_{e,CA} = H\; P_{CO_2} + q_{s,CA}\,\frac{b_{CA}\; P_{CO_2}}{1 + b_{CA}\; P_{CO_2}} \tag{4.25}$$

Here, $H$, $q_{s,CA}$ and $b_{CA}$ describe the Henry parameter, the maximum adsorption capacity and the equilibrium constant of the CA, respectively. With the volume percentages $\phi$ and densities $\rho$ of the zeolite and the CA, the volume-specific loading capacity ($q_{e,F}$) of the fiber module is determined as follows [Live2012b]:

$$q_{e,F} = \phi_Z \ \rho_Z \ q_{e,Z} + \phi_{CA} \ \rho_{CA} \ q_{e,CA} \tag{4.26}$$

However, the adsorption capacity of the zeolite NaY is much higher than the capacity of cellulose acetate. Therefore, the zeolite is primarily responsible for the adsorption.
The adsorption kinetics are described by the LDF approach (see (4.23)). The LDF coefficient $k$ is reciprocal to the total mass transfer resistance $R_{MT}$ multiplied with the slope of the adsorption isotherm $K$ [Ruth1994]:

$$k = \frac{1}{K \ R_{MT}} \tag{4.27}$$

The total mass transfer comprises the reistances in serial: the external film resistance $R_{MT,e}$, the intrafiber resistance $R_{MT,w}$ and the intracrystalline resistance $R_{MT,i}$ [Ruth1994]:

$$R_{MT} = R_{MT,e} + R_{MT,w} + R_{MT,i} \tag{4.28}$$

The determination of the three resistances can be found elsewhere [Bess2010].

### Axial lumen side pressure loss

The pressure drop $\partial p/\partial z$ due to the convective flow through the hollow fiber is calculated by Darcy's law as a simplified form of the averaged momentum balance [Yoon2008]:

$$\frac{\partial p}{\partial z} + \frac{32 \ \mu \ v_z}{d_{FI}^2} = 0 \tag{4.29}$$

with $\mu$ as the viscosity of the gas phase and $d_{FI}$ as the inner diameter of the hollow fiber (see Figure 4.2).

**Table 4.1:** Boundary conditions for the PSA cycle

.

| Pressurization | Adsorption | Blow-down | Desorption |
|---|---|---|---|
| $\frac{\partial y_{CO_2}}{\partial z}\|_{z=0} = 0$ | $y_{CO_2}\|_{z=0} = y_{CO_2,F}$ | $\frac{\partial y_{CO_2}}{\partial z}\|_{z=0} = 0$ | $\frac{\partial y_{CO_2}}{\partial z}\|_{z=0} = 0$ |
| $y_{CO_2}\|_{z=L} = y_{CO_2,P}$ | $\frac{\partial y_{CO_2}}{\partial z}\|_{z=L} = 0$ | $\frac{\partial y_{CO_2}}{\partial z}\|_{z=L} = 0$ | $y_{CO_2}\|_{z=L} = y_{CO_2,P}$ |
| $v\|_{z=0} = 0$ | $v\|_{z=0} = v_0$ | $\frac{\partial v}{\partial z}\|_{z=0} = 0$ | $\frac{\partial v}{\partial z}\|_{z=0} = 0$ |
| $\frac{\partial v}{\partial z}\|_{z=L} = 0$ | $\frac{\partial v}{\partial z}\|_{z=L} = 0$ | $v\|_{z=L} = 0$ | $v\|_{z=L} = f' \cdot v_0$ |
| $\frac{\partial p}{\partial z}\|_{z=0} = 0$ | $\frac{\partial p}{\partial z}\|_{z=0} = 0$ | $\frac{\partial p}{\partial t}\|_{z=0} = \frac{p_{De}-p_{Ad}}{t_{dep}}$ | $\frac{\partial p}{\partial t}\|_{z=0} = 0$ |
| $\frac{\partial p}{\partial t}\|_{z=L} = \frac{p_{Ad}-p_{De}}{t_{pre}}$ | $\frac{\partial p}{\partial t}\|_{z=L} = 0$ | $\frac{\partial p}{\partial t}\|_{z=L} = 0$ | $\frac{\partial p}{\partial z}\|_{z=L} = 0$ |

The cross-sectional area of the flow channel $A_{HF}$ and the fiber $A_F$ are calculated as follows:

$$A_{HF} = \frac{d_{FI}^2\,\pi}{4} \tag{4.30}$$

and

$$A_F = \frac{(d_{FO}^2 - d_{FI}^2)\,\pi}{4} \tag{4.31}$$

Here, $d_{FO}$ symbolizes the outer diameter of the hollow fiber (see Figure 4.2).

### 4.2.4 Process model

#### Boundary conditions

The PSA process is fully described if boundary conditions for the four discrete time steps of a Skarstrom PSA cycle (pressurization, adsorption, blow-down, desorption, see Figure 4.1) are provided at the inlet ($z = 0$) and the outlet ($z = L$) of the hollow fiber sorbent. Table 4.1 summarizes the boundary conditions applied in this chapter.

For optimization, an end-point constraint for the purity of the product

stream is used:

$$Purity \geq Purity_{min} \tag{4.32}$$

with

$$Purity = \frac{\int_{t_{dep}+t_{des}+t_{pre}}^{t_{cycle}} \dot{n}_{\mathsf{H_2}}|_{z=L}\ dt}{\int_{t_{dep}+t_{des}+t_{pre}}^{t_{cycle}} \dot{n}|_{z=L}\ dt} \tag{4.33}$$

Here, $\dot{n}_{\mathsf{H_2}}$ and $\dot{n}$ represent the $H_2$ and total product stream, respectively.

### Cyclic steady state

PSA processes never reach a steady state due to the alternation between adsorption and desorption. However, PSA processes show periodic dynamic equilibrium behavior after multiple cycles, which is called the cyclic steady state (CSS). The determination of the CSS poses special challenges on the modeling and optimization of PSA processes but at least two different methods are commonly applied:

- successive substitution,
- direct determination.

For the successive substitution, the PSA cycle is simulated multiple times until the state variables $x$ at the beginning and the end of a cycle are equal:

$$x(t_{cycle} + t) - x(t) = 0 \tag{4.34}$$

with $t_{cycle}$ as the full cycle time. To reduce the computational effort and to increase the robustness of the optimization problem, a slight deviation of the cyclic steady state condition with a deviation tolerance $\epsilon$ is allowed. Furthermore, an integral relationship over the spatial domain can be applied:

$$\int_0^{z=1} (x(z, t + t_{cycle}) - x(z, t = t))^2 dz < \epsilon \tag{4.35}$$

$\epsilon$ is the deviation tolerance for the cyclic steady state. Its value is decisive for the accuracy of the CSS. To account for differeent fiber lengths, we normalized the axial direction ($z = 1$).

The CSS condition (4.35) is used as a two point boundary condition for the direct determination approach to overcome the need for calculating multiple cycles and thus reduce the computational costs further (please refer to the literature [Jian2003] for differences in computational efforts). Then, the CSS is determined by the following expression [Smit1991]:

$$\int_0^{z=1} (x(z, t_{cycle}) - x(z, t = 0))^2 dz < \epsilon_{DD} \tag{4.36}$$

$x(z, t_{cycle})$ and $x(z, t = 0)$ describe the state variables at the beginning (t=0) and the end of a cycle ($t_{z,cycle}$). $\epsilon_{DD}$ is the deviation tolerance for the cyclic steady state. For the direct determination approach, the initial values of the state variables $x(t = 0)$ are not constant but implicitly defined by a set of equality constraints. Therefore, the initial values of the state variables are commonly iterated via a Newton based method of the optimization solver. Detailed information can be found in the work of Jiang et al. [Jian2003].

Ko and Biegler expressed the spatial dependence of the state variables by the following equations to reduce the computational effort further [Ko2003]:

$$q(z, t = 0) = k_{a,q} + \frac{k_{b,q}}{1 + e^{k_{c,q} + k_{d,q}\ z}} \quad , \tag{4.37}$$

$$y(z, t = 0) = k_{a,y} + \frac{k_{b,y}}{1 + e^{k_{c,y} + k_{d,y}\ z}} \quad , \tag{4.38}$$

$$p(z, t = 0) = p_A + (1 - z)\ p_{drop} \tag{4.39}$$

Here, $q$, $y$ and $p$ are the state variables over the axial coordinate $z$ and

represent the loading, the molar fraction of one specific component in the gas phase and the pressure. The variables $k_{a,q}$, $k_{b,q}$, $k_{c,q}$, $k_{d,y}$, $k_{a,y}$, $k_{b,y}$, $k_{c,y}$, $k_{d,y}$ as well as $p_A$ and $p_{drop}$ determine the spatial profile of the state and optimization variables. The end of the adsorption step and the begin of the depressurization were chosen as the cycle point for which the CSS condition was applied.

### 4.2.5 Economics

The economic evaluation comprises the investment costs, the operation costs and the costs for lost revenues due to incomplete recovery. The total investment costs $I$ are composed of the acquisition and montage costs for (i) the hollow fiber adsorber modules $I_F$, (ii) the module housing $I_{HC}$ and (iii) the compressor $I_{Comp}$:

$$I = I_F + I_{HC} + I_{Comp} \tag{4.40}$$

The annual cost (AC) are then calculated as follows:

$$AC = I \, \frac{(1+i)^{n_l} \, i}{(1+i)^{n_l} - 1} \tag{4.41}$$

with $i$ as the calculative interest rate and $n_l$ as the plant life time.

Currently, any price for hollow fiber sorbent modules are available in the literature as they have not been commercialized yet. However, we think that a similar price to hollow fiber membrane modules for gas permeation is appropriate since the fabrication process is comparable. Thus, as for membrane processes, we assume that the investment costs $I_F$ depend on the total area of the hollow fibers $A_F$ [Ohs2016]:

$$I_F = A_F \, C_F \tag{4.42}$$

with $C_F$ as the costs per surface area of the fiber. The surface area $A_F$ is calculated by the arithmetic mean $d_m$ of the inner diameter $d_{FI}$ and outer diameter $d_{FO}$ and the length $L$ multiplied with the total number of fibers

$N_{TF}$:

$$A_F = L\ d_m\ \pi\ N_{TF} \tag{4.43}$$

with

$$d_m = \frac{d_{FI} + d_{FO}}{2} \tag{4.44}$$

The total number of fibers $N_{TF}$ comprises the number of modules $N_{Mod}$ and the number of fibers per module $N_F$, which is determined by the packing fraction $\rho_{pack}$:

$$N_{TF} = N_{Mod}\ N_F = N_{Mod}\ \rho_{pack}\ \frac{d_{Mod}^2}{4\ d_F} \tag{4.45}$$

Therefore, the housing costs for the hollow fiber module $I_{HC}$ are determined by the following expression:

$$I_{HC} = N_{Mod}\ C_{Mod} \tag{4.46}$$

with $C_{Mod}$ as the housing costs. The costs for the valves for switching between the process steps are not considered in the cost calculations because it is expected that they do not differ for different process conditions.

The investment costs $I_{Comp}$ for the compressor can be approximated with the method of Guthrie and are based on its nominal electrical power ($P_{el}$) [Bieg1997]:

$$I_{Comp} = UF\ (MPF + MP + 1)\ C_0\ (P_{el}/S_0)^{\alpha} \tag{4.47}$$

Here, $UF$ is the update factor and $MP$ the montage and piping costs. The factor $MPF$ considers special temperature and pressure related requirements for the material. $C_0$, $S_0$ and $\alpha$ represent the basic costs, the basic capacity and a fractional exponent, respectively. The electrical power $P_{el}$

for compression is approximated as follows:

$$P_{el} = \frac{1}{\eta_{el}\,\eta_c}\,\frac{\partial n_{Feed}}{\partial t}\,\frac{\kappa}{\kappa-1}\,R\,T_{Feed}\left(\left(\frac{P_{Ad}}{P_0}\right)^{\frac{\kappa-1}{\kappa}}-1\right) \tag{4.48}$$

The efficiency factors $\eta_{el}$ for the electric motor and the compression $\eta_c$ are assumed to be $0.9$ and $0.8$, respectively. The constants $\kappa$ and $R$ express the isentropic expansion factor and the ideal gas constant. $\partial n_{Feed}/\partial t$, $p_{Ad}$ and $T_{Feed}$ define the molar feed flow, the adsorption pressure and the feed temperature. The energy costs per year ($C_{Energy}$) for compression, another important costs factor for the PSA process, are determined as follows:

$$C_{Energy} = P_{el}\,\tau\,c_{el} \tag{4.49}$$



with $\tau$ as the annual operating time and $c_{el}$ as the electricity costs, respectively. The costs due to product losses per year are calculated as follows:

$$C_{loss} = \frac{\partial n_{Feed}/\partial t\;T_{Feed}\;R}{p_{Ad}}\tau\;C_{\mathsf{H_2}}(1-\xi) \tag{4.50}$$

with $C_{\mathsf{H_2}}$ as the price of hydrogen per cubic meter. The recovery $\xi$ is determined by the following expression:

$$\xi = 1 - \frac{\int_0^{t_{dep}+t_{des}} \dot{n}_{H_2}|_{z=0}\;dt}{\int_0^{t_{ads}} \dot{n}_{Feed,H_2}\;dt} \tag{4.51}$$

where $t_{ads}$, $t_{dep}$, $t_{des}$ and $t_{pre}$ symbolize the time for the adsorption, depressurization, desorption and pressurization step. $\dot{n}_{H_2}$ describes the molar $H_2$ flow rate in the waste stream at the outlet of the column (position z = 0) and $\dot{n}_{Feed,H_2}$ represents the supplied hydrogen feed flow. With these equations, the total costs per year $C_{total}$, which are minimized by the optimization, can be calculated:

$$C_{total} = C_{loss} + AC + C_{Energy} \tag{4.52}$$

In addition, the costs per cubic meter product $C_V$ are calculated as follows:

$$C_V = \frac{C_{total}}{\partial V_{Product}/\partial t} \tag{4.53}$$

The objective function $C_{total}$ depends on parameters that may vary with location and time (we assumed European cost parameters in this chapter). Nevertheless, we think that using the annual costs as objective function allows comprising the different trade-offs of PSA processes into a single criterion. For example, the recovery and power consumption oppose each other, which results in an inevitable trade-off. Other studies often neglected the costs for incomplete recovery [Ko2003], and optimal design can not be identified. By consolidating the trade-offs into a single variable a multi-objective optimization is not necessary. Other process objectives such as product purity are constrained by the boundary conditions. Thus, as opposed to previous works a more holistic optimization is possible.



Furthermore, the energetic efficiency $\eta$ of the processes is an important performance indicator:

$$\eta = 1 - \frac{P_{el}}{LHV_{H_2}\ \partial n_{Product}/\partial t} \tag{4.54}$$

with $P_{Com,total}$ as the compression duty, $\text{LHV}_{H_2}$ as the lower heating value of $H_2$ and $\partial n_{Product}/\partial t$ as the product flow rate.

### 4.2.6 Optimization approach and annual costs as objective function

The optimization problem, which minimizes the total annual costs $C_{total}$, is written as follows:

$$\begin{aligned} & \min_{x(\cdot),y(\cdot),t_{cycle},p} C_{total} \\ \text{s.t. } 0 &= f(\frac{dx}{dt}, x, y, t, a), \qquad t \in [0, t_{cycle}], \\ 0 &= g(x, y, t, a), \qquad t \in [0, t_{cycle}], \\ 0 &\geq h(x, y, t, a), \qquad t \in [0, t_{cycle}], \\ 0 &= x(t = t_{cycle}) - x_0 \end{aligned} \tag{4.55}$$

The equality constraints $f$ and $g$ describe a set of differential algebraic and algebraic equations. The inequality constraints are summarized using the function $h$. $x$ represents the vector of differential variables, such as the pressure, $y$ the vector of the time-variant algebraic variables, e.g. adsorption equilibrium, $a$ the vector of the time-invariant parameters, e.g. adsorption constants, and $t$ the time. The PSA process is described by a system of partial differential algebraic equations (PDAE). In this chapter, a sequential single discretization approach is used to solve this system [Ko2003]. By this method, the spatial domain of the PDAE system is discretized by the method of lines. Thus, the PDAE system is converted to a system of differential algebraic equations (DAE). The DAE system is solved by DASOLV, which is available in gPROMS. DASOLV exploits a backward differentiation formula (BDF) for the numerical calculation of DAE systems. For the dynamic optimization of the DAE system, we used the local optimization solver CVP SS (control vector parameterization (CVP), Single-shooting (SS)), which allows identifying local optima. The spatial dependence of the state variables ($\frac{dx}{dz}$) is calculated depending on the flow direction with a backward (BFDM) or a forward finite difference method (FFDM) (upwind scheme).

## 4.3 Case study

Hydrogen ($H_2$) is a very promising energy carrier [Barr2003] and an important feedstock for the chemical industry [Stol2016], e.g. for the ammonia [Eris2008] and methanol production [Chen1994]. Currently, it is mainly produced from fossil resources such as natural gas [Venn2011]. For a more sustainable future, alternative production routes must be developed [Edwa2008]. For example, fermentation processes can use waste stream as renewable feedstock [Levi2004; Kapd2006]. This also allows combining waste treatment and energy production. Unfortunately, besides $H_2$ such a process produces $CO_2$ as well, which must be removed before $H_2$ utilization. A wide range of fermentation exhaust gas compositions can be obtained depending on the feedstock and operation conditions [Bhar2016]. In particular, processes based on selective membranes [Bako2013a; Hara2007; Horv2004] and membrane contactors [Modi2008; Tepl2002] have been investigated. Membrane processes benefit from a low energy consumption [Sand2013], small footprints [Bern2009] as well as the possibility of flexible operation. However, hydrogen utilization often requires high purities [Loff2003; Huft1999] but producing high purity hydrogen using a stand-alone membrane process usually results in high costs [Brun2010]. In comparison, pressure-swing adsorption (PSA) processes are well known and widely used for the production of highly pure hydrogen [Sirc2000a].

In this chapter, we optimized a PSA process for hydrogen purification using hollow fiber sorbents. The feed condition and the product requirements are given in Table 4.2. A small-volume feed flow rate of 150 $m^3$/h is considered which is usually obtained in decentralized hydrogen production processes. These small-scale processes with possibly varying product flow rates can benefit from the modular design of hollow fiber sorbents as a simple up-scaling is possible. Also trace components, such as humidity, are present in the gas stream and have to be removed prior to $H_2/CO_2$ separation, as they might limit the adsorption capacity of the hollow fiber. Thus, we assume that only $H_2$ and $CO_2$ are present in the gas stream and besides the PSA process several upgrading steps to remove the trace components

will be required. These may result in recycle streams, which influence the feed gas composition of the PSA process. As discussed above, the $H_2$ can vary significantly depending on the process parameters such as the feedstock's origin. As it is impossible to investigate all production scenarios, we define a reference case with a molar hydrogen fraction of 75 % at ambient conditions. This feed gas composition may represent a wide range of feedstock and represent a gas composition where a high recovery with PSA processes is still possible. The required product purity in this chapter was $\geq$ 99 mol-%. Also higher product purities were investigated in section 4.4.3. The physical and the economical parameter of the hollow fiber sorbent can be found in [Ohs2018b].



**Table 4.2:** Important process parameters for the case study.

| Case study parameters | Value | Unit |
|---|---|---|
| Feed rate | 150 | $Nm^3/h$ |
| Feed $H_2$ concentration | 75 | mol-% |
| Feed gas pressure | 1 | bar |
| Purity | $\geq$ 99 | mol-% |
| Operating time per year | 8000 | h/a |

Additionally, we define a reference case for the process and fiber design, which we use to compare the optimization results. The reference parameters are given in 4.3.

Table 4.4 summarizes the process optimization variables as well as their lower and upper bounds. As indicated above, the uniqueness of this chapter lies in the fact that not only the optimal operating parameters , e.g. adsorption pressure and purge ratio but also the optimal design of the hollow fiber sorbent, e.g. inner and outer diameter, are identified. In comparison, previous studies focused only on the optimization of process conditions such as operating pressure and total bed size [Ko2003; Ko2005]. We are now applying a more holistic approach by also incorporating the adsorbent design itself. This allows us to determine the interplay between hollow fiber sorbent and process design, as well its dependency on important pro-

**Table 4.3:** Reference parameters for hollow fiber sorbent process

| Variable | Unit | Value |
|---|---|---|
| Length $L$ [Ko2003; Yang1997] | m | 1 |
| Inner diameter $d_{FI}$ [Bess2010] | $10^{-3}$ m | 0.462 |
| Outer diameter $d_{FO}$ [Bess2010] | $10^{-3}$ m | 1.03 |
| Total number of fibers $N_{TF}$ [Live2012b] | $10^3$ | 156 |
| Adsorption pressure $p_{Ad}$ [Live2012b] | bar | 7.8 |
| Desorption pressure $p_{De}$ [Live2012b] | bar | 1 |
| Purge / feed flow ratio [Yang1997] | % | 7 |
| Pressurization time $t_p$ [Yang1997] | s | 45 |
| Adsorption time $t_p$ [Yang1997] | s | 180 |



cesses requirements.

**Table 4.4:** Applied bounds and start values of the optimization parameters

| Variable | Unit | Initial value | Lower bound | Upper bound |
|---|---|---|---|---|
| Length $L$ | m | 1 | 0.5 | 1.4 |
| Inner diameter $d_{FI}$ | $10^{-3}$ m | 0.45 | 0.3 | 0.5 |
| Outer diameter $d_{FO}$ | $10^{-3}$ m | 1 | 0.8 | 1.1 |
| Total number of fibers $N_{TF}$ | $10^3$ | 156 | 0 | 1 000 |
| Adsorption pressure $p_{Ad}$ | bar | 8 | 6 | 12 |
| Purge / feed ration | % | 5 | 1 | 10 |
| Pressurization time $t_p$ | s | 50 | 45 | 55 |
| Adsorption time $t_p$ | s | 180 | 120 | 210 |



## 4.4 Results and discussion

### 4.4.1 Simulation of the hollow fiber sorbent

This section discusses the general behavior of the hollow fiber sorbent. Figure 4.4 (a) shows the gas phase composition at different adsorption times for the reference case. Sharp breakthrough curves due to well-defined flow conditions are achieved with hollow fiber sorbents. For a feed flow rate of 0.266 $Ncm^3 \cdot s^{-1}$ per fiber and a fiber length of 1 m, the $CO_2$ breakthrough time is 280 s. Subsequently, the fiber is regenerated by desorption and purging with $H_2$. Figure 4.4 (b) represents the adsorbent loading for a purge ratio of 7 % and a total desorption pressure of 1 bar. Interestingly, the hollow fiber sorbent cannot be fully regenerated during the desorption time (which is usually limited by the adsorption duration in multi-bed processes).

Since the hollow fiber sorbent is not fully regenerated during the desorption step, the loading at the end of each cycle increases until the cyclic steady-state is reached. Thus, for the first cycle, the hollow fiber sorbent cannot be loaded fully to prevent breakthrough for later cycles. Figure 4.5 represents the accumulation of $CO_2$ in the fiber over several cycles. For the parameters given, the fiber can only be loaded up to 60 % at the first cycle,

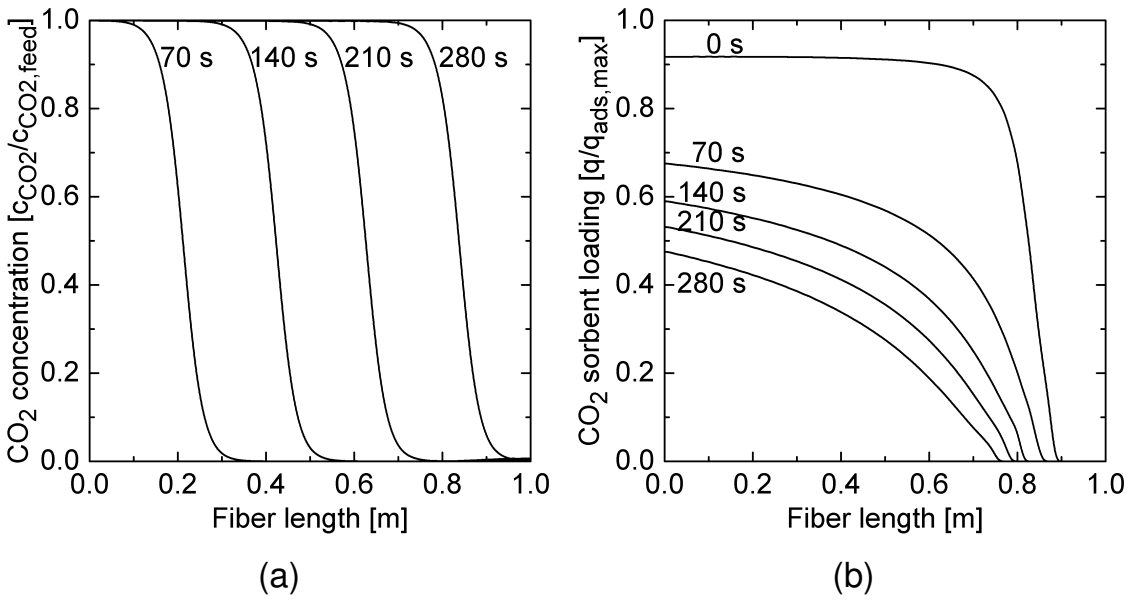


**Figure 4.4:** (a) Development of the local relative $CO_2$ gas concentration during the adsorption step, (b) Development of the local fiber loading during the desorption step.



which reduces the adsorption time down to 180 s. Furthermore, it takes up to ten cycles until the cyclic steady state is reached. Thus, it is computationally intense and time-consuming to find an appropriate operation mode and advanced methods are required to find optimal process conditions.

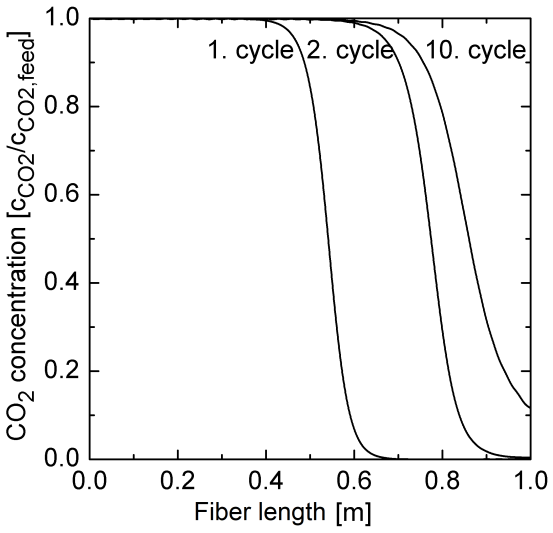


**Figure 4.5:** Accumulation of the $CO_2$ at the end of the adsorption step until cyclic steady state is reached. The adsorption step has a duration of 180 s.

### 4.4.2 Determination of cyclic steady state and isothermal process due to thermal moderation

To reduce the computational efforts, the cyclic steady state can also be determined by the direct determination approach. Figure 4.6 compares the $CO_2$ fraction at the end of the adsorption step at CSS determined by the two CSS approaches discussed above (see section 4.2.4). The direct determination approach according to (4.36) is very accurate for hollow fiber sorbents. Equivalently, very good agreements are obtained for other process variables such as the $CO_2$ loading.

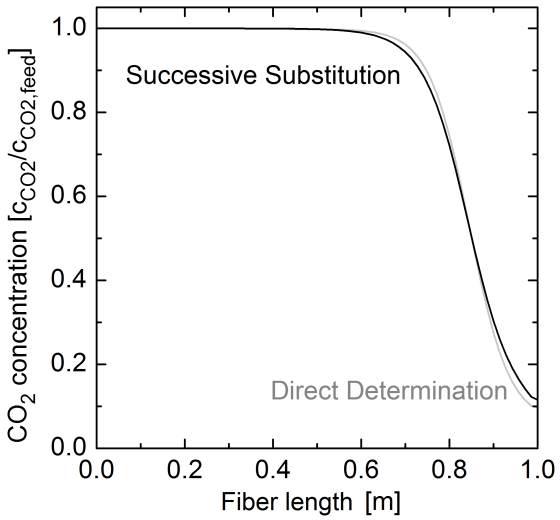


**Figure 4.6:** Relative $CO_2$-concentration profile at the end of the adsorption step for direct determination and successive substitution. Equivalently, a good a agreement is obtained for the $CO_2$ loading of the adsorbent (not shown here).

The uptake of the adsorption heat by the wax, which reduces temperature fluctuation, is one of the main advantages of hollow fiber sorbents. The temperature profiles for the hollow fiber sorbent based process at the end of the adsorption and desorption step are shown in Figure 4.7. Interestingly, the temperature only varies minimally for hollow fiber sorbents. This was also observed in experimental studies [Live2012b]. Thus, in the following, isothermal operations can be assumed and the energy balance is not considered for process optimization. In comparison, for packed-bed-based PSA processes, periodic temperature changes due to the exothermic ad-

sorption and endothermic desorption occur.

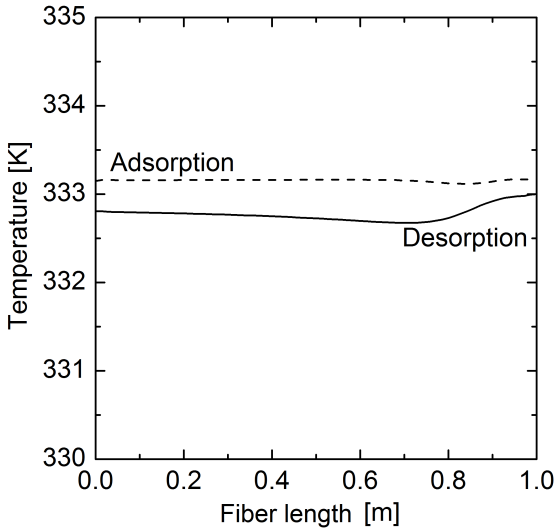


**Figure 4.7:** Temperature profiles in the hollow fiber sorbent at the end of the adsorption and desorption step. Only small temperature fluctuations in hollow fiber due to the thermal moderator occur. This has also been shown experimentally [Live2012b]



### 4.4.3 Optimization of hollow fiber sorbent processes

As discussed above, designing PSA processes is challenging as many trade-offs between the design variables exist. The presented reference case results in purification costs of 0.75 €/kg. compared with hydrogen costs of about 3-8 € per kg [Offe2010], this value is relatively low. However, it must be mentioned that the $H_2$ production and pre-purification steps are not considered yet and need to be included for further investigations. The $H_2$ recovery is 85 %.

The optimization study aims to reduce the purification costs further by optimizing the variables shown in Table 4.4. At the optimal operating point, the hydrogen recovery is 89.8 mol-% resulting in specific purification costs of 0.65 €/kg product, which are approximately 13 % lower compared as in the reference case. This is a significant cost reduction for a commodity product such as hydrogen. As discussed above, a trade-off for the length of adsorption beds exist. Long adsorption beds suffer from high pressure loss

and thus reduced efficiency. In comparison, short-adsorption beds result in short adsorption times which requires high-frequent switching between the cycle steps. As this is related with unnecessary product losses, the overall recovery of the process is reduced. Thus, an optimal fiber length exists. For a product purity of 99 mol-%, the optimal module length is slightly shorter than 1 m (see Table 4.5), which is in the range of commercial hollow fiber membrane modules for gas separation [Coke1998] and has also been identified as the optimal length for PSA-based processes for $CO_2$ sequestration using conventional packed-bed adsorber [Ko2003]. In comparison to packed-bed adsorber, the mass transfer resistance caused by the fiber thickness as well as the pressure drop, caused by the fiber length and the bore diameter can be optimized individually, which is an advantage of hollow fiber sorbents. The inner and outer diameter are about 20 % and 10 % (0.462 mm vs. 0.38 mm and 1.03 vs. 0.89 mm, respectively) lower compared with the reference case. The optimal operating pressure is 9.1 bar and the purge to feed ratio about 0.05. The energetic efficiency, which relates the energy required for the separation process and the LHV of hydrogen (see (4.54)), is around 94 %.



For some applications, e.g. for a hydrogen fuel cells vehicle, a hydrogen purity of 99 mol-% is not sufficient [Bess2010]. Therefore, the influence of higher product requirements on the process design is investigated. Thus, three additional optimization scenarios for hollow fiber based PSA processes are studied, in which hydrogen purities of 99.5, 99.9 and 99.99 mol-% are targeted. Table 4.6 summarizes the optimal values for the specific variables for different product purities and Figure 4.8 shows that the cost contributions for different product purities.

The purification costs using hollow fiber sorbent increase from 0.65 €/kg for a purity of 99 mol-% to 0.86 €/kg for a purity of 99.99 mol-%. This rise is based on a higher optimal operating pressure which increases from 9.1 bar to 11.3 bar. Also, the total required adsorber volume is about 10.6 % higher. Finally, the recovery decreases from 89.7 % to 85.0 % as higher product purities require higher purge streams. This represents an increase in the hydrogen loss of 50 %.

**Table 4.5:** Optimization results for hollow fiber based PSA processes for a hydrogen purity of 99 mol-%

| Variable | Unit | Reference case | Optimized design |
|---|---|---|---|
| Length $L$ | cm | 100 | 99.6 |
| Inner diameter $d_{FI}$ | $10^{-3}$ m | 0.462 | 0.38 |
| Outer diameter $d_{FO}$ | $10^{-3}$ m | 1.03 | 0.89 |
| Total number of fibers $N_{TF}$ | $10^3$ | 156 | 202 |
| Adsorption pressure $p_{Ad}$ | bar | 7.8 | 9.1 |
| Purge / feed ratio | % | 7 | 4.58 |
| Adsorption time $t_{ads}$ | s | 180 | 120 |
| Pressurization time $t_p$ | s | 45 | 45 |
| $H_2$-Recovery $\xi$ | % | 85.0 | 89.8 |
| Specific cost €/kg | % | 0.75 | 0.65 |
| Energetic efficiency $\eta$ | - | 0.94 | 0.94 |

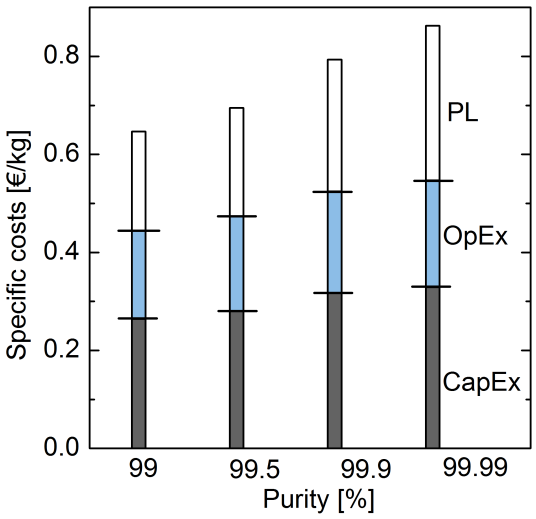


**Figure 4.8:** Specific purification costs for different $H_2$ product purities. Also, the contribution to the total costs, i.e. capital expenditure (CapEx), operational expenditure (OpEx) as well as product loss (PL) are given.

**Table 4.6:** Optimization results for hollow fiber based PSA processes targeting different product purities.

| Variable | Unit | 99 mol-% | 99.5 mol-% | 99.9 mol-% | 99.99 mol-% |
|---|---|---|---|---|---|
| Length $L$ | cm | 99.6 | 96.2 | 94.4 | 99.6 |
| Inner diameter $d_{FI}$ | $10^{-3}$ m | 0.38 | 0.35 | 0.34 | 0.33 |
| Outer diameter $d_{FO}$ | $10^{-3}$ m | 0.89 | 0.81 | 0.80 | 0.80 |
| Total number of fibers $N_{TF}$ | $10^3$ | 202 | 229 | 253 | 279 |
| Adsorption pressure $p_{Ad}$ | bar | 9.1 | 10.2 | 10.8 | 11.3 |
| Purge / feed ratio | % | 4.58 | 5.67 | 7.13 | 8.24 |
| Adsorption time $t_{ads}$ | s | 120 | 120 | 120 | 120 |
| Pressurization time $t_p$ | s | 45 | 45 | 45 | 45 |
| $H_2$-Recovery $\xi$ | % | 89.8 | 88.9 | 86.9 | 85.0 |
| Energetic efficiency $\eta$ | - | 0.94 | 0.93 | 0.93 | 0.92 |

Interestingly, the optimal inner and outer fiber diameter decreases from 0.38 to 0.33 $\cdot$ $10^{-3}$ m and from 0.89 to 0.80 $\cdot$ $10^{-3}$ m with increasing product purity because smaller diameters reduce the mass transfer resistance, which leads to sharper breakthrough curves and higher purities. Similar optimal diameters have been reported before [Bhan2010] but have not been proven to exist in combination with process optimization. The reduction of the fiber diameter is compensated by an increased number of fibers. Thus, the energetic efficiency is only reduced slightly due to the sophisticated process design.

Currently, many researchers focus on the development of new adsorption materials with high adsorption capacities, which promise to increase the performance of PSA processes. Thus, we analyzed the reduction of process costs for increased adsorption capacities. Therefore, we optimized PSA processes while assuming the availability of materials with 1.25 and 1.5 times higher adsorption capacities. The resulting adsorption isotherms and the dependence of specific costs on the increased adsorption capaci-

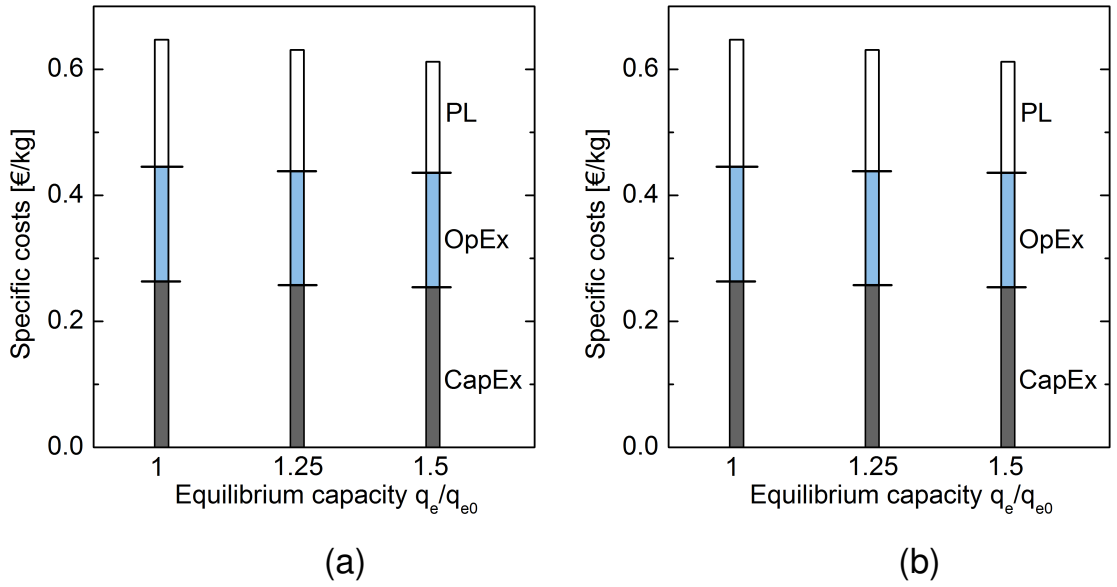


**Figure 4.9:** (a): Influence of an increased loading capacity on the adsorption isotherms, (b) Specific purification costs for the increased adsorption capacity with capital expenditure (CapEx), operational expenditure (OpEx) as well as product loss (PL).



ties $q_{e0}$ are shown in Figure 4.9.

Figure 4.9 shows that the costs decrease only slightly from 0.65 €/kg to 0.62 €/kg due to an increased loading capacity. Interestingly, the optimal operating pressure increased slightly from 9.14 bar to 9.35 bar exploiting the higher available adsorption capacity (see Table 4.7). Moreover, the investment costs for the fiber module decrease as smaller adsorber volumes are sufficient at increased loading capacity. Furthermore, the purging ratio can be decreased which increases the recovery. However, the adsorber fiber costs are small compared with the costs for compression (approximately 30% of the investment costs). Therefore, the specific costs only decrease slightly. Hence, we recommend that future work for adsorption materials should not only focus on adsorption capacity but even more on high selectivity, simple regeneration and long-time stability at real operating conditions. Interestingly, also the optimal fiber geometry only varies slightly with available adsorption capacities.

**Table 4.7:** Optimization results for a hollow fiber based PSA process with different adsorption capacities.

| Variable | Unit | 1 x $q_{eO}$ | 1.25 x $q_{eO}$ | 1.5 x $q_{eO}$ |
|---|---|---|---|---|
| Length $L$ | cm | 99.6 | 99.4 | 98.7 |
| Inner diameter $d_{FI}$ | $10^{-3}$ m | 0.38 | 0.37 | 0.36 |
| Outer diameter $d_{FO}$ | $10^{-3}$ m | 0.89 | 0.89 | 0.91 |
| Total number of fibers $n_{TF}$ | $10^3$ | 202 | 200 | 200 |
| Adsorption pressure $p_{Ad}$ | bar | 9.14 | 9.26 | 9.35 |
| Purge / feed ratio | % | 4.58 | 4.53 | 4.51 |
| Adsorption time $t_{ads}$ | s | 120 | 120 | 120 |
| Pressurization time $t_p$ | s | 45 | 45 | 45 |
| $H_2$-Recovery $\xi$ | % | 89.8 | 90.2 | 90.6 |
| Energetic efficiency $\eta$ | - | 0.94 | 0.94 | 0.94 |



## 4.5 Conclusion

Hollow fiber sorbents have shown to overcome many limitations of conventional packed-bed adsorption columns, such as (i) the interdependence of pressure loss and mass transfer resistance and (ii) well-defined flow conditions, resulting in very sharp breakthrough curves. Furthermore, isothermal process conditions can be achieved by using a thermal moderator, such as wax, which takes up the adsorption heat by the enthalpy of fusion. To reduce product loss and retain the wax, an impermeable layer serves as barrier. In this chapter, we presented an economic analysis for hollow fibers sorbents to fully exploit their potential. As a case study, we investigated the purification of hydrogen purification from small-scale hydrogen production facilities. In such processes, the modular design of hollow fiber sorbents is particularly advantageous. The hollow fiber sorbents are made of zeolites incorporated in a cellulose acetate matrix. In this kind of sorbents, the gas flows through the lumen side of the fiber, whereas the wax is placed on the shell side. The developed optimization model allows increasing the effi-

ciency and reducing the costs for hollow fiber sorbent based pressure swing adsorption. In contrast to previous works, not only the process parameters such as operating pressures and adsorption time were optimized numerically but also the design of the hollow fiber itself. The length, the inner and outer diameter provide additional degrees of freedom, which allows tuning the hollow fiber sorbent according to its specific separation task. Thus, with this chapter, we combine process and sorbent optimization for the first time.

Optimizing these variables resulted in more than 13 % lower costs as compared to a reference case defined by a process design presented in the literature. The model also allows investigating the influence of the required product purity on the process and fiber design. The optimal process pressure increases by 20 % when a product purity of 99.99 % instead of 99 % is required. The fiber design itself only varies marginally with product requirements. The optimal inner and outer fiber diameter are in the range between 0.33 and 0.38 mm as well as 0.80 and 0.89 mm, respectively. The optimal fiber length varies between 94.4 and 99.6 cm. However, the number of adsorption fibers increases with the required purity. This supports the modular concept where the addition of parallel modules allows coping with increasing capacity or purity requirements.

As future material development will reach higher adsorption capacities, we also evaluated increasing material performance. Higher adsorption capacities favor slightly higher operating pressures enabling to make use of this higher capacities. As for higher product requirements, the optimal fiber geometries do not vary significantly with adsorption capacities. The optimal inner and outer diameter was in the range of 0.33 to 0.38 $\cdot 10^{-3}$ m and 0.80 to 0.91 $\cdot 10^{-3}$ m, respectively. The optimal fiber length was in all cases about 1 m, similar to those of commercial hollow fiber membrane modules for gas separation.

# 5 Adsorption of carbon dioxide on solid amine-functionalized sorbents: A dual kinetic model



Parts of this chapter have been published as:

Burkhard Ohs, Maximilian Krödel, Matthias Wessling
*Adsorption of carbon dioxide on solid amine-functionalized sorbents: A dual kinetic model*, Separation and Purification Technology, 2018
DOI: 10.1016/j.seppur.2018.04.009

## 5.1 Introduction

In Chapter 3 and 4, the separation of (bio-)hydrogen from $CO_2$ has been discussed. However, both $CO_2$ and $H_2$ inhibit the hydrogen fermentation and thus often nitrogen sparging is applied to reduce their partial pressure. This also requires the separation of $CO_2$ and $N_2$. For this task, amine-functionalized solid sorbents are very attractive due to their outstanding adsorption capacities. However, the adsorption kinetics of these materials are still not fully understood. In particular, precise and versatile but still simple kinetic models are missing (see Chapter 2). To overcome these limitations, we propose a new semi-empirical kinetic model for the $CO_2$ adsorption on solid amine sorbents, where the $CO_2$ uptake is a function of the current $CO_2$ loading. This model allows for detailed process analysis to increase the process efficiency, to reduce the required separation energy for $CO_2$ separation processes and to evaluate the potential of new adsorption materials.



## 5.2 Models for amine-functionalized sorbents

In this chapter, we compare our dual kinetic model with the most commonly used kinetic models for $CO_2$ adsorption processes: (a) the pseudo-first-order model, (b) Avrami's fractional-order kinetic model and (c) the generalized fractional-order kinetic model. The pseudo-second-order model was not considered because it was shown that it is not suitable to describe the adsorption kinetics for amine-functionalized materials [Sern2010]. For clarity reasons the models are summarized shortly:

- Pseudo-first-order kinetic model: This is the most simple and thus most often used adsorption model for gas-solid systems:

$$\frac{\partial q_t}{\partial t} = k \cdot (q_{eq} - q_t) \tag{5.1}$$

where $k$ is the kinetic constant, $q_{eq}$ and $q_t$ represent the equilibrium loading and the current loading at time $t$, respectively.

- Avrami's fractional-order kinetic model: Avrami's fractional-order kinetic model was developed to describe the phase transition and crystal growth of materials [Lope2003], but is also suitable to describe $CO_2$ adsorption. The model can be written as follows [Sern2010]:

$$\frac{\partial q_i}{\partial t} = k_A^{n_A} \cdot t^{n_A - 1} \cdot (q_{eq,i} - q_i) \tag{5.2}$$

  where $k_A$ is Avrami's kinetic constant and $n_A$ is Avrami's exponent which is a fractional number. This parameter reflects the dimensionality of growth of adsorption sites.

- Generalized fractional-order kinetic model: The model was proposed by Heydari-Gorji et al. [Sern2010; Heyd2011b]. In this model, the adsorption rate is proportional to the $n$th power of the driving force and the $m$th power of the adsorption time:

$$\frac{\partial q_t}{\partial t} = k_G \cdot t^{m_G - 1} \cdot (q_{eq} - q_t)^{n_G} \tag{5.3}$$

  where $k_G$, $m_G$ and $n_G$ are the constants for the generalized fractional-order kinetic model. For $m_G = 1$ and $n_G = 1$ or $n_G = 2$ the generalized model reduces to pseudo-first-order or pseudo-second-order model, respectively.

- Our new semi-empirical dual kinetic model (DKM): For amine-functionalized solid materials, several overlaying phenomena influence the adsorption kinetics. Thus, the overall adsorption $q_t$ is the sum of the surface $q_{sur}$ and bulk sorption $q_{bulk}$.

$$q_t = q_{sur} + q_{bulk} \tag{5.4}$$

  Thus, the time derivative is given as follows:

$$\frac{\partial q_t}{\partial t} = \frac{\partial q_{sur}}{\partial t} + \frac{\partial q_{bulk}}{\partial t} \tag{5.5}$$

  with $q_{sur}$ as the $CO_2$ uptake at the surface and $q_b$ as the sorption in the bulk phase of the sorbent, respectively. Both terms represent ph-

ysisorption as well as chemisorption, but at different locations within the amine layer. We assume that the adsorption can be described as a reaction of higher order. Thus, the kinetic on the surface can be described using a fractional-order kinetic approach:

$$\frac{\partial q_{sur}}{\partial t} = k_{sur} \cdot (q_{eq} - q_t)^{n_{DKM}} \tag{5.6}$$

Furthermore, both chemi- and physiosorbed $CO_2$ molecules can further react with the non-surface active sites (also referred to as bulk amine layer). These interactions are then described by [Ebne2011]:

$$\frac{\partial q_{bulk}}{\partial t} = k_{bulk} \cdot q_t \cdot (q_{eq} - q_t)^{n_{DKM}} \tag{5.7}$$

The fractions of active sites at the surface and in the bulk phase are intrinsically incorporated into the kinetic parameters $k_{sur}$ and $k_{bulk}$. Combining equations (5.6) and (5.7), we get:

$$\frac{\partial q_t}{\partial t} = k_{sur} \cdot (q_{eq} - q_t)^{n_{DKM}} + k_{bulk} \cdot q_t \cdot (q_{eq} - q_t)^{n_{DKM}} \tag{5.8}$$

This can be rearranged to derive our dual kinetic model:

$$\frac{\partial q_t}{\partial t} = k_{DKM} \cdot (1 + \beta_{DKM} \cdot q_t) \cdot (q_{eq} - q_t)^{n_{DKM}} \tag{5.9}$$

with $k_{DKM}$ as constant for the dual kinetic model, $\beta_{DKM}$ as the ratio of $k_{bulk}$ and $k_{sur}$.

The fits of the models are evaluated by the normalized standard deviation ($NSD$):

$$NSD\ [\%] = \sqrt{\frac{\sum[(q_{t(exp)} - q_{t(mod)}/q_{t(exp)}]^2}{N-1}} \cdot 100 \tag{5.10}$$

In addition to a more comprehensive description of the physical behavior by the dual kinetic model, the mathematical fitting of the model's parameters to experimental data is improved through an additional model parameter compared with alternative models.

## 5.3 Results and discussion

To show the general usability of our dual kinetic model, we fitted the model parameters of several kinetic models to the experimental data of Serna-Guerrero et al. [Sern2010], who used amine-grafted mesoporous silica, and to the experimental data of Abdollahi-Govar et al. [Abdo2015], who used PEI-impregnated CARiACT G10 silica support. These experimental data sets represent the two main classes of amine-functionalized solid sorbents, namely amine-grafted and amine-impregnated materials. Furthermore, we fitted the model parameters to the adsorption behavior of amine-functionalized carbon nanotubes and metal-organic-frameworks. The results for these two materials are summarized in [Ohs2018a].

### 5.3.1 Comparison of kinetic models for amine-grafted solid sorbents

In Figure 5.1 the experimental data of Serna-Guerrero *et. al.* [Sern2010] are compared with the four kinetic models for 25 °C, 40 °C, 55 °C and 70 °C. Except of the kinetic first-order model, all other models can be fitted to the experimental data accurately. Yet, the best agreement for all temperatures is observed for the dual kinetic model.

Table 5.1 summarizes the values of the kinetic constants and the normalized standard deviation for the different models. Except for the pseudo-first-order model (Err between 12 and 21 %), the associated $NSD$ are very small. However, for both Avrami's model and the generalized fractional-order kinetic model, a severe problem exists: a systematic correlation of all kinetic rate constants and the temperature cannot always be observed [Sern2010]. In comparison, our model shows an exponential increase of the kinetic constant $k_{DKM}$ and an exponential decrease of the interaction parameter $\beta_{DKM}$ with the temperature, respectively. Thus, in an Arrhenius-plot a linear relation of the inverse temperature and the model parameters is observed (see Figure 5.2).

Thus, the temperature dependence of the kinetic constant can be written

**Table 5.1:** Kinetic model parameters for $CO_2$ adsorption on triamine-bearing organic species grafted on a mesoporous pore expanded MCM-41 silica at 5 vol-% $CO_2$ and the corresponding normalized standard deviation.

| Model | Variable | 25 °C | 40 °C | 55 °C | 70 °C |
|---|---|---|---|---|---|
| Pseudo-first-order model | $k$ [$10^{-2} \cdot \text{sec}^{-1}$] | 2.65 | 3.13 | 2.86 | 2.70 |
| | NSD [%] | 15 | 12 | 13 | 21 |
| Avrami's model | $k_A$ [$10^{-2} \cdot \text{sec}^{-n_A}$] | 6.81 | 6.34 | 5.35 | 7.62 |
| | $n_A$ [-] | 1.5 | 1.38 | 1.30 | 1.53 |
| | NSD [%] | 3.0 | 3.1 | 2.3 | 8.8 |
| Generalized fractional-order kinetic model | $k_G$ [$10^{-2} \cdot \text{sec}^{-m_G} \cdot \text{mmol}^{\,1-n_G} \cdot \text{g}^{n_G-1}$] | 0.95 | 1.72 | 2.29 | 1.38 |
| | $m_G$ [-] | 1.68 | 1.46 | 1.11 | 1.77 |
| | $n_G$ [-] | 1.70 | 1.33 | 1.32 | 2.34 |
| | NSD [%] | 3.5 | 3.6 | 10.2 | 3.4 |
| Dual kinetic model | $k_{DKM}$ [$10^{-2} \cdot \text{sec}^{-1} \cdot \text{mmol}^{1-n_{DKM}} \cdot \text{g}^{n_{DKM}-1}$] | 0.67 | 0.96 | 1.10 | 1.53 |
| | $\beta_{DKM}$ [$\text{g} \cdot \text{mmol}^{-1}$] | 9.32 | 6.13 | 5.41 | 5.00 |
| | $n_{DKM}$ [-] | 2 | 2 | 2 | 2 |
| | Err [%] | 3.1 | 3.1 | 3.4 | 10.0 |

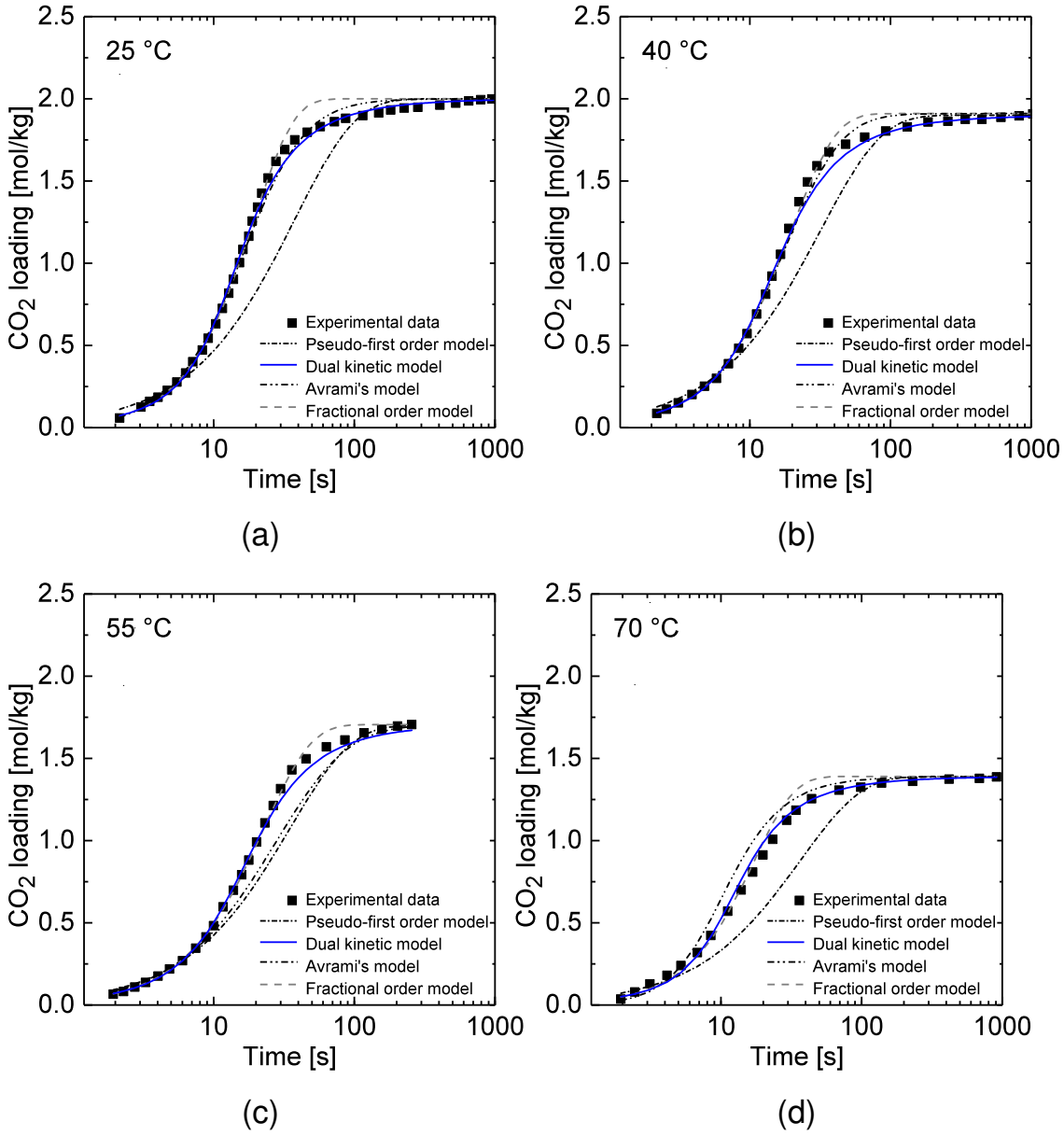


**Figure 5.1:** Comparison of experimental $CO_2$ uptake data and corresponding fit to kinetic models for triamine-bearing organic species grafted on a mesoporous MCM-41 silica at 5 vol-% $CO_2$. Experimental data were taken from [Sern2010].

as:

$$k_{DKM} = k_{DKM,0} \cdot e^{-\frac{E_{a,k_{DKM}}}{R \cdot T}} \quad , \tag{5.11}$$

$$k_{bulk} = k_{bulk,0} \cdot e^{-\frac{E_{a,k_{bulk}}}{R \cdot T}} \tag{5.12}$$

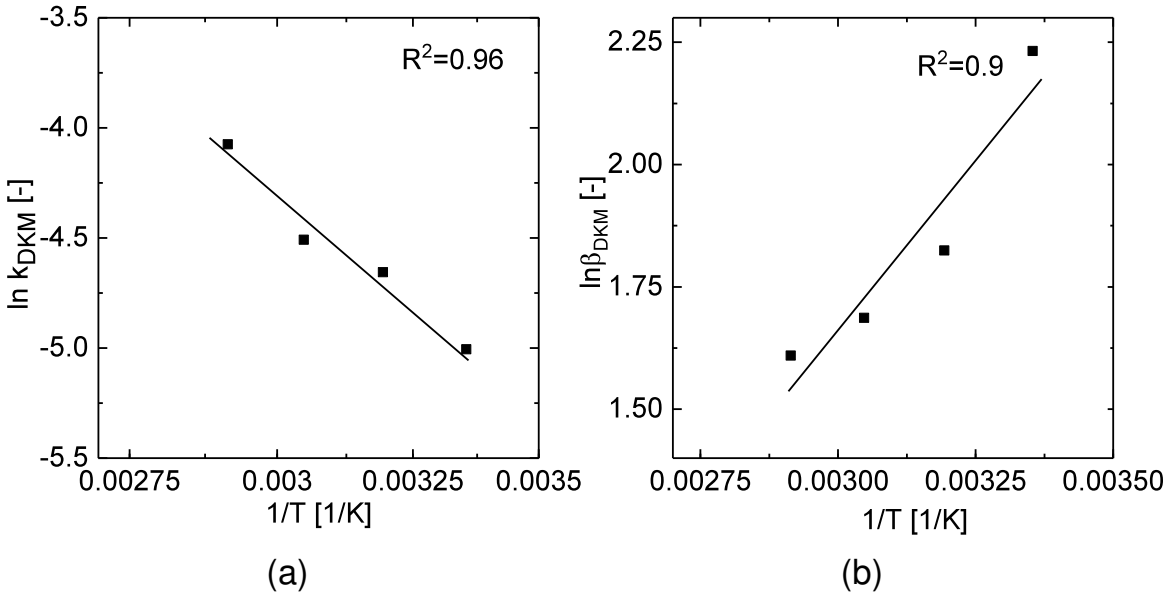


**Figure 5.2:** Arrhenius plots for the kinetic constants obtained by our dual kinetic model for triamine-bearing organic species grafted on a mesoporous pore expanded MCM-41 silica: (a) kinetic constant $k_{DKM}$ and (b) the adsorption site interaction parameter $\beta_{DKM}$.



and

$$\beta_{DKM} = \beta_{DKM,0} \cdot e^{-\frac{E_{a,\beta_{DKM}}}{R \cdot T}} \tag{5.13}$$

where $k_{DKM,0}$ and $\beta_{DKM}$ as the Arrhenius pre-exponential factors, $E_a$ as the activation energy, $R$ as the universal gas constant and $T$ as the absolute temperature.

We assume that $k_{DKM}$ increases with temperature due to a faster diffusion and/or higher chemisorption kinetics. Furthermore, the apparent activation energy for $\beta_{DKM}$ is negative. Negative activation energies for amine-functionalized materials have already been reported in the literature [Liu2014; Ebne2011; Mona2013], and are based on different temperature dependencies of forward and backward reactions. This, results in negative effective activation energies. However, the activation energy of the bulk adsorption parameter $k_{Bulk}$ is positive (see Table 5.2).

Compared with the other models, the exponential factor is temperature independent, meaning that the adsorption mechanism does not change

**Table 5.2:** Parameters for the Arrhenius equations for triamine-bearing organic species grafted on a mesoporous pore expanded MCM-41 silica.

| Parameter | Value | Unit |
|---|---|---|
| Pre-exponential factor $k_{DKM,0}$ | 5.414 | [1/s] |
| Activation energy $E_{a,k_{DKM}}$ | 16.616 | [kJ/mol] |
| Pre-exponential factor $k_{bulk,0}$ | 0.443 | [1/s] |
| Activation energy $E_{a,k_{bulk}}$ | 5.077 | [kJ/mol] |
| Pre-exponential factor $\beta_{DKM,0}$ | 0.082 | [1/s] |
| Activation energy $E_{a,\beta_{DKM,0}}$ | -11.539 | [kJ/mol] |

with temperature. This temperature independence of the exponential factor and the Arrhenius relation for the other kinetic constants are distinct advantages of the new proposed model since it allows to predict the relevant kinetic parameters for a broad range of temperatures.



### 5.3.2 Dual kinetic model for amine-impregnated solid sorbents

Amine-impregnated sorbents represent the second class of amine-functionalized sorbents. To show the universal usability of our model, we additionally fitted our dual kinetic model to experimental data from Abdollahi-Govar et al. [Abdo2015], who used PEI-impregnated CARiACT G10 silica support. The comparison of the experimental data and the kinetic models are shown in Figure 5.3. The parameters of our dual kinetic model can be fitted to the experimental data at different temperatures. As for the amine-grafted materials, the kinetic model parameters for the adsorption follow a linear correlation in the Arrhenius plot (see Figure 5.4).

Besides the adsorption step, the desorption step is of utmost importance for the design of temperature-swing adsorption processes, because (i) it is the main contributor to the total energy consumption, i.e. heating and/or vacuum and (ii) a complete regeneration usually takes much longer than the adsorption [Abdo2015]. Unfortunately, only very few studies addressing

desorption kinetics of amine-functionalized material have been published. Using Avrami's model the desorption of amine-functionalized materials can be described by the following equation [Liu2014]:

$$\Theta = 1 - exp(-(k_A \cdot t)^{n_A}) \tag{5.14}$$

Here, $\Theta$ represents the ratio of the current loading during desorption $q_{t,Des}$ and the loading at the end of the adsorption step $q_{t,Ads}$. However, the depressurization and/or heating usually accounts for a significant amount of time in real adsorption beds. Thus, it is debatable when to start the 'desorption time' $t$ as used in Equation 5.14 for Avrami's model and the generalized fractional-order kinetic model and whether the identified parameters are valid, if longer heating times are required. In our modified kinetic model, we circumvent this problem by describing the time derivative of the sorbent loading as a function of the current loading. In Figure 5.3 (b) the kinetic model is fitted to experimental desorption data: the model is capable to describe the desorption behavior accurately. However, the kinetic parameter $\beta_{DKM}$ have to be deduced for the desorption step separately. All kinetic parameters for the adsorption and desorption are summarized in Table 5.3 and Table 5.4.

Table 5.5 summarizes the kinetic constants for the amine-impregnated solid sorbents. As for the amine-grafted materials, the activation energy of the Arrhenius pre-exponential factor for the surface adsorption is positive (see Table 5.2). However, the activation energy for the bulk adsorption is negative (both $E_{a,\beta_{DKM}}$, as well as $E_{a,k_{bulk}}$). This indicates that with increasing temperature, less $CO_2$ is adsorbed which can further react with the amines in the bulk phase.

The dependence of the kinetic parameters on the $CO_2$ fraction in the gas phase is an additional challenge of Avrami's and the generalized fractional-order model [Abdo2015; Sern2010]. The kinetic parameters such as the kinetic constant $k_A$ depend significantly on the $CO_2$ fraction of the adsorption measurements. Thus experimental data are often acquired for different

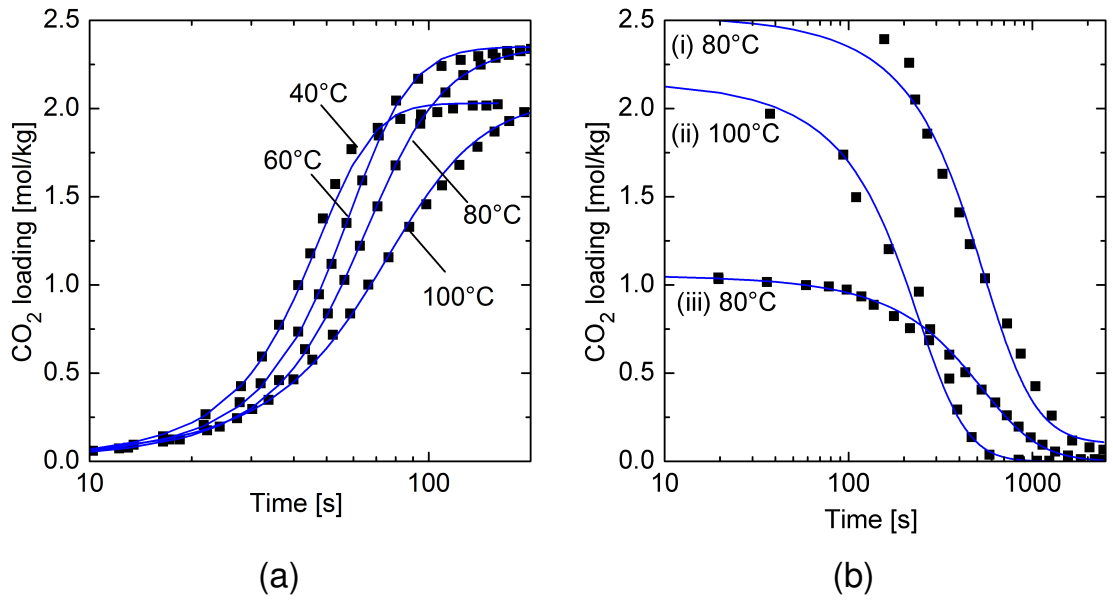


**Figure 5.3:** Comparison of experimental $CO_2$ uptake and desorption data and corresponding fit to the dual kinetic model for PEI-impregnated CARiACT G10 silica support. Experimental data were taken from [Abdo2015] and obtained for $CO_2$ adsorption with a $CO_2$ fraction of 32.8 %. (i)-(ii) represents different desorption temperatures and (iii) desorption starting from a lower loading of the sorbent.

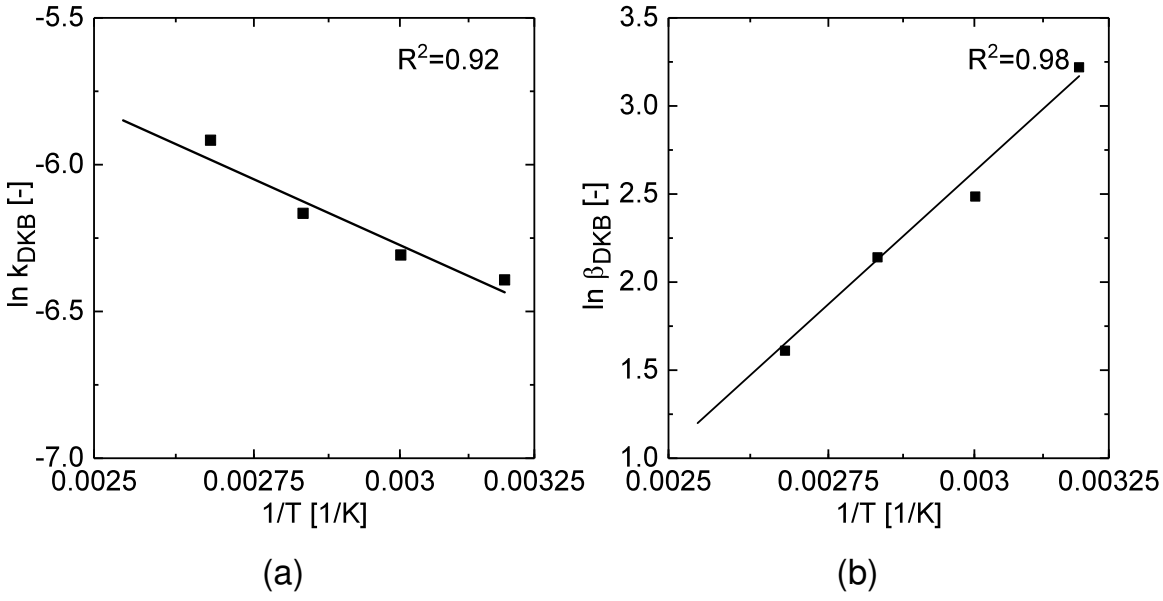


**Figure 5.4:** Arrhenius plots for the kinetic constants obtained by our dual kinetic model for for PEI-impregnated CARiACT G10 silica support: (a) kinetic constant $k_{DKM}$ and (b) the adsorption site interaction parameter $\beta_{DKM}$.

gas compositions and the models are then fitted to the experiments for each composition. However, the model parameters vary significantly with the gas

composition for this approach [Liu2014], in particular at low $CO_2$ fractions which are the most promising application of these materials. Sometimes a systematic relationship between the model parameters and the $CO_2$ fraction cannot be observed at all [Heyd2011b]. Thus, for these currently used models it is impossible to predict the adsorption kinetics for feed compositions which have not been investigated experimentally. To demonstrate the strength of the proposed model, we applied our model to a broad range of $CO_2$ gas phase fractions (see Figure 5.5). We used the experimental data of [Abdo2015], who measured the $CO_2$ uptake at different $CO_2$ gas fractions (1.2 %, 4.8 %, 14.5 % and 32.8 %). Figure 5.5 demonstrates convincingly that the model can describe the $CO_2$ uptake at different gas compositions with one parameter set. However, the fit is slightly better for higher adsorption temperatures. This independence of kinetic parameter of the gas composition provides an additional benefit of the proposed model since it can be used for process analysis with different feed compositions.



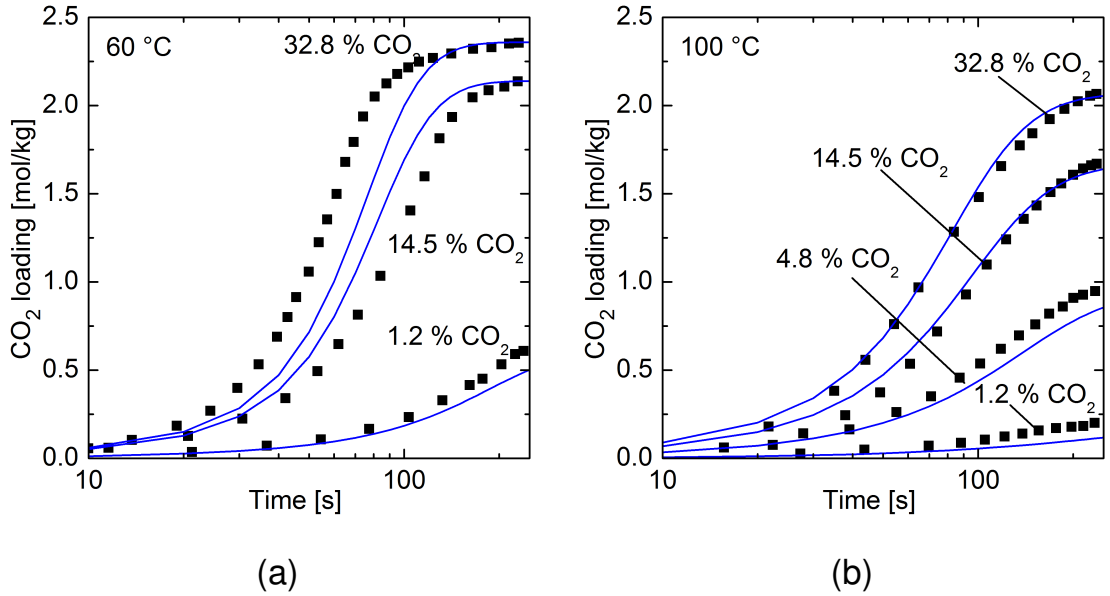


**Figure 5.5:** Comparison of experimental $CO_2$ uptake data and corresponding fit to the dual kinetic model for different $CO_2$ concentration for PEI-impregnated CARiACT G10 silica support. Experimental data were taken from [Abdo2015].

### 5.3.3 Simulation of breakthrough behavior

The proposed dual kinetic model can be easily incorporated into a dynamic temperature swing adsorption process model. As a case study for the practical application we simulated an adsorption bed for carbon dioxide capture from flue gas. The mass balance for the column bed is given by the following equation:

$$(\epsilon_{bed}+(1-\epsilon_{bed})\cdot\epsilon_p)\cdot\frac{\partial c_i}{\partial t}+\epsilon_{bed}\frac{\partial(u\cdot c_i)}{\partial z}+(1-\epsilon_{bed})\cdot\rho_p\cdot\frac{\partial q_i}{\partial t}=\epsilon_{bed}\cdot D_z\frac{\partial^2 c_i}{\partial^2 z} \quad (5.15)$$

where $\epsilon_{bed}$ is the bed void fraction, $u$ the interstitial velocity, $c_i$ the molar concentration of component $i$, $D_z$ is the axial dispersion coefficient, $\rho_p$ the particle density and $z$ the axial bed direction. $\epsilon_p$ represents the particle void fraction and $q_i$ is the amount of adsorbed $CO_2$. The adsorption isotherm for $CO_2$ is described by a Langmuir-type expression [Ebne2011]:

$$q_{CO_2}=\frac{k\cdot p_{CO_2}\cdot q_{max}}{1+k\cdot p_{CO_2}} \quad (5.16)$$

with $k$ as the affinity coefficient between $CO_2$ and the sorbent as well as $q_{max}$ as the maximal sorbent loading. The parameters used for the case study are given in Table 5.6.

In Figure 5.6 (a) the breakthrough curves resulting from simulations using both the pseudo first order and the dual kinetic model are compared with experimental adsorption data taken from [Sern2010]. Here, the absolute breakthrough time is shifted by an expected dead-volume time of the experimental set-up. The DKM can describe the sharp breakthrough behavior observed for amine-functionalized materials. Thus, we expect that the dual kinetic model is also able to describe the breakthrough behavior of amine-impregnated materials better than the linear driving force model.

In addition, we simulated an adsorption bed which is filled with amine-impregnated solid sorbents. The resulting breakthrough curves for different feed flow rates for both the pseudo-first-order and the dual kinetic model are

depicted in Figure 5.6 (b). In particular for short adsorption cycles, as used in modern rapid cycle temperature swing adsorption processes [Leta2014], the error for the breakthrough curves for the pseudo-first-order model is significantly large (e.g. at $C/C_{Feed}$= 0.1 the difference is 25%). In this case, designing a process by using the dual kinetic model allows increasing the loading of the adsorption bed. In comparison, process design with the PFO model would lead to incomplete loading. This would increase the amount of adsorption bed, which has to be heated up for regeneration. Since heating is the main contributor to the total energy consumption of TSA processes, a more precise model allows for significant energy reduction. Thus, for process evaluation a sophisticated kinetic model, as presented here, is indispensable.

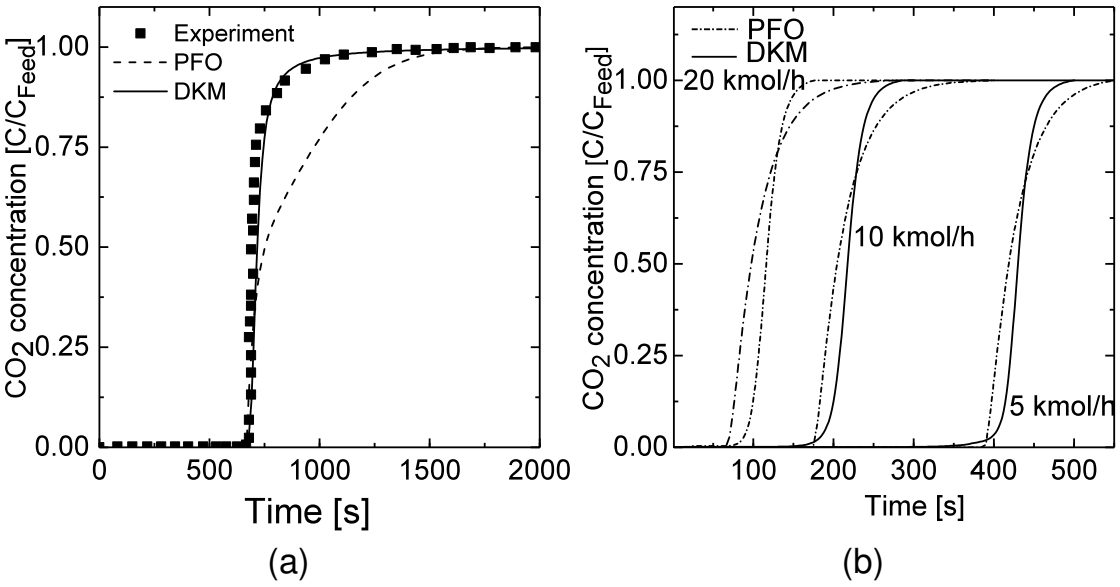


**Figure 5.6:** (a) Breakthrough simulation for amine-grafted mesoporous silica: Comparison with experimental data from [Sern2010] at a feed rate of 30 ml/min and (b) Breakthrough behavior of an process scale adsorption bed using PEI-impregnated CARiACT G10 silica support at different feed flow rates and a $CO_2$ molar fraction of 15 %. PFO represents the pseudo-first-order model and DKM the dual kinetic model.

**Table 5.3:** Kinetic model parameters for $CO_2$ adsorption for PEI-impregnated CARiACT G10 silica support at 32.8 % $CO_2$.

| Parameter | 40 °C | 60 °C | 80 °C | 100 °C |
|---|---|---|---|---|
| $k_{DKM}$ [$10^{-2} \cdot sec^{-1} \cdot mmol^{1-n_{DKM}} \cdot g^{n_{DKM}-1}$] | 0.17 | 0.18 | 0.21 | 0.27 |
| $\beta_{DKM}$ [$g \cdot mmol^{-1}$] | 25 | 12 | 8.5 | 5 |
| $n_{DKM}$ | 1.2 | 1.2 | 1.2 | 1.2 |

**Table 5.4:** Values of the kinetic model parameters for $CO_2$ desorption under pure nitrogen purge for PEI-impregnated CARiACT G10 silica support.

| Parameter | 80 °C | 100 °C |
|---|---|---|
| $k_{DKM}$ [$10^{-2} \cdot \text{sec}^{-1} \cdot \text{mmol}^{1-n_{DKM}} \cdot \text{g}^{n_{DKM}-1}$] | 4.5 | 1.03 |
| $\beta_{DKM}$ [$\text{g} \cdot \text{mmol}^{-1}$] | -0.35 | -0.40 |
| $n_A$ | 1.2 | 1.1 |



**Table 5.5:** Parameters for the Arrhenius equation for PEI-impregnated CARiACT G10 silica support.

| Parameter | Value | Unit |
|---|---|---|
| Pre-exponential factor $k_{DKM,0}$ | 2.86 | $10^{-2}$ [1/s] |
| Activation energy $E_{a,k_{DKM}}$ | 7.50 | [kJ/mol] |
| Pre-exponential factor $k_{bulk,0}$ | 4.35 | $10^{-5}$ [1/s] |
| Activation energy $E_{a,k_{bulk}}$ | -17.697 | [kJ/mol] |
| Pre-exponential factor $\beta_{DKM,0}$ | 1.49 | $10^{-3}$ [1/s] |
| Activation energy $E_{a,\beta_{DKM,0}}$ | -25.198 | [kJ/mol] |

**Table 5.6:** Parameters for breakthrough simulations in gProms for an adsorption bed at 20℃ and a $CO_2$ molar feed fraction of 15 %.

| Parameter | Value | Unit |
|---|---|---|
| Bed length $L$ | 1.2 | [m] |
| Bed diameter $d_{Bed}$ | 0.3 | [m] |
| Particle density $\rho_p$ | 880 | [kg $\cdot$ m$^{-3}$] |
| Particle diameter $d_p$ | 2.5 | [mm] |
| Kinetic constant $k_{DKM}$ | 1.3 | [10$^{-3}$ $\cdot$ sec$^{-1}$ $\cdot$ mmol$^{1-n_{DKM}}$ $\cdot$ g$^{n_{DKM}-1}$] |
| Adsorption site interaction parameter $\beta_{DKM}$ | 43 | [g $\cdot$ mmol$^{-1}$] |
| Adsortion order $n_{DKM}$ | 1.2 | [-] |
| Adsorption heat $\Delta H$ | 50 | [ kJ $\cdot$ mol$^{-1}$] |
| Maximal sorbent loading $q_{max}$ | 2.9 | [mol $\cdot$ kg$^{-1}$] |

## 5.4 Conclusion

This chapter presented an accurate but simple dual kinetic model (DKM) for the $CO_2$ uptake of functionalized solid sorbents under various conditions and temperatures. This model describes the $CO_2$ uptake as a function of a kinetic factor, the adsorption driving force as well as the current $CO_2$ loading. The model is suitable to describe the kinetics for several different amine-functionalized materials accurately. Furthermore, the fitted parameters are an exponential function of the temperature which allows predicting their values for a broad range of operation points. Additionally, the dual kinetic model can describe the $CO_2$ adsorption at different $CO_2$ gas fractions with one parameter set. The possibility to extra- and interpolate the kinetic data is a distinct benefit of the dual kinetic model in comparison to the kinetic models presented in the literature. Furthermore, it can be integrated into process simulation easily. Now, the accurate exploration of the impact of new solid sorbent materials in realistic process environments can proceed swiftly. Thus, in the subsequent chapter, a temperature swing adsorption process based on amine-functionalized material is presented.

# 6 Combining electrochemical hydrogen separation and temperature-vacuum swing adsorption for the separation of $N_2$, $H_2$ and $CO_2$



Parts of this chapter have been published as:

Burkhard Ohs, Lorenz Abduly, Maximilian Krödel, Matthias Wessling
*Combining electrochemical hydrogen separation and temperature-vacuum swing adsorption for the separation of $N_2$, $H_2$ and $CO_2$*, International Journal of Hydrogen Energy, 2020
DOI: 10.1016/j.ijhydene.2020.01.218

# 6.1 Introduction

Nitrogen sparging can reduce the inhibition of fermentation processes by $H_2$ and $CO_2$. However, the dilution of hydrogen makes the separation challenging. Recently, Massanet-Nicolau et al. presented an electrochemical process for hydrogen separation combined with amine scrubbing for $CO_2$ removal, which does not require the compression of the bulk stream. Furthermore, the electrochemical hydrogen separation (ECHS) only needs small overpotentials [Mass2016]. Because also $CO_2$ inhibits the biohydrogen fermentation [Mass2016], the efficient separation of $CO_2$ is an additional challenge. After $CO_2$ removal, $N_2$ can be recycled to the fermentation unit for sparging, which decreases $N_2$ consumption and thus overall costs. For $N_2$/$CO_2$ separation, such as flue gas carbon capture, adsorption-based processes have been investigated [DAle2010; Choi2009; Ntia2016]. The low energy consumption and the simple operation mode is also attractive for decentralized $H_2$ production.

This chapter combines the electrochemical hydrogen separation with a temperature-vacuum swing adsorption process (TVSA) for the first time. This design does not require pressurization of the gas bulk stream and is thus particularly attractive. So far, such a process has not been investigated. Interestingly, the process does not only recover high purity hydrogen but also produces $CO_2$ at high purities. This chapter gives first insights into potential process designs, energy duty and costs for this separation task.



# 6.2 Process description and modeling of the process units

## 6.2.1 Process overview

The fermentation unit produces a gas mixture consisting of $N_2$, $H_2$ and $CO_2$ (see Figure 6.1), which is first fed to the electrochemical hydrogen separation unit. The remaining gas stream ($N_2$ and $CO_2$) then enters the TVSA process for the removal of $CO_2$. The $N_2$ is then recycled to the fermentation

reactor for sparging and the $CO_2$ can be sold as a byproduct.

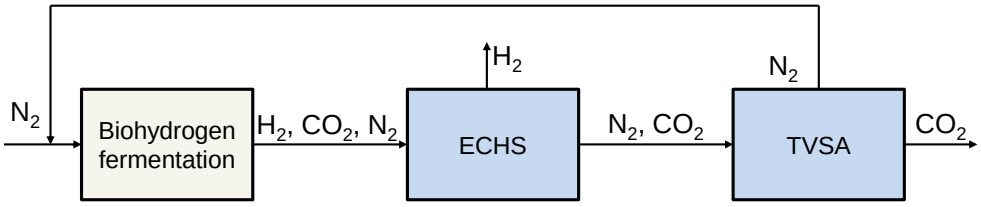


**Figure 6.1:** Flowsheet of the separation process consisting of an electrochemical hydrogen separation cell (ECHS) as well as a temperature-vacuum swing adsorption process (TVSA) for $CO_2$ removal.

### 6.2.2 Process units

### 6.2.3 Electrochemical hydrogen separation

The electrochemical hydrogen separation unit consists of two electrodes (see Figure 6.2), i.e. the anode and the cathode, as well as a proton exchange membrane (PEM). The feed enters the unit at the anode, where the hydrogen is split into protons. As the transport of protons through the PEM is significantly faster than the diffusive transport, purified hydrogen can be withdrawn at the cathode.

A simple 1-dimensional model describes the electrochemical separation unit with the following potential balance [Choi2004; Kugl2014]:

$$U_{Cell} = U_{Anode} + U_{Cathode} + U_{EP} + U_{Ohm} \tag{6.1}$$

with $U_{Cell}$ as the cell potential, $U_{Anode}$ and $U_{Cathode}$ as the anodic and cathodic overpotential, $U_{EP}$ as the equilibrium potential of the cell and $U_{Ohm}$ as the ohmic potential loss due to the proton transport through the PEM. The equilibrium potential can be calculated by adding the equilibrium potentials of the two electrodes [Wend2010]:

$$U_{EP} = E_A - E_C \tag{6.2}$$

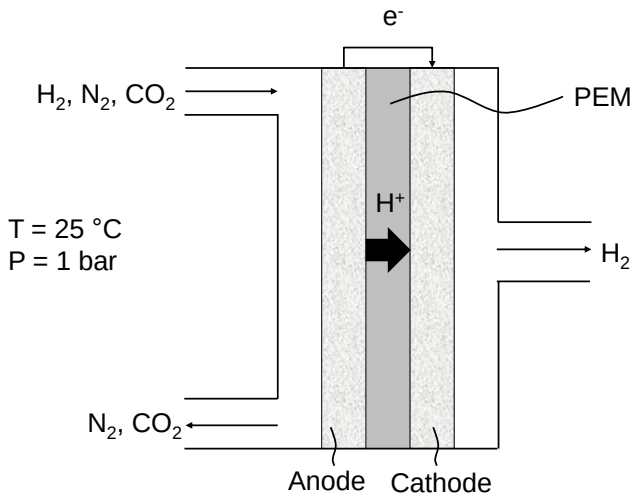


**Figure 6.2:** Schematic representation of the electrochemical hydrogen separation cell consisting of two electrodes as well as the proton exchange membrane (PEM).

with $E_A$ and $E_C$ as the equilibrium potentials of the anode and the cathode reactions. For ideal gas behavior and if the standard potentials for the anode and the cathode are equal (as for the hydrogen separation), the simplifies to [Wend2010]:

$$U_{EP} = \frac{R \cdot T}{\nu_e \cdot F} \cdot ln\,(\frac{c_{A,H_2}}{c_{C,H_2}}) \tag{6.3}$$

where $c_{A,H_2}$ and $c_{C,H_2}$ represent the hydrogen concentration at the anode and cathode. $\nu_e$ is the stoichiometric coefficient of the electrons in the half-cell reaction. The anodic and cathodic overpotentials are calculated by the Butler-Volmer equation [Wend2010]:

$$j_i = j_{0,i} \cdot e^{\frac{\alpha_i \cdot F \cdot U_i}{R \cdot T}} \tag{6.4}$$

here, $j$ represents the current density, $j_{0,i}$ the exchange current density and $\alpha_i$ the charge transfer coefficient. The mole balance for component $i$ at the

anode is then given by:

$$\dot{n}_{i,out} = \dot{n}_{i,in} - \dot{n}^{"}_{i,PEM} \cdot A_{ECHS} \tag{6.5}$$

with $\dot{n}_{i,in}$ as the inlet flow of component $i$ at the anode and $\dot{n}_{i,out}$ as the outflow of the anode, respectively. $n^{"}_{i,PEM}$ is the area specific number of molecules of component $i$ which are oxidized at the electrode (here only hydrogen) and $A_{ECHS}$ the geometric surface area of the electrode. $n^{"}_{i,PEM}$ can be calculated using Faraday's law, which correlates the number of oxidized molecules and the current exchange density $j$ for component $i$ (in this work only for hydrogen) [Wend2010]:

$$j_i = \frac{\nu_e \cdot F \cdot \dot{n}^{"}_{i,PEM}}{\nu_i} \tag{6.6}$$

$\nu_i$ is the stoichiometric coefficient for the component $i$ in the half-cell reaction. Equivalently, the outflow at the cathode can be calculated as follows (in this work only hydrogen):

$$\dot{n}_{i,PEM} = \dot{n}^{"}_{i,PEM} \cdot A_{ECHS} \tag{6.7}$$

Finally, the ohmic potential drop $\Delta U_{\Omega,E}$ due to charge transfer between the anode and the cathode is determined by the sum of the current densities $j$ ($j = \sum j_i$, as $H_2$ is the only electrochemical species considered in this work, only the current density for hydrogen must be considered), the thickness of the PEM $d_M$ and its conductivity $\kappa$ [Kugl2014]:

$$\Delta U_{\Omega,E} = \frac{j \cdot d_M}{\kappa} \tag{6.8}$$

The total power consumption $P_{Cell}$ is then given by multiplying the cell

voltage with the cell current $I$

$$P_{Cell} = U_{Cell} \cdot I \quad with \quad I = j \cdot A_{ECHS} \tag{6.9}$$

Dividing the total power consumption of the cell by the amount of separated hydrogen gives the specific energy consumption:

$$E_{spec} = \frac{P_{Cell}}{\dot{n}_{C,H_2}} \tag{6.10}$$

Finally, we calculated the energy efficiency as follows:

$$\eta_{ECHS} = 1 - \frac{P_{Cell}}{LHV_{H_2} \cdot \dot{n}_{C,H_2}} \tag{6.11}$$

with $LHV_{H_2}$ as the lower heating value of hydrogen. The physical parameters for the electrochemical hydrogen separation unit are summarized in Table 6.1



**Table 6.1:** Physical parameters for the electrochemical hydrogen splitter.

| Process parameter | Value | Unit | Reference |
|---|---|---|---|
| PEM conductivity $\kappa$ | 10 | A/(V · m$^2$) | Assumption |
| Charge transfer coefficient $\alpha_i$ | 0.5 | - | [Wend2010] |
| Faraday's constant $F$ | 96 485 | s · A / mol | [Wend2010] |
| Stoichiometric coefficient $\nu_{H_2}$ | 1 | - | [Wend2010] |
| Stoichiometric electron coefficient $\nu_e$ | 2 | - | [Wend2010] |
| PEM thickness $d_M$ | 0.2 | cm | Assumption |
| Exchange current density $j_0$ | 150 | A/m² | Assumption |

### 6.2.4 Temperature-vacuum swing adsorption process

In comparison to the electrochemical cell, the simulation of the TVSA unit is much more complex due to its dynamic operation mode. In this chapter, we simulate a three-step cycle consisting of an adsorption step at ambient conditions, a heating/vacuum step for desorption as well as a cooling step (see Figure 6.3). During the adsorption step, $N_2$ and $CO_2$ are fed to the adsorption column. The $CO_2$ is adsorbed and a pure $N_2$ stream is withdrawn from the adsorption column. Shortly before the $CO_2$-breakthrough, the adsorption step is terminated. Subsequently, the desorption step starts to regenerate the bed. During the heating step, the temperature of the column increases by heating of the column wall. Additionally, a vacuum is applied to enhance the regeneration of sorbent. When a specified regeneration is reached, the column is cooled down to restart the process cycle. In this chapter, we simulated a packed-bed column.

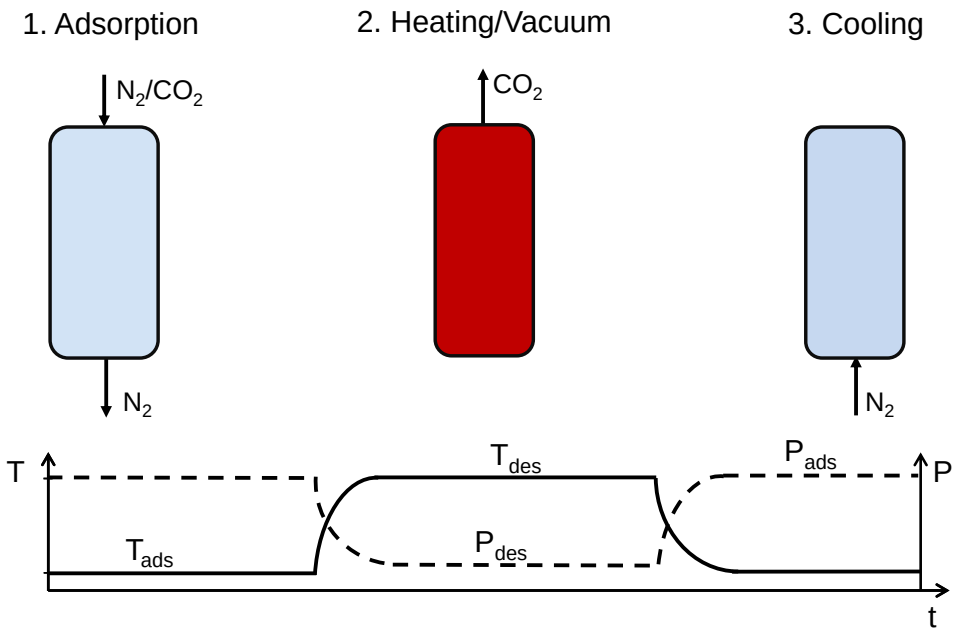


**Figure 6.3:** Three step TVSA cycle for $CO_2$ removal from the $N_2$ sparging stream.

We assumed the following simplifications for the simulation of the TVSA process:

- All gases obey the ideal gas law.

- Gradients in temperature, concentration and velocity in the radial direction are negligible.
- The flow within the packed-bed is one-dimensional, laminar and fully-developed.
- All adsorption particles are of uniform size and shape. Furthermore, they are evenly distributed in the adsorption bed.
- The humidity of the feed gas as well as trace components can be neglected.
- The amine functionalized material only adsorbs $CO_2$.
- The heat of adsorption is constant.

**Mass balance**

The mass balance of component $i$ in the packed-bed can be written in the following form [Ko2003]:



$$\frac{\partial C_i}{\partial t}(1+(1-\epsilon_{Bed})\cdot\frac{\epsilon_P}{\epsilon_{Bed}}) = D_{Ax}\frac{\partial^2 C_i}{\partial z^2} - \frac{\partial(v\cdot C_i)}{\partial z} - \frac{1-\epsilon_{Bed}}{\epsilon_{Bed}}\cdot\rho_P\cdot\frac{\partial q_i}{\partial t} \quad (6.12)$$

where $C_i$ is the molar concentration of component $i$, $\epsilon_{Bed}$ and $\epsilon_P$ are the bed and particle void fractions, respectively, and $D_{ax}$ the axial dispersion coefficient. $v$ represents the axial velocity, $\rho_P$ the sorbent particle density and $q_i$ the loading of the sorbent particle with component $i$. The axial dispersion term is small compared to the convective flow and thus can be neglected. Equivalently, the overall mass balance is given by the following equation [Ko2003]:

$$\frac{\partial C}{\partial t}(1+(1-\epsilon_{Bed})\cdot\frac{\epsilon_P}{\epsilon_{Bed}}) = -\frac{\partial(v\cdot C)}{\partial z} - \frac{1-\epsilon_{Bed}}{\epsilon_{Bed}}\cdot\rho_P\cdot\sum_{i=0}^{n}\frac{\partial q_i}{\partial t} \quad (6.13)$$

where $n$ is the number of components $i$ in the gas mixture.

### Adsorption kinetics

To describe the adsorption kinetics, we use a dual-adsorption kinetic model presented in Chapter 5, which can describe the $CO_2$ uptake precisely [Ohs2018a]:

$$\frac{\partial q_i}{\partial t} = k_L \cdot (1 + \beta_L \cdot q_i) \cdot (q_{eq} - q_i)^{n_L} \tag{6.14}$$

where $k_L$ is the kinetic constant for the unloaded sorbent of the loading-dependent kinetic model, $\beta_L$ the adsorption site interaction parameter and $n_L$ the macroscopic order of the adsorption mechanism.

### Adsorption isotherm

In this chapter, we simulated the $CO_2$ adsorption on PEI-impregnated CARiACT G10 silica support [Abdo2015]. The Langmuir model describes the adsorption isotherm of these materials:

$$q_e = \frac{k \cdot p_{CO_2} \cdot q_{Max}}{1 + k \cdot p_{CO_2}} \tag{6.15}$$



with $k$ as the Langmuir constant, $p_{CO_2}$ as the partial pressure of $CO_2$ and $q_{Max}$ as the total number of available adsorption sides. The temperature dependency of the Langmuir constant follows the Arrhenius approach:

$$k = k_0 \cdot e^{-\frac{E_{a,k}}{R \cdot T}} \tag{6.16}$$

here $k_0$ is the Arrhenius pre-exponential factor. $E_{A,k}$ represents the respective activation energy. Figure 6.4 shows the adsorption isotherms for 25 °C and 100 °C. The respective model parameters are summarized in Table 6.2. The adsorption takes place at 25 °C and a partial pressure of 0.15 bar. To make use of a reasonable working capacity, only increasing the temperature is not sufficient, because generating pure $CO_2$ would result

in a $CO_2$ pressure of 1 bar. Thus, also a vacuum must be applied. In this chapter, we analyze regeneration pressures in the range of 0.01 - 0.1 bar.

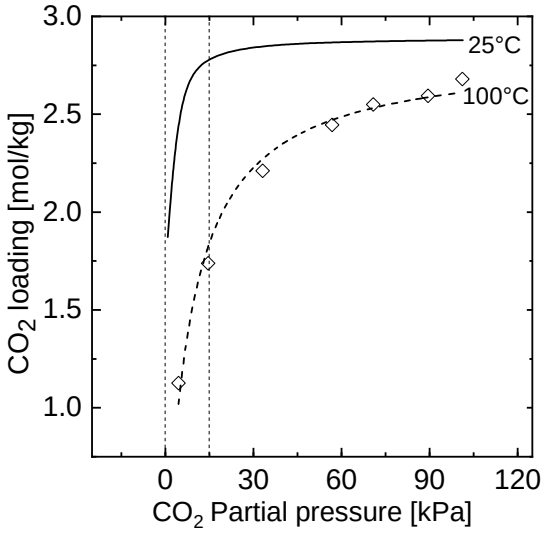


**Figure 6.4:** Adsorption isotherms for PEI-impregnated CARiACT G10 silica support at 25 °C and 100 °C [Abdo2015]. The isotherm at 100 °C was taken from [Abdo2015]. The adsorption isotherm at 25 °C was calculated using the Arrhenius approach.



**Table 6.2:** Physical parameters for the adsorption isotherm.

| Physical parameter | Value | Unit |
|---|---|---|
| Arrhenius pre-exponential $k_0$ | $1.07 \cdot 10^{-11}$ | [$bar^{-1}$] |
| Activation energy $E_{A,k}$ | 50.03 | [kJ/mol] |
| Maximal adsorption capacity $q_{Max}$ | 2.89 | [mol/kg] |

### Energy balance

For adsorption columns, the energy balance can be derived for the gas phase, adsorbent pellet, and column wall. Here, we use an integrated en-

ergy balance for the gas and solid phase of the adsorption column:

$$\begin{aligned} -\epsilon_{Bed} \cdot K_Z \cdot \frac{\partial^2 T}{\partial t^2} + \epsilon_{Bed} \cdot \rho_g \cdot c_{p,g} \cdot v \cdot \frac{\partial T}{\partial z} + \\ (\epsilon_{Bed} + (1 - \epsilon_{Bed} \cdot \epsilon_p) \cdot \rho \cdot c_{p,g} + \rho_{Bed} \cdot c_{p,s}) \cdot \frac{\partial T}{\partial t} + \\ (1 - \epsilon_{Bed}) \cdot \rho_p \cdot \frac{\partial q_{CO_2}}{\partial t} \cdot \Delta H_{Ads,CO_2} + h_{Wall} \cdot a_{Int} \cdot (T - T_{Wall}) = 0 \end{aligned} \tag{6.17}$$

with $K_Z$ as the axial thermal dispersion coefficient, $\rho_g$ and $\rho_p$ as the density of the gas and solid phase, $c_{p,g}$ and $c_{p,s}$ as the heat capacity of the gas and solid phase, $\Delta H_{Ads,CO_2}$ as the heat of adsorption, $h_{Wall}$ as the heat coefficient and $a_{Int}$ as the volumetric surface area of the adsorption bed.

### Pressure loss

Since large volume streams flow through the adsorption bed, the pressure loss is not neglectable and can be described by the well-known Darcy-equation [Amir2011]:

$$\frac{\partial p}{\partial z} = f_D \cdot \frac{\rho_g}{2} \cdot \frac{v^2}{d_H} \tag{6.18}$$

where $\rho_g$ is the gas density, $d_H$ is the hydraulic diameter of the channel and $f_D$ is Darcy's friction factor. For the friction factor, we assumed laminar flow.

### Boundary conditions

Additionally, boundary conditions are required to describe the adsorption process fully. We specified the boundary conditions for each cycle steps at the inlet and the outlet of the adsorption bed in Table 6.3. The $CO_2$ purity $y_{Product,CO_2}$ is given by the following equation:

$$y_{Product,CO_2} = \frac{\int_{t_{ads}}^{t_{ads}+t_{des/heat}} \dot{n}_{CO_2}|_{z=0}\, dt}{\int_{t_{ads}}^{t_{ads}+t_{des/heat}} \dot{n}|_{z=0}\, dt} \tag{6.19}$$

**Table 6.3:** Boundary conditions for the adsorption, heating/desorption and cooling step.

| Adsorption | Heating/Desorption | Cooling |
|---|---|---|
| $y_i(0) = y_i^{Feed}$ | $\frac{\partial y_i(0)}{\partial z} = 0$ | $\frac{\partial y_i(0)}{\partial z} = 0$ |
| $\frac{\partial y_i(L)}{\partial z} = 0$ | $\frac{\partial y_i(L)}{\partial z} = 0$ | $y_i(L) = y_i^{Recycle}$ |
| $v(0) = v^{Feed}$ | $\frac{\partial v(L)}{\partial z} = 0$ | $v(0) = 0$ |
| $\frac{\partial v(L)}{\partial z} = 0$ | $v(L) = 0$ | $\frac{\partial v(L)}{\partial z} = 0$ |
| $T(0) = T^{Feed}$ | $\frac{\partial T(0)}{\partial z} = 0$ | $\frac{\partial T(0)}{\partial z} = 0$ |
| $\frac{\partial T(L)}{\partial z} = 0$ | $\frac{\partial T(L)}{\partial z} = 0$ | $\frac{\partial T(L)}{\partial z} = 0$ |
| $\frac{\partial p(0)}{\partial z} = 0$ | $P(0) = P^{Vac}$ | $\frac{\partial p(0)}{\partial z} = 0$ |
| $P(L) = P^U$ | $\frac{\partial P(L)}{\partial z} = 0$ | $P(L) = P^U$ |

with $t_{ads}$ and $t_{des/heat}$ as the time for the adsorption and heating/desorption step, respectively. $\dot{n}_{CO_2}|_{z=0}$ and $\dot{n}|_{z=0}$ denote the $CO_2$ and total gas outflow of the adsorption column during the desorption step. Equivalently, the purity of $N_2$ $y_{Recycle,N_2}$ can be calculated:

$$y_{Recycle,N_2} = \frac{\int_0^{t_{ads}} \dot{n}_{N_2}|_{z=L}\, dt}{\int_0^{t_{ads}} \dot{n}|_{z=L}\, dt} \tag{6.20}$$

In this chapter, the adsorption step terminates at the breakthrough of the adsorption bed, i.e. if the following condition is met at the bed outlet:

$$y_{N_2} \leq 0.99 \tag{6.21}$$

Furthermore, the $N_2$ recovery is given by:

$$R_{N_2} = 1 - \frac{\int_{t_{ads}}^{t_{ads}+t_{des/heat}} \dot{n}_{N_2}|_{z=0}\, dt}{\int_0^{t_{ads}} \dot{n}_{N_2}|_{z=0}\, dt + \int_{t_{ads}+t_{des/heat}}^{t_{ads}+t_{des/heat}+t_{cool}} \dot{n}_{N_2}|_{z=0}\, dt} \tag{6.22}$$

The desorption step is stopped when a specific regeneration of the adsorption bed as defined in the sensitivity study is reached. In this chapter, we investigated a regeneration rate $\xi$ between 0.1 and 0.9 defined as follows:

$$\xi = 1 - \frac{q_{m,des}}{q_{m,ads}} \tag{6.23}$$

with $q_{m,ads}$ and $q_{m,des}$ as the mean bed loading at the end of the adsorption step and the desorption step, respectively.

### Energy efficiency

The minimum energy requirement is used to evaluate the energy efficiency of the TVSA-based $CO_2$ removal process [Kulk2012]. It is calculated as follows:

$$MER = \frac{\Delta E_{Tot}}{\Delta m_{CO_2}} \tag{6.24}$$

with $\Delta E_{Tot}$ as the total energy requirement per cycle, and the $\Delta m_{CO_2}$ as the total amount of $CO_2$ separated per cycle. The total energy requirement $\Delta E_{Tot}$ is the sum of the minimum heat duty for regeneration $Q_{Heat}$, the minimum energy duty for the gas flow during adsorption $E_{Gasflow}$ and the energy duty for vacuum generation $E_{Vacuum}$:

$$\Delta E_{Tot} = \Delta Q_{Heat} + \Delta E_{Gasflow} + \Delta E_{Vacuum} \tag{6.25}$$

The minimum heat duty comprises the heat duty for the adsorption bed, the desorption enthalpy as well as the heating of the column wall.:

$$\Delta Q_{Heat} = \Delta Q_{Bed} + \Delta Q_{Desorption} + \Delta Q_{Wall} \tag{6.26}$$

Here, we assumed that the heat capacities for all materials are constant in the given temperature range. The minimum energy duty for the gas flow is calculated as the product of the volumetric flow rate and the pressure drop inside the adsorption bed:

$$\Delta E_{Gasflow} = \int_{t_{Cycle}}^{t_{Cycle}+t_{Ads}} v_{Feed} \cdot A_{Column} \cdot \epsilon_{Bed} \cdot (p_{In} - p_{Out}) \ dt \tag{6.27}$$

where $A_{Column}$ is the cross-section of the column as well as $p_{In}$ and $p_{Out}$ the pressures at the inlet and the outlet of the column, respectively.

During the desorption step, the vacuum pump evacuates the adsorption bed and compress the gas to ambient conditions. Assuming an isothermal and irreversible process, the energy requirement for this step can be calculated with the following equation [Kulk2012]:

$$\Delta E_{Evacuation} = -p_{Atm} \cdot V_{Bed} \cdot (1 - \frac{p_{Des}}{p_{Atm}} + ln(\frac{p_{Des}}{p_{Atm}})) \tag{6.28}$$

where $p_{Atm}$ is the atmospheric pressure, $V_{Bed}$ the void volume of the adsorption bed and $p_{Des}$ the desorption pressure. Subsequently, the desorbed $CO_2$ is sucked out of the column. To calculate the energy requirement for this step, we assume that the withdrawn product must overcome the pressure drop in the adsorption bed and is isothermally compressed to ambient conditions by the vacuum pump [Kulk2012]:

$$\begin{aligned} &\Delta E_{Vacuumflow} = \\ &\int_{t_{Ads}}^{t_{Ads}+t_{Des}} (0.5 \cdot v_L \cdot A_{Column} \cdot \epsilon_{Bed} \cdot (p_{Atm} - p_{Des}) \\ &- \dot{n}_{CO_2} \cdot R \cdot T_{Des} \cdot ln(\frac{p_{Des}}{p_{Atm}})) \ dt \end{aligned} \tag{6.29}$$

where $v_L$ is the velocity at the outlet of the column and $\dot{n}_{CO_2}$ is the molar flow of $CO_2$ leaving the column during the desorption step. Thus the energy

for the vacuum $\Delta E_{Vacuum}$ is given by:

$$\Delta E_{Vacuum} = \Delta E_{Evacuation} + \Delta E_{Vacuumflow} \tag{6.30}$$

The total energy requirement of the adsorption column is calculated by dividing the minimal energy requirements by the efficiencies of the different process units as summarized in Table 6.4.

**Table 6.4:** Energy efficiencies for the process equipment used for TVSA processes

| Efficiency | Value | Reference |
|---|---|---|
| Fan | 0.8 | Assumption |
| Heat exchanger | 0.85 | [Kulk2012] |
| Vacuum pump | 0.7 | [Wurz2011] |

### 6.2.5 Separation costs

Besides the energy duties, the recovery and the purities of the two separation steps, we consider the process costs as an additional process criterion. As the process operates for several years, we evaluate the equivalent annual costs $EAC$:

$$EAC = C + \frac{I_{Tot}}{A_{t_{Plant},r}} \tag{6.31}$$

with $C$ as the annual operation costs, $I_{Tot}$ as the investment costs, $t_{Plant}$ as the plant lifetime and $A_{t_{Plant},r}$ as the annuity factor:

$$A_{t_{Plant},r} = \frac{1 - \frac{1}{(1+i)^{t_{Plant}}}}{i} \tag{6.32}$$

The specific costs $c_{Spec}$ are then calculated by dividing the $EAC$ by the hydrogen product stream $\dot{m}_{H_2,Prod}$ and the annual operation time $t_{Ope}$ as

follows:

$$c_{Spec} = \frac{EAC}{\dot{m}_{Prod} \cdot t_{Ope}} \tag{6.33}$$

The total investment costs are given by:

$$I_{Tot} = I_{ECHS} + I_{Ads} + I_{Fan} + I_{Vacuum} \tag{6.34}$$

with $I_{ECHS}$, $I_{Ads}$, $I_{Fan}$ and $I_{Vacuum}$ as investment costs for the ECHS, the adsorber column, the fans and the vacuum pump, respectively. The investment costs for the ECHS are calculated by multiplying the stack surface area $A_{ECHS}$ with the specific stack price $p_{ECHS}$:

$$I_{ECHS} = A_{ECHS} \cdot p_{ECHS} \tag{6.35}$$

Here, we assume that the investment costs for the fan and vacuum pump scale linearly with the power duty:

$$I_{Fan,i} = P_{Fan,i} \cdot p_{Fan} \tag{6.36}$$

and

$$I_{Vacuum} = P_{Vacuum} \cdot p_{Vacuum} \tag{6.37}$$

The investment costs of the TVSA unit, $I_{TVSA}$, are calculated by adding the costs for the pressure vessels $I_{Vessel}$ to the costs of the adsorber material $I_{Adosrbent}$:

$$I_{TVSA} = (I_{Vessel} + I_{Adsorbent}) \cdot n_{PSA} \tag{6.38}$$

with $n_{PSA}$ as the number of adsorber beds. The costs for the pressure vessels are calculated by the Guthrie method [Bieg1997]:

$$I_{Vessel} = UF \cdot BC \cdot (MPF + MF - 1) \tag{6.39}$$

with $UF$ as the update factor, $BC$ the base costs, $MPF$ as the material and pressure correction and $MF$ as the module factor. The base costs are calculated as follows:

$$BC = C_0 \cdot (\frac{L}{L_0})^w \cdot (\frac{D}{D_0})^e \tag{6.40}$$

Here, $w$ denotes the length exponent and $e$ the diameter exponent. $L_0$ and $D_0$ are the reference lengths according to the Guthrie method [Bieg1997]. The investment costs of the adsorbent material are calculated as follows:

$$I_{Adsorbent} = V_{Adsorber} \cdot (1 - \epsilon_{Bed}) \cdot \rho_{Sorbent} \cdot C_{Ads} \tag{6.41}$$

with $V_{Adsorber}$ as the volume of the adsorption columns, $\epsilon_{Bed}$ as the bed void fraction and $\rho_{Sorbent}$ as the adsorbent density. The operating costs are calculated by the summation of the energy costs for the TVSA unit $C_{TVSA}$ and the electrochemical hydrogen separator $C_{ECHS}$:

$$C = C_{TVSA} + C_{ECHS} \tag{6.42}$$

For the ECHS unit the operational costs are given by the energy consumption with $P_{ECHS}$:

$$C_{ECHS} = p_{Energy} \cdot t_a \cdot P_{ECHR} \tag{6.43}$$

with $p_{energy}$ as the energy price, $t_a$ as the annual operation time. The

operational costs for the TVSA process itself are the sum of the power costs for the fan $C_{Fan}$, the vacuum pump $C_{Vac}$ and the heating $C_{Heating}$:

$$C_{TVSA} = C_{Vac} + C_{Fan} + C_{Heating} \tag{6.44}$$

The energy costs are calculated by multiplying the vacuum power duty $P_{Vac}$:

$$C_{VAC} = P_{Vac} \cdot p_{Energy} \quad , \tag{6.45}$$

the fan power duty $P_{Fan}$

$$C_{Fan} = P_{Fan} \cdot p_{Energy} \tag{6.46}$$

and the heating duty $P_{Heating}$

$$C_{Heating} = P_{Heating} \cdot p_{Energy} \tag{6.47}$$

with the energy price $p_{Energy}$, respectively.

## 6.3 Case study

For the fermentative biohydrogen production, various feedstocks as well as microorganisms can be used. Design parameters such as nutrient concentration or sparging rate, significantly influence the hydrogen concentration in the product gas [Bhar2016; Kapd2006]. Thus, the gas composition can vary significantly. For instance, [Krae2008] investigated the influence of different $N_2$ sparging rates on biohydrogen production. They have shown that sparging rates beyond 40 ml of nitrogen per min and liter of the liquid phase do not increase the hydrogen yield and the production rate. This results in

a $H_2$ and $CO_2$ gas fraction of approximately 18 % and 12 %, respectively. Thus, we adopt this feed composition in this chapter. Furthermore, we consider a feed stream volume of 150 $Nm^3/h$ which is in the size of conventional biogas plants [Scho2013a; Ohs2018b]. The ECHS stack price for the reference case is 140 €/$m^2$ [Bern2014]. The compressor and vacuum pump investment costs are assumed to be dependent on the installed power duty. For simplicity reasons, we assumed a linear correlation with 6.5 k€/kW. The energy price is 0.08 €/kWh for the reference costs. Further economic parameters can be found in Table 6.5.

**Table 6.5:** Process and economic parameters for the biohydrogen upgrading.

| Case study parameters | Value | Unit |
|---|---|---|
| Feed rate $\dot{V}_{Feed}$ | 150 | $Nm^3/h$ |
| Raw gas pressure $p_{Feed}$ | 1 | bar |
| $H_2$ feed fraction $y_{Feed,H_2}$ | 12 | mol-% |
| $CO_2$ feed fraction $y_{Feed,CO_2}$ | 18 | mol-% |
| $N_2$ purity $y_{Recycle,N_2}$ | $\geq$ 99 | % |
| Vacuum pump efficiency $\eta_{Vac}$ | 0.72 | - |
| ECHS stack price $p_{ECHS}$ | 140 | €/$m^2$ |
| Adsorber material price $p_{Sorbent}$ | 3 | €/kg |
| Adsorber material lifetime $t_{Sorbent}$ | 4 | a |
| Compressor and vacuum investment price $p_{Com}$ | 6.5 | k€/kW |
| Energy price $p_{Energy}$ | 0.08 | €/kWh |
| $H_2$ price $p_{H2}$ | 5 | €/kg |
| Annual operation hours $t_a$ | 8000 | h/a |
| Plant lifetime $t_{Plant}$ | 15 | a |
| Interest rate $r$ | 9 | % |

## 6.4 Results and discussion

First, we show the principle behavior and costs for different operation points of the electrochemical hydrogen separation unit. Subsequently, we present a sensitivity study for the design of the TVSA by varying the desorption pressure and temperature as well as the regeneration of the adsorption column. Finally, we compare the results for an overall process evaluation.

### 6.4.1 Electrochemical hydrogen splitter

The model can simulate the experimental data of [Gard2007] precisely. Figure 6.5 shows the potential drops within the electrochemical hydrogen separation unit for different current densities and a hydrogen recovery of 99.9 %. As well known for electrochemical systems, the overpotentials and the potential loss due to the ohmic resistance of the PEM increases at higher current densities. At current densities above 7500 A/m$^2$, the ohmic resistance is the main contributor to the cell potential.



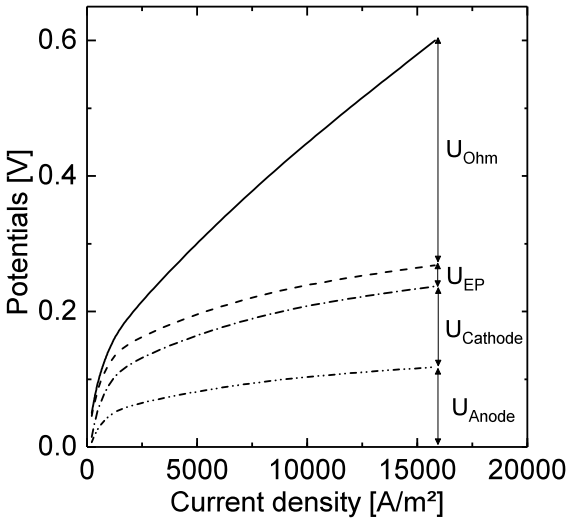


**Figure 6.5:** Influence of the current density on the potential losses in the electrochemical hydrogen separation cell

According to equation (6.9), the power consumption increases with total current and cell potential. At a fixed recovery and volume stream, the total current is constant according to the Faraday's law and thus the power

consumption is only a function of the cell potential. Thus, at increased cell potential, the energetic efficiency decreases (see Figure 6.6). At a cell potential of 0.05 V and 0.6 V, the energetic efficiency is about 96 % and 52 %, respectively. On the other hand, the specific throughput, defined as the amount of separated $H_2$ per time and stack area, rises from 0.008 kg/h/m$^2$ to 0.590 kg/h/m$^2$ with an increase of cell voltage from 0.05 V to 0.6 V. Thus, a trade-off between energy and investment costs exists.

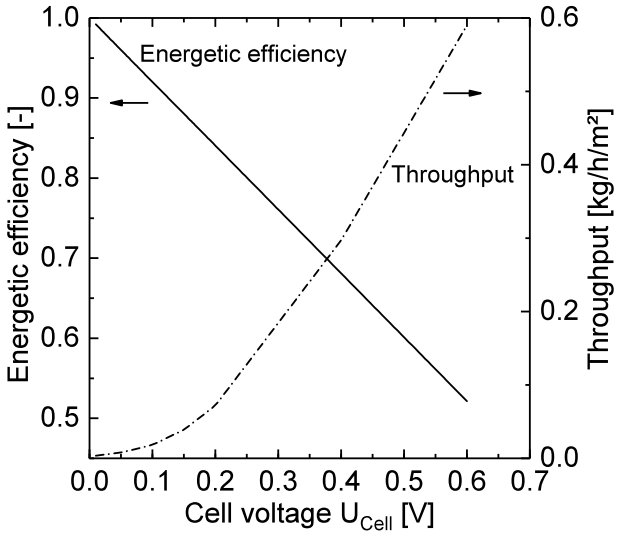


**Figure 6.6:** Influence of the cell potential on the energetic efficiency and the area-specific throughput at a hydrogen recovery of 99.9 %



To balance this trade-off, we calculated the specific separation costs defined by equation (6.33). Figure 6.7 shows the total specific $H_2$ separation costs for different cell potentials as well as electricity and stack prices. Depending on the electricity price, the optimal cell potential lays in the range of 0.1 and 0.15 V. The specific separation costs are 0.33 €/kg for an ECHS stack price of 140 €/m$^2_{Stack}$. Higher ECHS stack prices of 180 €/kg increase the specific separation costs to 0.38 €/kg. Even higher prices would move the optimal cell potential to higher values than 0.1 V.

## 6.4.2 Temperature-vacuum swing adsorption

In the following, we present a simulation study of the TVSA process. After the removal of the $H_2$ fraction, the resulting molar feed fractions of the TVSA

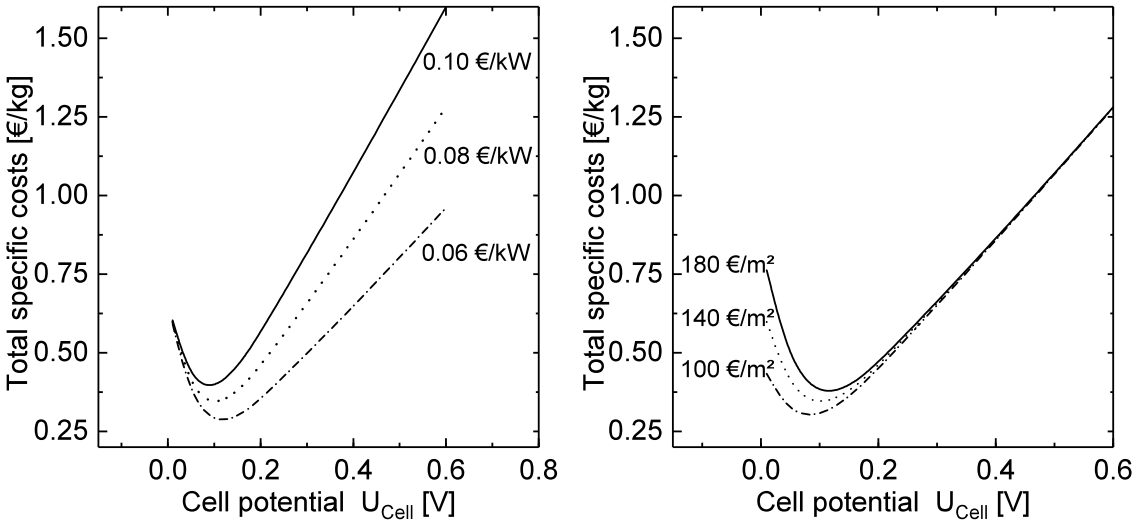


**Figure 6.7:** Total specific costs for different cell potentials $U_{Cell}$ and (a) electricity prices and (b) ECHS stack prices. The $H_2$ feed fraction is 18 % and the recovery is 99.9 %.

process are 15 % for $CO_2$ and 85 % for $N_2$, respectively. We varied the desorption pressure in the range of 0.01-0.1 bar, which we consider as a technically feasible vacuum range. The purity of $N_2$ for each simulation is 99 %.

6

Figure 6.8 shows the minimal energy requirement of the TVSA process for different desorption pressures and temperatures. The most energy efficient process operates at desorption pressure and temperature of 0.01 bar and 80 °C, respectively, as well as a regeneration rate of 0.7. At this operation point, the TVSA process consumes 0.68 kJ/kg$_{CO_2}$. At lower regeneration rates, the energy efficiency decreases as the adsorption bed is still partly loaded resulting in shorter adsorption steps. Thus, the energy consumption to heat the bed more frequently is much higher. Higher regeneration rates than 0.7 are not possible for desorption temperatures of 80 °C, as the working capacity of the sorbent is reached. With an energy consumption of 0.69 kJ/kg$_{CO_2}$, a process with a desorption pressure of 0.025 bar is almost equally energy efficient. For higher desorption rates, the process efficiency does only vary slightly with the desorption pressure, but higher desorption pressures limit the possible regeneration rate. In comparison,

processes with a desorption temperature of 100 °C allow higher regeneration rates. For this desorption temperature, the most energy efficient process operates at a desorption pressure of 0.025 bar and a regeneration rate at 0.7 (0.73 kJ/kg$_{CO_2}$). A process with a desorption pressure of 0.05 bar and a regeneration rate of 0.6 is only slightly less energy efficient and consumes 0.75 kJ/kg$_{CO_2}$. Higher desorption temperatures increase the MER further. At a desorption temperature of 120 °C, 0.79 kJ/kg$_{CO_2}$ are required for the process at a desorption pressure of 0.05 bar and a regeneration rate of 0.7. Thus, the minimal energy requirement:

- increases with higher desorption temperatures.
- decreases with high regeneration rates.

Besides the MER, the $CO_2$ purity, which also correlates with the recovery of $N_2$, is an important criterion for the process. An incomplete $N_2$ recovery results in additional costs as purged $N_2$ must be replaced. Furthermore, the co-produced $CO_2$ is of lower value. As shown in Figure 6.9, the $CO_2$ purity rises with increasing desorption temperature and decreasing desorption pressure. At low pressures and higher temperatures, more $CO_2$ is desorbed which increases the purity. Also, the recovery of $N_2$ increases, because more $CO_2$ is desorbed at high desorption rate and thus the cycle time for the adsorption step is increased which reduces the desorption frequency where $N_2$ is purged out with the $CO_2$ stream. The highest purity of 98.6 % was achieved at a temperature of 120 °C and a desorption pressure of 0.01 bar. Also, at higher desorption pressures and lower temperatures, $CO_2$ at purities beyond 95 % can be withdrawn. At lower regeneration rates than 0.4, the purity drops sharply, as low regeneration rates result in shorter process cycles and thus the rate of desorbed $CO_2$ compared to the $N_2$ present in the gas phase is much lower.

Furthermore, the volumetric throughput, i.e. the amount of purified $N_2$ per volume of the adsorption bed and cycle time, is another important process criterion as it is related to the investment costs for the sorbent material and adsorption bed. As shown in Figure 6.10, an optimum for the throughput for the different desorption pressures exists. At high regeneration rates,

the regeneration takes very long resulting in a low throughput. Also, low regeneration rates lead to short process cycles and thus to more frequent cooling and heating of the adsorption bed, which respectively decreases the throughput. The highest throughput of 79 $Nm^3/ (m^3_{Bed} h)$ is achieved at a desorption pressure and temperature of 0.01 and 100 °C, at a regeneration rate of 0.6. At lower desorption temperatures, the breakthrough time is reduced due to a lowered cycle capacity, i.e. the difference between adsorption and desorption loading, which also requires more frequent switching between the cycle steps. At higher desorption temperatures, the throughput is also lower as more time is needed for heating during the desorption step and cooling for the final cycle step, respectively. Thus, for the throughput

- an optimal regeneration rate exists,
- a median temperature is optimal as the working capacity of the bed and the time needed for the regeneration rate is well balanced,
- a low desorption pressure is beneficial.



The trade-off between energy requirement and throughput of the TVSA process results in an optimum for the specific purification costs of the process. Figure 6.11 shows the dependency of the specific purification costs (costs per $kg_{H_2}$ of the initial feed stream). For a desorption temperature of 100 °C, a process at 0.01 bar and a regeneration rate of 0.4 results in costs of 2.32 € per kg hydrogen. In comparison, the optimal desorption pressure for a process with a desorption temperature of 100 °C is 0.025 bar. At these operation parameters and a regeneration rate of 0.5, the specific purification costs are 2.30 € per kg hydrogen, which are the lowest costs for all processes investigated. Finally, the costs for the optimal process a desorption temperature of 120 °C are slightly higher (2.37 € per kg hydrogen). With these results, it can be concluded that:

- the MER is not a sufficient process criterion, as also the volumetric throughput significantly influences the overall process costs.

- the regeneration rate and thus the volumetric throughput is more important for this TVSA processes than the desorption temperature and pressure,

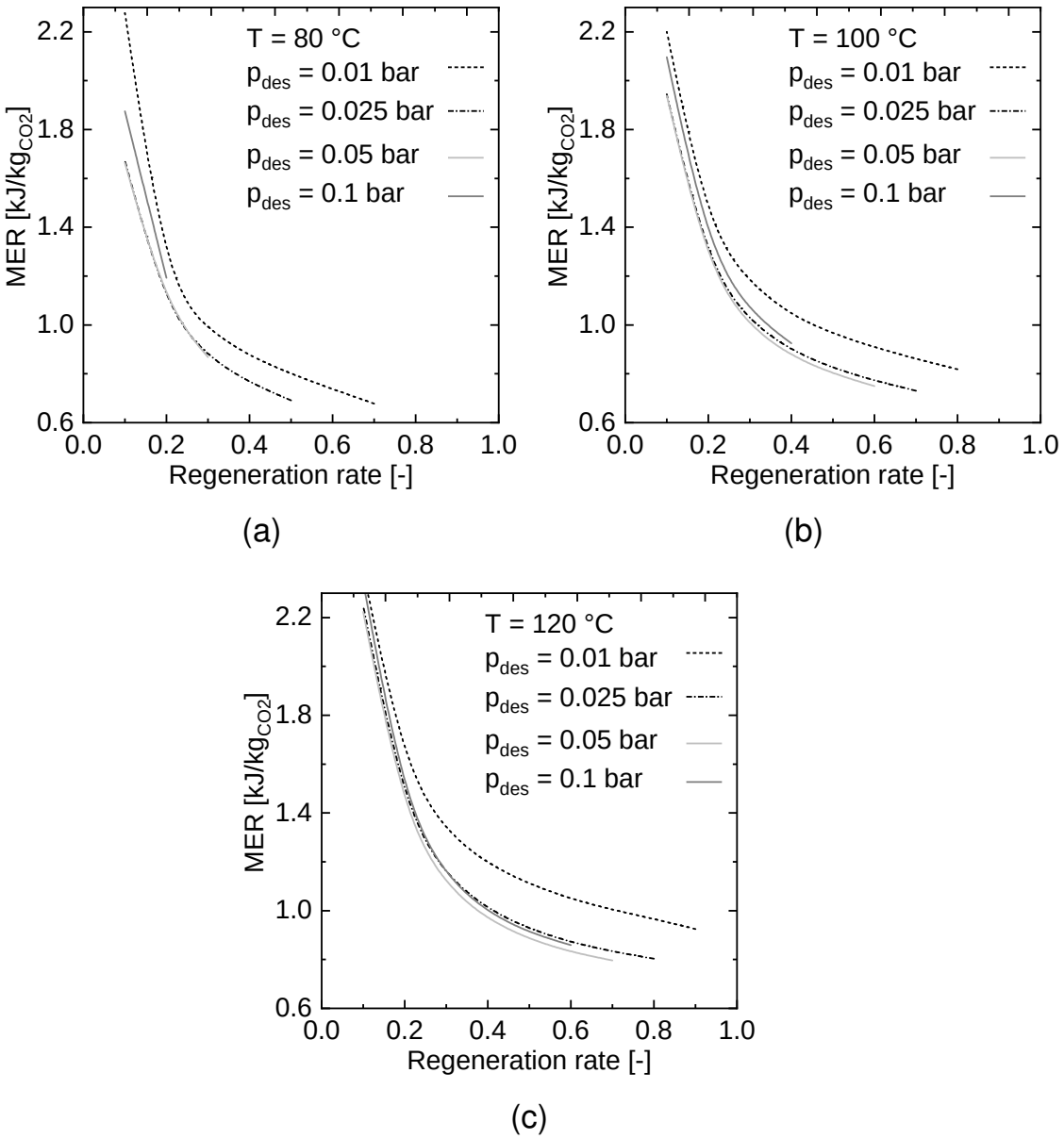


**Figure 6.8:** Minimal energy requirement per $kg_{CO_2}$ for the TVSA process at different regeneration rates with a desorption temperature of (a) 80 °C, (b) 100 °C and (c) 120 °C.

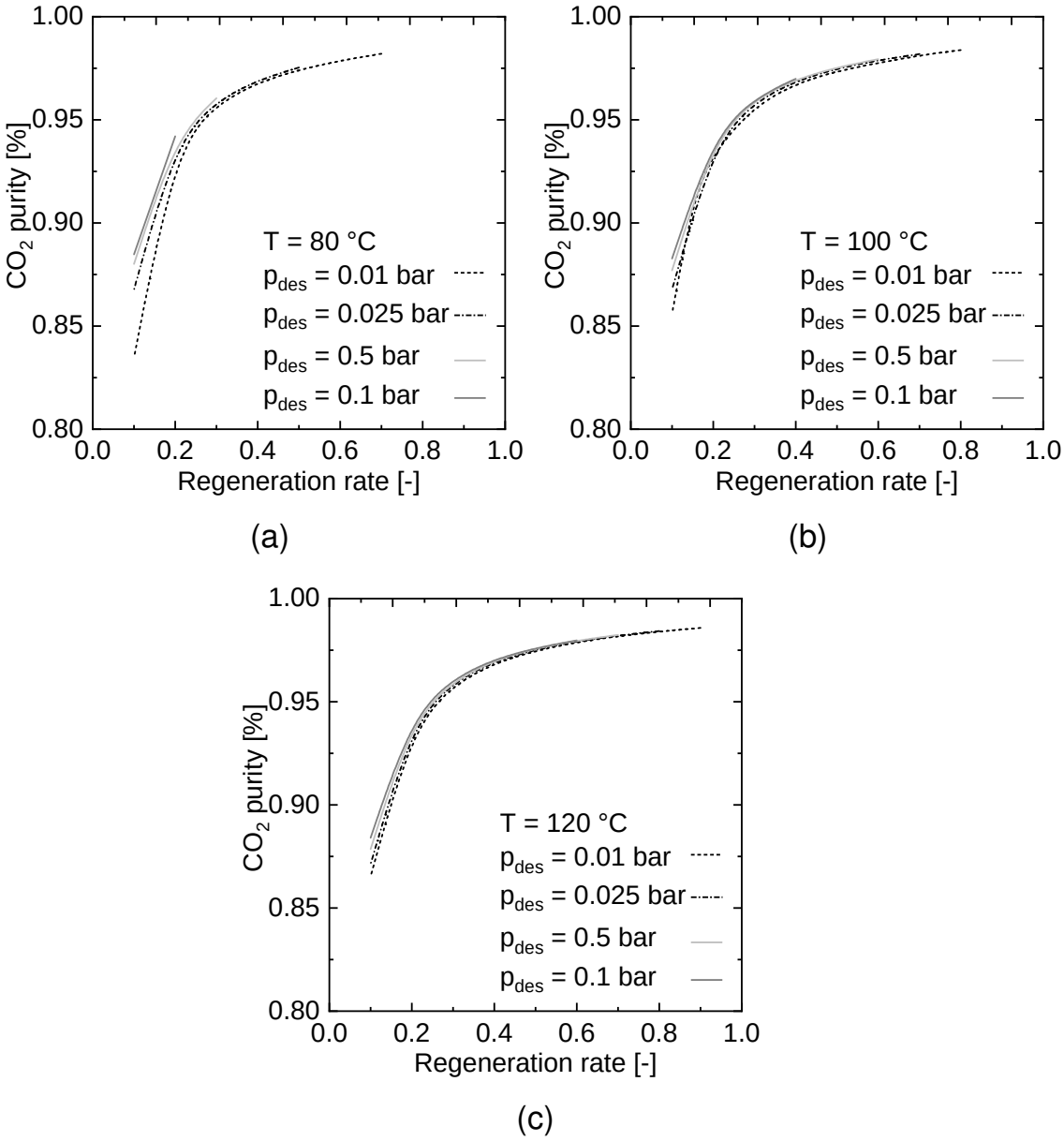


**Figure 6.9:** $CO_2$ purity for the TVSA process at different regeneration rates with a desorption temperature of (a) 80 °C, (b) 100 °C and (c) 120 °C.

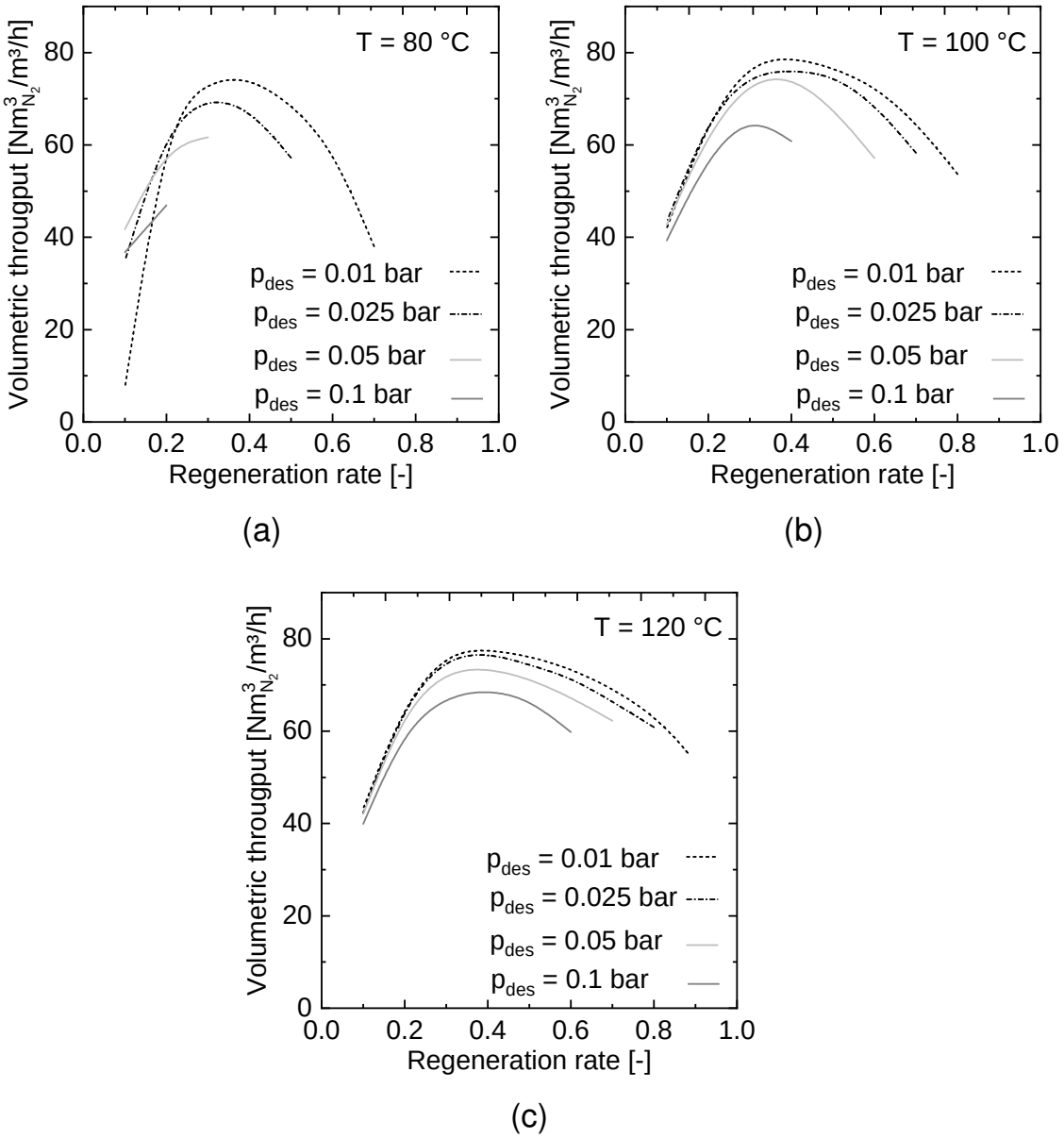


**Figure 6.10:** Volumetric throughput of the TVSA process at different regeneration rates with a desorption temperature of (a) 80 °C, (b) 100 °C and (c) 120 °C.

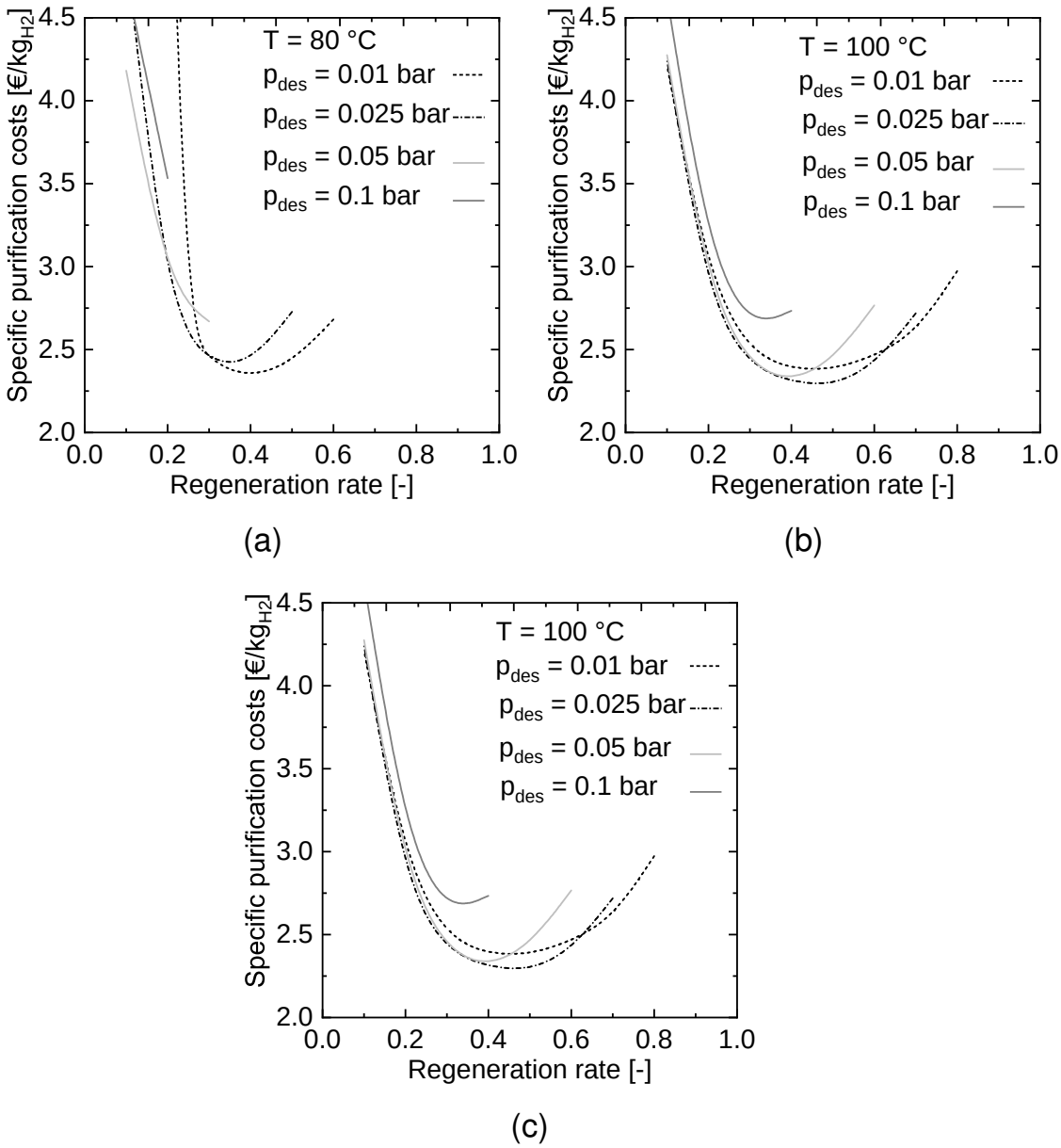


**Figure 6.11:** Separation costs for the $CO_2$ removal per kg hydrogen in the feed for different regeneration rates with a desorption temperature of (a) 80 °C, (b) 100 °C and (c) 120 °C.

## 6.5 Conclusion

This chapter presented a hybrid electrochemical and adsorption-based process for the separation of $H_2$ from a biogenic origin. Such a process does not require the compression of a bulk stream. The techno-economic analysis provides a sound indication of the optimal design of this novel process. The feed stream of the process contains $N_2$, $H_2$ and $CO_2$. In a first step, the $H_2$ is removed electrochemically. Subsequently, $N_2$ and $CO_2$ are separated by a TVSA process. The purified $N_2$ can then be recycled to the process, e.g. for nitrogen sparging of biohydrogen fermentations. To evaluate the potential of different process designs, we considered the energy consumption, the throughput, the $CO_2$ purity, the $N_2$ recovery as well as the specific hydrogen purification costs as process criteria. For both process steps, a trade-off between the operational and investment costs exists. The ECHS process can produce highly purified hydrogen with minimal purification costs of 0.37 €/($kg_{H_2}$) at a cell potential of 0.1 V. For the TVSA-based $CO_2$ separation, we identified a process with a MER in range of 0.73 kJ/$kg_{CO_2}$ and a $CO_2$ purity in the range of 97.2 %. The highest volumetric throughput is 79 $Nm^3$/ ($m^3_{Bed}$ h). However, a trade-off between the volumetric throughput and the MER exists for this process. Interestingly, the lowest costs were identified at a medium desorption temperature and regeneration rate at which the cycle capacity and the cycle duration are well balanced (2.30 €/$kg_{H_2}$ separated). The operation conditions at this point are fairly different from those at the lowest energy consumption. Consequently, taking the MER as the only process criterion does not allow designing TVSA processes. The overall minimal separation costs are 2.67 €/$kg_{H_2}$, which is about 50 % of the prices assumed for hydrogen production from sustainable resources [Eich2016]. Furthermore, the TVSA process produces $CO_2$ with purities above 95 %, which can be sold as a byproduct.

# 7 Conclusion and outlook

## 7.1 Conclusion

For a sustainable future, an alternative energy supply must be developed. Biohydrogen fermentation is particularly attractive as it allows to combine waste treatment and energy production. However, the separation of biohydrogen needs particular attention as it is a main cost driver for this production route. In comparison to conventional large scale separation processes, biohydrogen differs in terms of the feed gas composition, the feed gas pressure and the feed volume stream. Furthermore, the decentralized character requires simple operation modes. In this thesis, separation processes for sustainably produced hydrogen were analyzed and optimized.

In biohydrogen fermentation, $CO_2$ is produced as well and has to be removed before hydrogen utilization. First, hybrid membrane-PSA for the separation of $H_2$ and $CO_2$ was optimized using mixed-integer-non-linear programming. The optimal process designs result in cost of 1.86, 1.02 and 0.60 €/kg$_{H_2}$ for feed compositions of 25 %, 50% and 75%, respectively. Interestingly, the optimal process structure is dependent on the feed compositions. For a hydrogen feed fraction of 25%, low processes pressures are more beneficial. Thus, a stand-alone membrane process outperforms hybrid processes as the partial $CO_2$ pressure difference between adsorption and desorption is only limited.

Besides optimizing the overall process structure, PSA processes can be further improved by hollow fiber sorbents. The hollow fiber design leads to well-defined flow conditions resulting in extended breakthroughs as channeling and dead zones are reduced. Furthermore, mass transfer resistance and pressure loss are decoupled. However, the design of hollow fiber sorbents provides additional variables for the design of pressure swing adsorption processes as the design of the hollow fibers sorbents can be varied as well. Thus, an integrated optimization model for the design of the PSA processes and the hollow fiber sorbents itself was developed. The optimal design results in separation cost of 0.65 €/kg$_{H_2}$ for a hydrogen feed fraction of 75%. Thereby, the overall process costs were reduced by 13% using the optimization model.

Unfortunately, a high hydrogen partial pressure reduces the efficiency of the biohydrogen fermentation. Often nitrogen sparging is applied to increase the hydrogen yield. But this makes the recovery of the hydrogen even more challenging. As hydrogen is present in a diluted bulk stream, compression is uneconomical. Thus, a process using electrochemical hydrogen separation (ECHS) was presented. Furthermore, the $CO_2$, which is present in the gas stream, is separated by a TVSA process. The ECHS process as well as the TVSA suffer from a trade-off between energy and investment costs. At an optimal operation point, the ECHS unit operates at costs of 0.37 €/kg$_{H_2}$. Respectively, the costs for the TVSA process are 2.30 €/kg$_{H_2}$. Thus, the overall separation costs are 2.67 €/kg$_{H_2}$.

The TVSA process uses amine-functionalized solid sorbents, which are particularly attractive due to their high selectivity and chemical stability also at humid conditions. So far, precise but simple and physical reasonable adsorption models for these materials were lacking. Thus, a dual adsorption model has been developed in this work. It describes the adsorption as a combination of surface and bulk adsorption of amine-functionalized materials. With this model, precise adsorption processes, as presented for example in chapter 6, can be developed.

Table 7.1 summarizes the costs related to the different processes (please attend the different feed compositions). For low hydrogen fractions, the separation costs are almost five times higher compared with processes for high hydrogen fractions. This shows the importance to develop biohydrogen production processes with high hydrogen gas fractions. Only if other valuable products such as methane are co-produced, low hydrogen fractions might be acceptable.

**Table 7.1:** Summary of process costs for the different separation design.

| Process | Feed composition [%] | Costs [€/ $kg_{H_2}$] |
|---|---|---|
| Membrane-PSA Case 1 | $H_2$ = 25, $CO_2$ = 75 | 1.86 |
| Membrane-PSA Case 2 | $H_2$ = 50, $CO_2$ = 50 | 1.02 |
| Membrane-PSA Case 3 | $H_2$ = 75, $CO_2$ = 25 | 0.60 |
| Hollow fiber sorbent PSA | $H_2$ = 75, $CO_2$ = 25 | 0.65 |
| ECHS-TVSA | $N_2$ = 70, $H_2$ = 18, $CO_2$ = 12 | 2.67 |

## 7.2 Outlook

In general, the presented processes are easy to operate and can start up and shut down immediately. Thus, the purified and stored hydrogen can be used for smoothing peaks in the electric grid. For example, if alternative energy supply routes such as solar and wind power are not sufficient to satisfy the energy demand, the purified hydrogen can be converted into electric energy by fuel cells or by driving gas turbines or combined heat and power cycles. Herefor, concepts for storage and distribution are currently under development [Andr2012]. These approaches may require the compression of hydrogen. The electrochemical separation process can also pressurize the hydrogen stream by electrochemical hydrogen pumping [Strö2002]. This would allow combining hydrogen separation and compression in a single unit.

Besides conventional biohydrogen production, combined fermentation processes producing both hydrogen and methane are currently under development [Liu2006]. This route allows increasing the methane yield of the biogas production. Furthermore, the methane can be used for sparging which reduces the partial pressure of the hydrogen and thus the inhibition of the fermentation processes. Interestingly, the hybrid electrochemical-temperature swing adsorption process also allows separating the resulting tertiary gas mixture. In future works, it is very interesting to analyze the resulting economics of such a process.

Additionally, the separated $CO_2$ can be used as a feedstock in the chem-

ical, agriculture and food industry, which would close the carbon cycle of the waste material. In particular, hydrogen and $CO_2$ can be converted to methanol [Alsa2019] or methane [Scho2013b]. Then, separating hydrogen and $CO_2$ would not be necessary and simple membrane processes can adjust the hydrogen and $CO_2$ ratio. Therefore, adequate separation processes for the specific composition of the biohydrogen off-gas must be developed.

This work presented an optimization model for the design of hollow fiber sorbents and pressure swing adsorption processes. Hollow fiber sorbents processes have also been applied for TVSA processes. The developed model can be modified to optimize the hollow fiber sorbents for such processes. Currently, many hollow fiber sorbents often consist of both the sorbent materials as well as a polymer fiber. However, heating the polymer binder reduces the energetic efficiency of the processes. Thus, hollow fiber sorbents consisting only of the sorbent material must be developed. Therefore, monolithic metal-organic frameworks are particular attractive [Widm2018].

Finally, for the commercial applications of biohydrogen systems, an overall techno-economic analysis of this production route is necessary. So far, the separation process, which is an important energy consumer and cost driver, gained insufficient attention.

# Bibliography


[Abdo2015] A. Abdollahi-Govar, A. Ebner, and J. Ritter. “New Kinetic Model That Describes the Reversible Adsorption and Desorption Behavior of $CO_2$ in a Solid Amine Sorbent”. *Energy & Fuels* 29.7 (2015). (Cit. on pp. 17, 89, 93–96, 111, 112).

[Abdu2011] A. Abdulla et al. “Efficiency of hydrogen recovery from reformate with a polymer electrolyte hydrogen pump”. *AIChE Journal* 57.7 (2011). (Cit. on p. 19).

[Agar2010] A. Agarwal, L. Biegler, and S. Zitney. “A Superstructure-Based Optimal Synthesis of PSA Cycles for Post-Combustion $CO_2$ Capture”. *AIChE Journal* 56.7 (2010). (Cit. on p. 12).

[Alsa2017a] S. Alsayegh et al. “$CO_2$ aided $H_2$ recovery from water splitting processes”. *International Journal of Hydrogen Energy* 42.34 (2017). (Cit. on p. 12).

[Alsa2017b] S. Alsayegh et al. “Systematic optimization of $H_2$ recovery from water splitting process using membranes and $N_2$ diluent”. *International Journal of Hydrogen Energy* 42.9 (2017). (Cit. on pp. 12, 24, 25).

[Alsa2019] S. Alsayegh et al. “Methanol production via direct carbon dioxide hydrogenation using hydrogen from photocatalytic water splitting: Process development and techno-economic analysis”. *Journal of Cleaner Production* 208 (2019). (Cit. on p. 137).

[Amir2011] S. Amirnordin et al. “Pressure Drop and Analysis of Square and Hexagonal Cells and its Effects and on the Performance and of Catalytic and Converters”. *International Journal of Environmental Science and Development* 2 (2011). (Cit. on p. 113).

[Andr2012] J. Andrews and B. Shabani. “Where does Hydrogen Fit in a Sustainable Energy Economy?” *Procedia Engineering* 49 (2012). (Cit. on p. 136).

[Arim2015] M. Arimi et al. “Strategies for improvement of biohydrogen production from organic-rich wastewater: A review”. *Biomass and Bioenergy* 75 (2015). (Cit. on p. 3).

[Arya2018] N. Aryal et al. “An overview of microbial biogas enrichment”. *Bioresource Technology* 264 (2018). (Cit. on p. 46).

[Avra2003] M. Avramescu et al. “Preparation of mixed matrix adsorber membranes for protein recovery”. *Journal of Membrane Science* 218.1–2 (2003). (Cit. on p. 14).

[Bake1998] R. Baker, J. Wijmans, and J. Kaschemekat. “The design of membrane vapor-gas separation systems”. *Journal of Membrane Science* 151.1 (1998). (Cit. on p. 12).

[Bake2014] R. Baker and B. Low. “Gas Separation Membrane Materials: A Perspective”. *Macromolecules* 47.20 (2014). (Cit. on pp. 11, 12).

[Bako2013a] P. Bakonyi, N. Nemestóthy, and K. Bélafi-Bakó. “Biohydrogen Purification by Membranes: An Overview on the Operational Conditions Affecting the Performance of Non-porous, Polymeric and Ionic Liquid based Gas Separation Membranes”. *Int. J. Hydrogen Energy* 38.23 (2013). (Cit. on pp. 3, 11, 71).

[Bako2013b] P. Bakonyi et al. “Biohydrogen purification using a commercial polyimide membrane module: Studying the effects of some process variables”. *International Journal of Hydrogen Energy* 38.35 (2013). (Cit. on p. 11).

[Bako2015] P. Bakonyi et al. “Simultaneous biohydrogen production and purification in a double-membrane bioreactor system”. *International Journal of Hydrogen Energy* 40.4 (2015). (Cit. on pp. 3, 11).

[Barr2003] L. Barreto, A. Makihira, and K. Riahi. “The hydrogen economy in the 21st century: a sustainable development scenario”. *International Journal of Hydrogen Energy* 28.3 (2003). (Cit. on pp. 10, 71).

[Béla2006] K. Bélafi-Bakó et al. “Integration of biohydrogen fermentation and gas separation processes to recover and enrich hydrogen”. *International Journal of Hydrogen Energy* 31.11 (2006). (Cit. on pp. 3, 4, 11, 12).

[Belm2009] Y. Belmabkhout and A. Sayari. “Effect of pore expansion and amine functionalization of mesoporous silica on $CO_2$ adsorption over a wide range of conditions”. *Adsorption* 15.3 (2009). (Cit. on pp. 5, 16).

[Belm2010a] Y. Belmabkhout, R. Serna-Guerrero, and A. Sayari. “Adsorption of $CO_2$-Containing Gas Mixtures over Amine-Bearing Pore-Expanded MCM-41 Silica: Application for Gas Purification”. *Industrial & Engineering Chemistry Research* 49.1 (2010). (Cit. on pp. 5, 16).

[Belm2010b] Y. Belmabkhout, R. Serna-Guerrero, and A. Sayari. “Amine-bearing mesoporous silica for $CO_2$ removal from dry and humid air”. *Chemical Engineering Science* 65.11 (2010). (Cit. on p. 16).

[Bern2009] P. Bernardo, E. Drioli, and G. Golemme. “Membrane Gas Separation: A Review/State of the Art”. *Industrial & Engineering Chemistry Research* 48.10 (2009). (Cit. on pp. 4, 11, 71).

[Bern2014] W. Bernhart et al. “Fuel cells—a realistic alternative for zero emission?” *Auto tech review* 3.3 (2014). (Cit. on p. 121).

[Bess2010] N. Bessho. “Advanced pressure swing adsorption system with fiber sorbents for hydrogen recovery”. PhD thesis. Georgia Institute of Technology, 2010 (cit. on pp. 50, 59, 61, 62, 73, 78).

[Bhan2010] D. Bhandari, N. Bessho, and W. Koros. “Hollow Fiber Sorbents for Desulfurization of Natural Gas”. *Industrial & Engineering Chemistry Research* 49.23 (2010). (Cit. on p. 80).

[Bhan2013] D. Bhandari et al. “Dual Layer Hollow Fiber Sorbents: Concept, Fabrication and Characterization”. *Separation and Purification Technology* 104.0 (2013). (Cit. on p. 14).

[Bhar2016] B. Bharathiraja et al. “Biohydrogen and Biogas - An overview on feedstocks and enhancement process”. *Fuel* 185 (2016). (Cit. on pp. 36, 71, 120).

[Bieg1997] L. Biegler, I. Grossmann, and A. Westerberg. *Systematic methods of chemical process design*. Prentice-Hall international series in the physical and chemical engineering sciences. Prentice Hall PTR, 1997 (cit. on pp. 31, 34, 37, 67, 119).

[Bieg2005] L. Biegler, L. Jiang, and V. Fox. “Recent Advances in Simulation and Optimal Design of Pressure Swing Adsorption Systems”. *Separation & Purification Reviews* 33.1 (2005). (Cit. on p. 51).

[Boll2012a] P. Bollini et al. “Dynamics of $CO_2$ Adsorption on Amine Adsorbents. 1. Impact of Heat Effects”. *Industrial & Engineering Chemistry Research* 51.46 (2012). (Cit. on p. 17).

[Boll2012b] P. Bollini et al. “Dynamics of $CO_2$ Adsorption on Amine Adsorbents. 2. Insights Into Adsorbent Design”. *Industrial & Engineering Chemistry Research* 51.46 (2012). (Cit. on p. 17).

[Brun2010] A. Brunetti et al. “Membrane technologies for $CO_2$ separation”. *Journal of Membrane Science* 359.1 (2010). (Cit. on pp. 4, 12, 71).

[Carm2013] M. Carmo et al. “A comprehensive review on PEM water electrolysis”. *International Journal of Hydrogen Energy* 38.12 (2013). (Cit. on p. 10).

[Carr2010] A. Carrara, A. Perdichizzi, and G. Barigozzi. “Simulation of an hydrogen production steam reforming industrial plant for energetic performance prediction”. *International Journal of Hydrogen Energy* 35.8 (2010). (Cit. on p. 13).

[Chah2001] M. Chahbani and D. Tondeur. “Pressure Drop in Fixed-Bed Adsorbers”. *Chemical Engineering Journal* 81.1 (2001). (Cit. on p. 51).

[Chan2015] K. Chandrasekhar, Y. Lee, and D. Lee. “Biohydrogen production: strategies to improve process efficiency through microbial routes”. *International journal of molecular sciences* 16.4 (2015). (Cit. on p. 3).

[Chen1994] W. Cheng. *Methanol production and use*. CRC Press, 1994 (cit. on p. 71).

[Choi2004] P. Choi, D. Bessarabov, and R. Datta. “A simple model for solid polymer electrolyte SPE water electrolysis”. *Solid State Ionics* 175.1 (2004). (Cit. on p. 105).

[Choi2009] S. Choi, J. Drese, and C. Jones. “Adsorbent Materials for Carbon Dioxide Capture from Large Anthropogenic Point Sources”. *ChemSusChem* 2.9 (2009). (Cit. on pp. 12, 16, 104).

[Chou1995] V. Choudhary, S. Mayadevi, and A. Singh. “Sorption isotherms of methane, ethane, ethene and carbon dioxide on NaX, NaY and Na-mordenite zeolites”. *Journal of the Chemical Society , Faraday Transactions* 91 (17 1995). (Cit. on p. 61).

[Chu2012] S. Chu and A. Majumdar. “Opportunities and challenges for a sustainable energy future”. *Nature* 488.7411 (2012). (Cit. on p. 10).

[Chun1998] Y. Chung, B. Na, and H. Song. “Short-cut evaluation of pressure swing adsorption systems”. *Computers & Chemical Engineering* 22 (1998). (Cit. on p. 27).

[Clau2011] M. Clausse, J. Merel, and F. Meunier. “Numerical parametric study on $CO_2$ capture by indirect thermal swing adsorption”. *International Journal of Greenhouse Gas Control* 5.5 (2011). (Cit. on p. 19).

[Coke1998] D. Coker, B. Freeman, and G. Fleming. “Modeling Multicomponent Gas Separation using Hollow-Fiber Membrane Contactors”. *AIChE Journal* 44.6 (1998). (Cit. on p. 78).

[DAle2010] D. D’Alessandro, B. Smit, and J. Long. “Carbon Dioxide Capture: Prospects for New Materials”. *Angewandte Chemie International Edition* 49.35 (2010). (Cit. on pp. 16, 104).

[Das2001] D. Das. “Hydrogen production by biological processes: a survey of literature”. *International Journal of Hydrogen Energy* 26.1 (2001). (Cit. on p. 10).

[Das2008] D. Das and T. Veziroglu. “Advances in biological hydrogen production processes”. *International Journal of Hydrogen Energy* 33.21 (2008). (Cit. on p. 10).

[Delg2014] J. Delgado et al. “Adsorption and Diffusion of $H_2$, CO, $CH_4$, and $CO_2$ in BPL Activated Carbon and 13X Zeolite: Evaluation of Performance in Pressure Swing Adsorption Hydrogen Purification by Simulation”. *Industrial & Engineering Chemistry Research* 53.40 (2014). (Cit. on p. 29).

[Dete2012] M. Determan, D. Hoysall, and S. Garimella. “Heat- and Mass-Transfer Kinetics of Carbon Dioxide Capture Using Sorbent-Loaded Hollow Fibers”. *Industrial & Engineering Chemistry Research* 51.1 (2012). (Cit. on p. 50).

[Dine2018] G. Dinesh, R. Chauhan, and S. Chakma. “Influence and strategies for enhanced biohydrogen production from food waste”. *Renewable & Sustainable Energy Reviews* 92 (2018). (Cit. on p. 10).

[DNV 2017] DNV, GL. *Energy Transition Outlook*. 2017 (cit. on p. 2).

[Dunn2002] S. Dunn. “Hydrogen futures: toward a sustainable energy system”. *International Journal of Hydrogen Energy* 27.3 (2002). (Cit. on p. 2).

[Dutc2015] B. Dutcher, M. Fan, and A. Russell. “Amine-Based $CO_2$ Capture Technology Development from the Beginning of 2013 – A Review”. *ACS Applied Materials & Interfaces* 7.4 (2015). (Cit. on p. 16).

[Ebne2011] A. Ebner et al. “Suitability of a Solid Amine Sorbent for $CO_2$ Capture by Pressure Swing Adsorption”. *Industrial & Engineering Chemistry Research* 50.9 (2011). (Cit. on pp. 88, 92, 97).

[Edwa2008] P. Edwards et al. “Hydrogen and fuel cells: Towards a sustainable energy future”. *Energy Policy* 36.12 (2008). (Cit. on pp. 10, 71).

[Eich2016] J. Eichman, A. Townsend, and M. Melaina. *Economic Assessment of Hydrogen Technologies Participating in California Electricity Markets. Technical Report, REL/TP-5400-6585, Contract DE-AC36-08GO28308 NREL (National Renewable Energy Laboratory (NREL), Golden, CO*. 2016 (cit. on p. 132).

[Elsh2013] O. Elsharnouby et al. “A critical literature review on biohydrogen production by pure cultures”. *International Journal of Hydrogen Energy* 38.12 (2013). (Cit. on pp. 3, 10).

[Eris2008] J. Erisman et al. “How a century of ammonia synthesis changed the world”. *Nature Geoscience* 1.10 (2008). (Cit. on p. 71).

[Este2002] I. Esteves and J. Mota. “Simulation of a new hybrid membrane/-pressure swing adsorption process for gas separation”. *Desalination* 148.1 (2002). (Cit. on pp. 4, 12).

[Este2007] I. Esteves and J. Mota. “Gas Separation by a Novel Hybrid Membrane/Pressure Swing Adsorption Process”. *Industrial & Engineering Chemistry Research* 46.17 (2007). (Cit. on pp. 4, 12).

[Feng1998] X. Feng et al. “Hollow-fiber-based adsorbers for gas separation by pressure-swing adsorption”. *AIChE Journal* 44.7 (1998). (Cit. on p. 14).

[Gard2007] C. Gardner and M. Ternan. “Electrochemical separation of hydrogen from reformate using PEM fuel cell technology”. *Journal of Power Sources* 171.2 (2007). (Cit. on p. 122).

[Guo2010] X. Guo et al. “Hydrogen production from agricultural waste by dark fermentation: A review”. *International Journal of Hydrogen Energy* 35.19 (2010). (Cit. on p. 10).

[Guth1969] K. Guthrie. “Data and techniques for preliminary capital cost estimating”. *Chemical Engineering* 76.6 (1969). (Cit. on p. 38).

[Han2017] W. Han et al. “Simultaneous dark fermentative hydrogen and ethanol production from waste bread in a mixed packed tank reactor”. *Journal of Cleaner Production* 141 (2017). (Cit. on p. 10).

[Hara2007] M. Harasimowicz et al. “Application of polyimide membranes for biogas purification and enrichment”. *Journal of Hazardous Materials* 144.3 (2007). (Cit. on pp. 11, 71).

[Hasa2013] M. Hasan, E. First, and C. Floudas. “Cost-effective $CO_2$ Capture based on In Silico Screening of Zeolites and Process Optimization”. *Physical Chemistry Chemical Physics* 15.40 (2013). (Cit. on p. 12).

[Haya1996] S. Hayashi, M. Kawai, and T. Kaneko. “Dynamics of High Purity Oxygen PSA”. *Gas Separation & Purification* 10.1 (1996). (Cit. on p. 12).

[Heyd2011a] A. Heydari-Gorji, Y. Belmabkhout, and A. Sayari. “Polyethylenimine-Impregnated Mesoporous Silica: Effect of Amine Loading and Surface Alkyl Chains on $CO_2$ Adsorption”. *Langmuir* 27.20 (2011). (Cit. on p. 16).

[Heyd2011b] A. Heydari-Gorji and A. Sayari. “$CO_2$ capture on polyethylenimine-impregnated hydrophobic mesoporous silica: Experimental and kinetic modeling”. *Chemical Engineering Journal* 173.1 (2011). (Cit. on pp. 16–18, 87, 96).

[Hiyo2005] N. Hiyoshi, K. Yogo, and T. Yashima. “Adsorption characteristics of carbon dioxide on organically functionalized SBA-15”. *Microporous and Mesoporous Materials* 84.1–3 (2005). (Cit. on p. 16).

[Ho2008] M. Ho, G. Allinson, and D. Wiley. “Reducing the Cost of $CO_2$ Capture from Flue Gases Using Pressure Swing Adsorption”. *Industrial & Engineering Chemistry Research* 47.14 (2008). (Cit. on p. 12).

[Horv2004] R. Horváth et al. “Application of gas separation to recover biohydrogen produced by Thiocapsa roseopersicina”. *Desalination* 163.1–3 (2004). (Cit. on pp. 11, 71).

[Huan2014] Y. Huang, T. Merkel, and R. Baker. “Pressure ratio and its impact on membrane gas separation processes”. *Journal of Membrane Science* 463 (2014). (Cit. on p. 12).

[Huft1999] J. Hufton, S. Mayorga, and S. Sircar. “Sorption-enhanced reaction process for hydrogen production”. *AIChE Journal* 45.2 (1999). (Cit. on pp. 4, 12, 71).

[Ibeh2007] B. Ibeh, C. Gardner, and M. Ternan. “Separation of hydrogen from a hydrogen/methane mixture using a PEM fuel cell”. *International Journal of Hydrogen Energy* 32.7 (2007). (Cit. on p. 19).

[Inte2015] Intergovernmental Panel on Climate Change. *Climate Change 2014: Mitigation of Climate Change*. Vol. 3. Cambridge University Press, 2015 (cit. on p. 15).

[Jian2003] L. Jiang, L. Biegler, and V. Fox. “Simulation and optimization of pressure-swing adsorption systems for air separation”. *AIChE Journal* 49.5 (2003). (Cit. on pp. 12, 65).

[Kaly2015] J. Kalyanaraman et al. “Modeling and Experimental Validation of Carbon Dioxide Sorption on Hollow Fibers Loaded with Silica-Supported Poly(ethylenimine)”. *Chemical Engineering Journal* 259 (2015). (Cit. on p. 14).

[Kapd2006] I. Kapdan and F. Kargi. “Bio-hydrogen production from waste materials”. *Enzyme and Microbial Technology* 38.5 (2006). (Cit. on pp. 10, 36, 71, 120).

[Keit2009] D. Keith. “Why capture $CO_2$ from the atmosphere?” *Science* 325.5948 (2009). (Cit. on p. 16).

[Kell2018] L. Keller et al. “High capacity polyethylenimine impregnated microtubes made of carbon nanotubes for $CO_2$ capture”. *Carbon* 126 (2018). (Cit. on pp. 5, 15, 16).

[Kim2006] D. Kim et al. “Effect of gas sparging on continuous fermentative hydrogen production”. *International Journal of Hydrogen Energy* 31.15 (2006). (Cit. on p. 10).

[Ko2003] D. Ko, R. Siriwardane, and L. Biegler. “Optimization of a pressure-swing adsorption process using zeolite 13X for CO2 sequestration”. *Industrial & Engineering Chemistry Research* 42.2 (2003). (Cit. on pp. 12, 51, 65, 69, 70, 72, 73, 78, 110).

[Ko2005] D. Ko, R. Siriwardane, and L. Biegler. “Optimization of Pressure Swing Adsorption and Fractionated Vacuum Pressure Swing Adsorption Processes for $CO_2$ Capture”. *Industrial & Engineering Chemistry Research* 44.21 (2005). (Cit. on pp. 12, 72).

[Krae2008] J. Kraemer and D. Bagley. “Optimisation and design of nitrogen-sparged fermentative hydrogen production bioreactors”. *International Journal of Hydrogen Energy* 33.22 (2008). (Cit. on p. 120).

[Kudo2009] A. Kudo and Y. Miseki. “Heterogeneous photocatalyst materials for water splitting”. *Chemical Society Reviews* 38.1 (2009). (Cit. on p. 10).

[Kugl2014] K. Kugler et al. “Towards a carbon independent and $CO_2$-free electrochemical membrane process for $NH_3$ synthesis”. *Physical Chemistry Chemical Physics* 16.13 (2014). (Cit. on pp. 105, 107).

[Kulk2012] A. R. Kulkarni and D. S. Sholl. “Analysis of Equilibrium-Based TSA Processes for Direct Capture of $CO_2$ from Air”. *Industrial & Engineering Chemistry Research* 51.25 (2012). (Cit. on pp. 115–117).

[Labr2014] Y. Labreche et al. “Poly(amide-imide)/Silica Supported PEI Hollow Fiber Sorbents for Postcombustion $CO_2$ Capture by RTSA”. *ACS Applied Materials & Interfaces* 6.21 (2014). (Cit. on p. 14).

[Lee2012] K. Lee et al. “Enhancing the performance of dark fermentative hydrogen production using a reduced pressure fermentation strategy”. *International Journal of Hydrogen Energy* 37.20 (2012). (Cit. on p. 10).

[Leta2014] D. Leta et al. *Temperature swing adsorption process for the separation of target species from a gas mixture*. US Patent 8,784,533. 2014 (cit. on p. 98).

[LeVa2014] T. LeValley, A. Richard, and M. Fan. “The progress in water gas shift and steam reforming hydrogen production technologies – A review”. *International Journal of Hydrogen Energy* 39.30 (2014). (Cit. on p. 3).

[Levi2004] D. Levin, L. Pitt, and M. Love. “Biohydrogen production: prospects and limitations to practical application”. *International Journal of Hydrogen Energy* 29.2 (2004). (Cit. on pp. 2, 3, 10, 71).

[Levi2010] D. Levin and R. Chahine. “Challenges for renewable hydrogen production from biomass”. *International Journal of Hydrogen Energy* 35.10 (2010). (Cit. on p. 37).

[Li2009] J. Li, R. Kuppler, and H. Zhou. “Selective Gas Adsorption and Separation in Metal–Organic Frameworks”. *Chemical Society Reviews* 38.5 (2009). (Cit. on p. 12).

[Li2016a] B. Li et al. “Pressure swing adsorption/membrane hybrid processes for hydrogen purification with a high recovery”. *Frontiers of Chemical Science and Engineering* 10.2 (2016). (Cit. on pp. 4, 12).

[Li2016b] D. Li et al. “Experiment and simulation for separating $CO_2$/$N_2$ by dual-reflux pressure swing adsorption process”. *Chemical Engineering Journal* 297 (2016). (Cit. on p. 27).

[Liao2010] Z. Liao et al. “Integrating purifiers in refinery hydrogen networks: a retrofit case study”. *Journal of Cleaner Production* 18.3 (2010). (Cit. on p. 37).

[Lin2014] H. Lin et al. “$CO_2$-selective membranes for hydrogen production and $CO_2$ capture - Part I: Membrane development”. *Journal of Membrane Science* 457 (2014). (Cit. on p. 25).

[Lin2015] H. Lin et al. “$CO_2$-selective membranes for hydrogen production and $CO_2$ capture - Part II: Techno-economic analysis”. *Journal of Membrane Science* 493 (2015). (Cit. on pp. 36, 37).

[Lind2016] Linde Engineering AG. *Hydrogen Recovery by Pressure Swing Adsorption*. (accessed July 2017). 2016 (cit. on p. 26).

[Liu2006] D. Liu et al. “Hydrogen and methane production from household solid waste in the two-stage fermentation process”. *Water Research* 40.11 (2006). (Cit. on p. 136).

[Liu2011] Y. Liu et al. “Carbon Dioxide Capture by Functionalized Solid Amine Sorbents with Simulated Flue Gas Conditions”. *Environmental Science & Technology* 45.13 (2011). (Cit. on pp. 5, 16).

[Liu2014] Q. Liu et al. “Kinetics Studies of $CO_2$ Adsorption/Desorption on Amine-Functionalized Multiwalled Carbon Nanotubes”. *Industrial & Engineering Chemistry Research* 53.29 (2014). (Cit. on pp. 16, 92, 94, 96).

[Live2012a] R. Lively et al. *Sorbent fiber compositions and methods of temperature swing adsorption*. US Patent 8,133,308. 2012 (cit. on p. 14).

[Live2012b] R. Lively et al. “Thermally moderated hollow fiber sorbent modules in rapidly cycled pressure swing adsorption mode for hydrogen purification”. *International Journal of Hydrogen Energy* 37.20 (2012). (Cit. on pp. 14, 50, 52, 54, 62, 73, 76, 77).

[Loff2003] D. Loffler, K. Taylor, and D. Mason. “A light hydrocarbon fuel processor producing high-purity hydrogen”. *Journal of Power Sources* 117.1 (2003). (Cit. on pp. 4, 12, 71).

[Lope2003] E. Lopes et al. “An alternative Avrami equation to evaluate kinetic parameters of the interaction of Hg(II) with thin chitosan membranes”. *Journal of Colloid and Interface Science* 263.2 (2003). (Cit. on p. 87).

[Lope2009] F. Lopes et al. “Adsorption of $H_2$, $CO_2$, $CH_4$, CO, $N_2$ and $H_2O$ in activated carbon and zeolite for hydrogen production”. *Separation Science and Technology* 44.5 (2009). (Cit. on p. 37).

[Lund2007] H. Lund. “Renewable energy strategies for sustainable development”. *Energy* 32.6 (2007). (Cit. on p. 10).

[Maed2010] K. Maeda and K. Domen. “Photocatalytic water splitting: recent progress and future challenges”. *Journal of Physical Chemistry Letters* 1.18 (2010). (Cit. on p. 10).

[Mass2016] J. Massanet-Nicolau et al. “Maximising biohydrogen yields via continuous electrochemical hydrogen removal and carbon dioxide scrubbing”. *Bioresource Technology* 218 (2016). (Cit. on pp. 11, 19, 104).

[Mell2011] M. Mello et al. “Amine-modified MCM-41 mesoporous silica for carbon dioxide capture”. *Microporous and Mesoporous Materials* 143.1 (2011). (Cit. on pp. 5, 16).

[Milt2010] A. Miltner et al. “Renewable hydrogen production: a technical evaluation based on process simulation”. *Journal of Cleaner Production* 18 (2010). (Cit. on p. 10).

[Mizu2000] O. Mizuno et al. “Enhancement of hydrogen production from glucose by nitrogen gas sparging”. *Bioresource Technology* 73.1 (2000). (Cit. on p. 10).

[Modi2008] M. Modigell et al. “A membrane contactor for efficient $CO_2$ removal in biohydrogen production”. *Desalination* 224.1–3 (2008). (Cit. on pp. 11, 71).

[Mona2013] E. Monazam et al. “Equilibrium and kinetics analysis of carbon dioxide capture using immobilized amine on a mesoporous silica”. *AIChE Journal* 59.3 (2013). (Cit. on pp. 16, 92).

[Mosc2008] A. Mosca et al. “Optimization of Synthesis Procedures for Structured PSA Adsorbents”. *Adsorption* 14.4 (2008). (Cit. on p. 12).

[Nath2004] K. Nath and D. Das. “Improvement of fermentative hydrogen production: Various approaches”. *Appl. Microbiol. Biotechnol.* 65.5 (2004). (Cit. on p. 10).

[Neve2009] L. Neves et al. “Separation of biohydrogen by supported ionic liquid membranes”. *Desalination* 240.1–3 (2009). (Cit. on p. 11).

[Nguy2010] T. Nguyen et al. “Hydrogen production of the hyperthermophilic eubacterium, Thermotoga neapolitana under $N_2$ sparging condition”. *Bioresource Technology* 101.1, Supplement (2010). (Cit. on p. 10).

[Niko2015] D. Nikolić and E. Kikkinides. “Modelling and optimization of hybrid PSA/membrane separation processes”. *Adsorption* 21.4 (2015). (Cit. on p. 13).

[Ntia2016] A. Ntiamoah et al. “$CO_2$ Capture by Temperature Swing Adsorption: Use of Hot $CO_2$-Rich Gas for Regeneration”. *Industrial & Engineering Chemistry Research* 55.3 (2016). (Cit. on pp. 16, 104).

[Ocho2007] E. Ochoa-Fernández et al. “Process design simulation of $H_2$ production by sorption enhanced steam methane reforming: evaluation of potential $CO_2$ acceptors”. *Green Chemistry* 9.6 (2007). (Cit. on p. 13).

[Ockw2007] N. Ockwig and T. Nenoff. “Membranes for Hydrogen Separation”. *Chemical Reviews* 107.10 (2007). (Cit. on pp. 4, 12, 13).

[Offe2010] G. Offer et al. “Comparative Analysis of Battery Electric, Hydrogen Fuel Cell and Hybrid Vehicles in a Future Sustainable Road Transport System”. *Energy Policy* 38.1 (2010). (Cit. on p. 77).

[Ogoh2009] D. G. W. Ogoh. “Solid-liquid phase change simulation applied to a cylindrical latent heat energy storage system”. In*COMSOL Conference 2009*. 2009 (cit. on p. 60).

[Oh2009] S. Oh et al. “Hydrogen production by *Clostridium acetobutylicum* ATCC 824 and megaplasmid-deficient mutant M5 evaluated using a large headspace volume technique”. *International Journal of Hydrogen Energy* 34.23 (2009). (Cit. on p. 10).

[Ohs2016] B. Ohs, J. Lohaus, and M. Wessling. “Optimization of membrane based nitrogen removal from natural gas”. *Journal of Membrane Science* 498 (2016). (Cit. on pp. 12, 22, 24, 25, 66).

[Ohs2018a] B. Ohs, M. Krödel, and M. Wessling. “Adsorption of carbon dioxide on solid amine-functionalized sorbents: A dual kinetic model”. *Separation and Purification Technology* 204 (2018). (Cit. on pp. 89, 111).

[Ohs2018b] B. Ohs et al. “Optimized hollow fiber sorbents and pressure swing adsorption process for H2 recovery”. *Industrial & Engineering Chemistry Research* 57.14 (2018). (Cit. on pp. 4, 12, 55, 57, 61, 72, 121).

[Qi1998] R. Qi and M. Henson. “Optimization-based design of spiral-wound membrane systems for $CO_2$/$CH_4$ separations”. *Separation and Purification Technology* 13.3 (1998). (Cit. on p. 12).

[Ramí2013] J. Ramírez-Morales et al. “Evaluation of two gas membrane modules for fermentative hydrogen separation”. *International Journal of Hydrogen Energy* 38.32 (2013). (Cit. on p. 10).

[Reza2010a] F. Rezaei and P. Webley. “Structured Adsorbents in Gas Separation Processes”. *Separation and Purification Technology* 70.3 (2010). (Cit. on pp. 12, 50).

[Reza2010b] F. Rezaei et al. “Comparison of Traditional and Structured Adsorbents for CO2 Separation by Vacuum-Swing Adsorption”. *Industrial & Engineering Chemistry Research* 49.10 (2010). (Cit. on p. 12).

[Reza2014] F. Rezaei et al. “Modeling of rapid temperature swing adsorption using hollow fiber sorbents”. *Chemical Engineering Science* 113 (2014). (Cit. on p. 15).

[Ruth1994] D. Ruthven, S. Farooq, and K. Knaebel. *Pressure Swing Adsorption*. VCH, 1994 (cit. on pp. 12, 62).

[Sama2012] A. Samanta et al. “Post-Combustion $CO_2$ Capture Using Solid Sorbents: A Review”. *Industrial & Engineering Chemistry Research* 51.4 (2012). (Cit. on p. 16).

[Sand2013] D. Sanders et al. “Energy-efficient polymeric gas separation membranes for a sustainable future: A review”. *Polymer* 54.18 (2013). (Cit. on pp. 4, 11, 71).

[Saya2011] A. Sayari, Y. Belmabkhout, and R. Serna-Guerrero. “Flue gas treatment via $CO_2$ adsorption”. *Chemical Engineering Journal* 171.3 (2011). (Cit. on p. 16).

[Scho2013a] M. Scholz, T. Melin, and M. Wessling. “Transforming biogas into biomethane using membrane technology”. *Renewable and Sustainable Energy Reviews* 17 (2013). (Cit. on pp. 11, 37, 121).

[Scho2013b] M. Scholz and M. Wessling. “Membrane based biogas upgrading processes”. PhD thesis. Hochschulbibliothek der Rheinisch-Westfälischen Technischen Hochschule Aachen, 2013 (cit. on p. 137).

[Scho2015a] M. Scholz et al. “Dynamic process simulation and process control of biogas permeation processes”. *Journal of Membrane Science* 484 (2015). (Cit. on pp. 4, 11).

[Scho2015b] M. Scholz et al. “Structural optimization of membrane-based biogas upgrading processes”. *Journal of Membrane Science* 474.0 (2015). (Cit. on pp. 12, 24, 25).

[Sedl1981] J. Sedlak, J. Austin, and A. LaConti. “Hydrogen recovery and purification using the solid polymer electrolyte electrolysis cell”. *International Journal of Hydrogen Energy* 6.1 (1981). (Cit. on pp. 5, 19).

[Sern2010] R. Serna-Guerrero and A. Sayari. “Modeling adsorption of $CO_2$ on amine-functionalized mesoporous silica. 2: Kinetics and breakthrough curves”. *Chemical Engineering Journal* 161.1–2 (2010). (Cit. on pp. 16, 17, 86, 87, 89, 91, 94, 97, 98).

[Shal2015] M. Shalygin et al. “Membrane recovery of hydrogen from gaseous mixtures of biogenic and technogenic origin”. *International Journal of Hydrogen Energy* 40.8 (2015). (Cit. on p. 36).

[Sing2015] L. Singh and Z. Wahid. “Methods for enhancing bio-hydrogen production from biological process: A review”. *Journal of Industrial and Engineering Chemistry* 21 (2015). (Cit. on p. 3).

[Sirc1999] S. Sircar et al. “Hydrogen production by hybrid SMR-PSA-SSF membrane system”. *Separation and Purification Technology* 17.1 (1999). (Cit. on pp. 4, 12, 13, 23).

[Sirc2000a] S. Sircar and T. Golden. “Purification of hydrogen by pressure swing adsorption”. *Separation Science and Technology* 35.5 (2000). (Cit. on pp. 4, 12, 71).

[Sirc2000b] S. Sircar and J. Hufton. “Why Does the Linear Driving Force Model for Adsorption Kinetics Work?” *Adsorption* 6.2 (2000). (Cit. on p. 60).

[Sirc2002] S. Sircar. “Pressure Swing Adsorption”. *Industrial & Engineering Chemistry Research* 41.6 (2002). (Cit. on p. 12).

[Skib2012] M. Skiborowski et al. “Model-based structural optimization of seawater desalination plants”. *Desalination* 292 (2012). (Cit. on p. 22).

[Smit1991] O. Smith and A. Westerberg. “The optimal design of pressure swing adsorption systems”. *Chemical Engineering Science* 46.12 (1991). (Cit. on p. 65).

[Son2008] W. Son, J. Choi, and W. Ahn. “Adsorptive removal of carbon dioxide using polyethyleneimine-loaded mesoporous silica materials”. *Microporous and Mesoporous Materials* 113.1–3 (2008). (Cit. on p. 16).

[Stol2016] D. Stolten. *Hydrogen Science and Engineering: Materials, Processes, Systems and Technology, 2 Volume Set*. John Wiley & Sons, 2016 (cit. on pp. 10, 71).

[Strö2002] R. Ströbel et al. “The compression of hydrogen in an electrochemical cell based on a PE fuel cell design”. *Journal of Power Sources* 105.2 (2002). (Cit. on p. 136).

[Tagl2009] M. Tagliabue et al. “Natural Gas Treating by Selective Adsorption: Material Science and Chemical Engineering Interplay”. *Chemical Engineering Journal* 155.3 (2009). (Cit. on p. 12).

[Tepl2002] V. Teplyakov et al. “Lab-scale bioreactor integrated with active membrane system for hydrogen production: experience and prospects”. *International Journal of Hydrogen Energy* 27.11–12 (2002). (Cit. on pp. 11, 71).

[Tlil2009] N. Tlili, G. Grévillot, and C. Vallières. “Carbon dioxide capture and recovery by means of TSA and/or VSA”. *International Journal of Greenhouse Gas Control* 3.5 (2009). (Cit. on p. 19).

[Turn2004] J. Turner. “Sustainable hydrogen production”. *Science* 305.5686 (2004). (Cit. on p. 10).

[US D2015] U.S. Department of Energy. *DOE Technical Targets for Photobiological Hydrogen Production*. 2015. URL: https://www.energy.gov/eere/fuelcells/doe-technical-targets-photobiological-hydrogen-production (visited on 01/09/2019) (cit. on p. 38).

[Venn2011] P. Vennestrøm et al. “Beyond Petrochemicals: The Renewable Chemicals Industry”. *Angewandte Chemie International Edition* 50.45 (2011). (Cit. on pp. 10, 71).

[Wang2014] J. Wang et al. “Recent advances in solid sorbents for $CO_2$ capture and new development trends”. *Energy & Environmental Science* 7.11 (2014). (Cit. on p. 16).

[Wang2018] H. Wang et al. “A review on bio-hydrogen production technology”. *International Journal of Energy Research* 42.11 (2018). (Cit. on p. 10).

[Wend2010] H. Wendt and G. Kreysa. *Electrochemical Engineering: Science and Technology in Chemical and Other Industries*. Springer, 2010 (cit. on pp. 105–108).

[Widm2018] R. Widmer et al. “Manufacturing Macroporous Monoliths of Microporous Metal–Organic Frameworks”. *ACS Applied Nano Materials* 1.2 (2018). (Cit. on p. 137).

[Wies1988] F. Wiessner. “Basics and industrial applications of pressure swing adsorption (PSA), the modern way to separate gas”. *Gas Separation & Purification* 2.3 (1988). (Cit. on p. 37).

[Wurz2011] J. Wurzbacher, C. Gebald, and A. Steinfeld. “Separation of $CO_2$ from air by temperature-vacuum swing adsorption using diamine-functionalized silica gel”. *Energy & Environmental Science* 4.9 (2011). (Cit. on p. 117).

[Yang1997] J. Yang, C. Lee, and J. Chang. “Separation of Hydrogen Mixtures by a Two-Bed Pressure Swing Adsorption Process Using Zeolite 5A”. *Ind. Eng. Chem. Res.* 36.7 (1997). (Cit. on p. 73).

[Yoon2008] S. Yoon, S. Lee, and I. Yeom. “Experimental Verification of Pressure Drop Models in Hollow Fiber Membrane”. *Journal of Membrane Science* 310.1 (2008). (Cit. on p. 62).

[Zele2008] V. Zeleňák et al. “Amine-modified ordered mesoporous silica: effect of pore size on carbon dioxide capture”. *Chemical Engineering Journal* 144.2 (2008). (Cit. on p. 16).

[Zhao2013] A. Zhao et al. “Carbon Dioxide Adsorption on Amine-Impregnated Mesoporous SBA-15 Sorbents: Experimental and Kinetics Study”. *Industrial & Engineering Chemistry Research* 52.19 (2013). (Cit. on p. 16).